In-silico Modeling of Lipid-Water Complexes and Lipid Bilayers

Dissertation
zur Erlangung des akademischen Grades
des Doktors der Naturwissenschaften (Dr. rer. nat.)
an der Universität Osnabrück
Fachbereich Physik

vorgelegt von

Tayebeh Jadidi

Betreuer: Prof. Dr. Philipp Maaß
Datum der mündlichen Prüfung: 16. Juli 2013

Abstract

Part I: *Ab initio* calculation of biological systems

Throughout this research, the molecular structure and electronic properties of phospholipids, with an emphasis on the most abundant PC including DPPC, under different degrees of hydration at the single bare molecule and also for monolayer structure were investigated by linear scaling *ab initio* calculations. Calculations of the first part of the thesis all were performed by SIESTA; a package for DFT calculations [**?**].

It is observed that upon hydration, the phospholipid undergoes drastic long range conformational rearrangements which lead to a sickle-like ground state shape. The structural unit of the tilted gel-phase PC appears to be a water-bridged PC dimer. The hydration dramatically alters the surface potential, dipole and quadrupole moments of the lipids and probably guides the interactions of the lipids with other molecules and the communication between cells. By performing the same calculations, some of the structural and electronic characteristics of the second most important phospholipid; DPPE, is compared with DPPC.

A complete assignment of the vibrational spectrum of DPPC and DPPC-water complexes shows that water hydrating the lipid head groups enables efficient energy transfer across membrane leaflets on sub-picosecond time scales. The emergence of spatially extended vibrational modes upon hydration, underlies this phenomenon. The collective molecular behavior of biomembranes is found to be important and reveals that hydrated lipid membranes can act as efficient media for the transfer of vibrational energy.

The vibrational modes and lifetimes of pure and hydrated DPPC lipids, at human body temperature, are estimated by performing large-scale *ab-initio* molecular dynamics simulations. The projected atomic vibrations calculated from the spectral energy density are used to compute the vibrational modes and the lifetimes. All the normal modes of the pure and hydrated DPPC and their frequencies are identified. The computed lifetimes incorporate the full anharmonicity of the atomic interactions.

The vibrational modes of the water molecules close to the head group of DPPC are active (posses large projected spectrum amplitudes) in the frequency range between 0.5 - 55 THz, with a peak at 2.80 THz in the energy spectrum. The computed lifetimes for the high frequency modes agree well with the recent data measured at room temperature, where high-order phonon scattering is not negligible. The computed lifetimes of the low frequency modes can be tested using the current experimental capabilities. Moreover, the approach may be applied to other lipids and biomolecules, in order to predict their vibrational dispersion relations, and to study the dynamics of vibrational

energy transfer.

The structure and auto-ionization of water at the water-phospholipid interface are investigated by *ab initio* Molecular Dynamics (AIMD) and *ab initio* Monte Carlo (AIMC) simulations using local density approximation (LDA) and generalized gradient approximation (GGA) for the exchange-correlation energy functional. Depending on the lipid head group, strongly enhanced ionization is observed leading to the dissociation of several water molecules into H^+ and OH^- per lipid. The results can shed light on the phenomena of the high proton conductivity along membranes that has been reported experimentally [?, ?, ?, ?, ?, ?, ?, ?, ?].

Part II: Coarse grained simulation of lipid bilayers

Monte Carlo simulations of the lipid bilayer, which are modeled on the basis of the Lenz and Schmid generic coarse grained model [?], are performed to gain insight into the mechanical properties of planar uni lipid bilayers. By using a rescaling method, the Poisson's ratio, ν, are calculated for different phases. The bending rigidity determined from height fluctuations, based on the Helfrich Hamiltonian, accompanied with the estimated Poisson's ratio allows for calculation of the Young's modulus E for each phase. To extend this study, with the knowledge of both elastic constants E and ν, the local strain energy stored in a lipid membrane might be obtained. Moreover, the direct calculation of these elastic moduli can be processed to validate the obtained results.

The Jarzynski's equality is used to estimate the free energy barrier for lipid flip flop process in the fluid and gel phases of the coarse grained modeled lipid bilayer. The main rate limiting step to complete a flip flop process is related to barrier that has to be crossed in order to reach the center of the bilayer. The free energy cost for performing a lipid flip flop in the gel phase found to be five times greater than in the fluid phase, proving the rarity of such events in the gel phase.

However, the energy profile shows the same trajectory as previous works, smaller energy barriers are estimated in the coarse grained simulated bilayer, which can be explained by the fact that in this model no water pores is observed during the flip flop process. This behavior originated in the over simplification of the model. Moreover, the small number of performed ensemble can be considered as another affecting factor. Using the similar approach, the free energy cost of monomeric exchange is estimated as well. Once the lipid is immersed in the aqueous bulk, the free energy trajectory reaches a plateau value. The energy barrier is obtained for the formation of transient water pores that often precedes lipid translocation events and accounts for the rate limiting step of these pore associated lipid translocation processes.

The next step for this part of the research might be retrieving the Arrhenius pre-exponential factor to predict the flip flop rate by performing a MD simulation for identical phases resulted from different temperatures.

Kurzfassung

Erster Teil: ab initio Berechnungen biomolekularer Systeme

In dieser Forschungsarbeit werden die strukurellen und elektronischen Eigenschaften von Phospholipiden durch linear skalierende *ab initio* Berechnungen mit dem Schwerpunkt auf den häufig vorkommenenden PC inklusive DPPC untersucht. Hierbei werden unterschiedliche Hydrationsgrade der einzelnen, isolierten Moleküle und auch der Monolagen betrachtet. Alle Rechnungen des ersten Teils dieser Doktorarbeit werden mit SIESTA ausgeführt, einem Programmpaket für DFT (Dichtefunktionaltheorie) Berechnungen [**?**].

Es zeigt sich, dass das Phospholipid durch Wasseranlagerung drastische langreichweitige Konformationsumlagerungen erfährt, die zu einer sichelförmigen Grundzustandsform führen. Die Struktureinheit von gel-phasig geneigtem PC scheint ein wasserstoffbrückenbindener PC Dimer zu sein. Die Wasseranlagerung verändert das Oberflächenpotential und die Dipol- und Quadrupolmomente der Lipide drastisch und bestimmt wahrscheinlich die Interaktionen der Lipide mit anderen Molekülen und die Kommunikation mit anderen Zellen. Durch gleiche Berechnungen bezüglich strukureller und elektronischer Merkmale wird das zweitwichtigste Phospholipid DPPE mit DPPC verglichen.

Eine vollständige Zuordnung des Schwingungsspektrums von isoliertem DPPC und von mit Wasser umgebenem DPPC zeigt, dass Wasseranlagerungen an den Kopfgruppen des Lipids einen effizienten Energietransport über eine Membranschicht auf Sub-Picosekunden Zeitskalen ermöglicht. Das Auftreten von räumlich ausgedehnten Schwingungsmoden bei Wasseranlagerungen unterliegt diesem Phänomen. Das kollektive Molekülverhalten von Biomembranen spielt eine wichtige Rolle und zeigt, dass wasserumlagerte Lipidmembranen als effizientes Medium für den Transport von Schwingungsenergie agieren können.

Die Schwingungsmoden und Lebenszeiten von isolierten und wasserumlagerten DPPC Lipiden bei Körpertemperatur des Menschen werden durch umfangreiche *ab initio* Molekulardynamiksimulationen abgeschätzt. Die prognostizierten Atomschwingungen, die sich aus der spektralen Energiedichte bestimmen lassen, werden benutzt, um die Schwingungsmoden und Lebenszeiten zu berechnen. Alle Schwingungsmoden von isoliertem und wasserumlagertem DPPC und seine Frequenzen werden ermittelt. Die berechneten Lebensdauern enthalten den vollen inharmonischen Anteil der Atomwechselwirkungen.

Die Schwingungsmoden von Wassermolekülen nahe der Kopfgruppe von DPPC sind

aktiv (besitzen eine große prognostizierte Amplitude im Spektrum) im Frequenzbereich zwischen 0.5 and 55 THz, mit einem Peak bei 2.80 Thz im Energiespektrum. Die berechneten Lebensdauern für die Hochfrequenzmoden stimmen gut mit den jüngsten Messdaten bei Raumtemperatur überein, wobei die Phononenstreuung hoher Ordnung nicht vernachlässigt werden darf. Die berechneten Lebensdauern bei niedrigen Frequenzmoden können mit gebräuchlichen experimentellen Techniken getestet werden. Außerdem kann die Methode auf andere Lipide und Biomoleküle angewandt werden, um die Schwingungsdispersionsrelation vorherzusagen und die Dynamik des Schwingungsenergietransports zu untersuchen.

Die Struktur und Selbstionisierung von Wasser an der Wasser-Phospholipid-Schnittstelle werden mit ab initio Molekular Dynamik (AIMD) und ab initio Monte Carlo (AIMC) Simulationen unter Benutzung der lokalen Dichteannäherung (LDA) und verallgemeinerter Gradientennäherung (GGA) für das Austausch-Korrelationsenergiefunktional untersucht. Bei bestimmten Lipidkopfgruppen kann eine stark erhöhte Ionisierung beobachtet werden, was zur Dissoziierung von mehreren Wassermolekülen in H^+ und OH^- pro Lipid führt. Die Ergebnisse können Aufschluss über das Phänomen der hohen Protonenleitfähigkeit entlang von Membranen geben, wie unlängst experimentell bestätigt wurde [**?**, **?**, **?**, **?**, **?**, **?**, **?**, **?**, **?**].

Zweiter Teil: coarse grained Simulatuinen von Lipiddoppellagen

Um Einblick in die mechanischen Eigenschaften planarer Doppellagen einfacher Lipide zu erhalten, werden Monte Carlo Simulationen ausgeführt, denen das auf Vergröberung (coarse graining) basierende Modell von Lenz und Schmid zu Grunde liegt [**?**]. Die Poissonrate, ν, wird mittels einer reskalierenden Methode für verschiedene Phasen berechnet. Die Steifheit, ermittelt aus den Höhenfluktuationen der Membran mit Hilfe des Helfrich Hamiltonians, zusammen mit der geschätzten Poissonrate ermöglichen die Berechnung des Young Modulus E für jede Phase. In weiterführenden Untersuchungen könnte durch Kenntnis der beiden elastischen Konstanten E und ν die lokale Spannungsenergie einer Lipidmembran ermittelt werden. Außerdem kann die direkte Berechnung dieser elastischen Module zur Validierung der Ergebnisse herangezogen werden.

Die Jarzynski-Gleichung wird genutzt, um die Barriere in der Freien Energie für einen Umklappprozess des Lipids abzuschätzen, genauer gesagt in den flüssigen und gel-artigen Phasen der mit coarse graining modellierten Lipiddoppellage. Die Rate für solche Umklappprozesse wird hauptsächlich durch die Barriere bestimmt, die überwunden werden muss, um die Mitte der Doppellage zu erreichen. Es zeigt sich, dass der Freie Energie Betrag, der nötig ist, um ein Lipid in der gel-artigen Phase umzuklappen, fünf mal größer ist als der selbe Prozess in der flüssigen Phase, was die Seltenheit derartiger Ereignisse in der gel-artigen Phase andeutet.

Obwohl das Energieprofil den selben Verlauf wie vorherige Arbeiten zeigt, ergeben sich kleinere Energiebarrieren in der mit coarse graining simulierten Doppellage, was dadurch erklärt werden kann, dass hier keine Wasserporen während des Umklapp-

prozesses beobachtet werden. Dieses Verhalten ergibt sich aus der starken Vereinfachung des Modells. Außerdem kann die kleine Anzahl untersuchter Ensembles die Ergebnisse beeinflussen. Sobald das Lipid in eine Wasserumgebung eingebracht wird, erreicht die Freie Energie einen Plateauwert. Die Energiebarriere wird bestimmt durch die Bildung von Wasserporen, die oft der Verschiebung von Lipiden vorausgehen. Gleichzeitig begrenzt die Barriere die Rate, mit der diese Verschiebungen stattfinden.

Eine vielversprechende Möglichkeit, um die in diesem Teil der Arbeit vorgestellten Studien zu erweitern, ist die Bestimmung des Vorfaktors im Arrhenius-Gesetz durch MD Simulationen identischer Phasen bei verschiedenen Temperaturen, um die Rate der Umklappprozesse vorherzusagen.

Contents

Abstract i

Kurzfassung iii

List of Figures xi

List of Tables xv

Abbreviations xvii

1 Introduction 1
- 1.1 Importance of biological membranes . . . 1
- 1.2 Scope of the present work . . . 2
  - 1.2.1 Part I: *Ab initio* calculation of lipid molecules . . . 3
  - 1.2.2 Part II: Coarse grained modeling of lipid bilayers . . . 5

2 Membrane lipids 7
- 2.1 Membrane structure . . . 7
  - 2.1.1 Lipid bilayer phases . . . 8
- 2.2 Composition of biomembranes . . . 12
  - 2.2.1 Lipid structure . . . 12
  - 2.2.2 Asymmetry across membranes . . . 16
  - 2.2.3 Temperature dependence of lipid composition . . . 17
  - 2.2.4 Pressure dependence of lipid composition . . . 17
  - 2.2.5 Other parameters affecting lipid composition . . . 18
- 2.3 DPPC and DPPE . . . 18
- 2.4 Conclusions . . . 19

I *Ab initio* calculation of biomolecular systems 21

3 The SIESTA method for *ab initio* Order-N simulation 23
- 3.1 Introduction . . . 23
- 3.2 The LCAO Basis set . . . 24
  - 3.2.1 Radial flexibility . . . 25

3.2.2 Angular flexibility . . . 26
3.2.3 Transferability . . . 27
3.3 Order-N solution . . . 27
3.4 Calculation of the total energy . . . 28
3.5 Atomic forces and stress calculation . . . 30
3.6 Conclusions . . . 31

4 Molecular and electronic structure of phospholipids 33
4.1 Introduction . . . 33
4.1.1 Experimental methods and their limitations . . . 33
4.1.2 Application of the first principle approach in the force field extending . . . 34
4.2 DPPC molecular structure . . . 35
4.2.1 Technical details of the ground state calculation . . . 35
4.2.2 Pure DPPC structure . . . 36
4.2.3 Hydrated DPPC structure . . . 36
4.2.4 Dimer DPPC structure . . . 38
4.2.5 Hydration energy estimation . . . 40
4.2.6 Contribution of van der Waals interactions . . . 41
4.2.7 GGA and LSDA vs. LDA . . . 41
4.3 Electronic structure of DPPC . . . 41
4.3.1 Charge density profile . . . 42
4.3.2 Electronic dipole and quadrupole moments . . . 42
4.3.3 Surface electric potential . . . 45
4.3.4 Electronic density of states of DPPC and DPPE . . . 47
4.4 Conclusions . . . 49

5 Extended vibrations in membrane lipids 51
5.1 Introduction . . . 51
5.2 Theory of vibrational modes of a cluster . . . 52
5.3 *Ab initio* calculation of vibrational modes . . . 54
5.3.1 Vibrational dynamics of pure DPPC . . . 55
5.3.2 Vibrational dynamics of hydrated DPPC . . . 55
5.3.3 Vibrational dynamics of hydrated bilayer DPPC . . . 57
5.4 Inverse participation ratio . . . 58
5.4.1 Active modes of DPPC . . . 59
5.4.2 Active modes of interfacial water . . . 62
5.4.3 Extended modes of lipid-water complexes . . . 62
5.4.4 Active modes of hydrated bilayer like DPPC . . . 62
5.5 Estimation of phase velocity . . . 64
5.5.1 Method . . . 64
5.5.2 Phase velocities of normal modes in DPPC complexes . . . 65

5.6 Conclusions . . . 68

6 Vibrational lifetimes of pure and hydrated DPPC 69
6.1 Introduction . . . 69
6.2 Spectral energy density formalism . . . 71
6.3 *Ab initio* molecular dynamics simulation (AIMD) . . . 72
6.4 Calculation of spectral energy density of pure and hydrated DPPC . . . 73
6.4.1 Comparison of SED with harmonic approximation phonon DOS 77
6.4.2 Comparison of SED analysis with experiment . . . 77
6.5 Conclusions . . . 77

7 Enhanced auto-ionization of water at phospholipid interfaces 79
7.1 Introduction . . . 79
7.2 AIMD and AIMC simulations . . . 80
7.3 Auto-ionization of neat water . . . 82
7.4 Auto-ionization of interfacial water . . . 82
7.4.1 Electric field induced auto-ionization . . . 83
7.4.2 Lipid-water coupling . . . 87
7.5 Conclusions . . . 90

II Coarse grained simulation of lipid bilayers 91

8 Coarse grained modeling of lipid bilayers 93
8.1 Introduction . . . 93
8.2 Lipid model . . . 94
8.2.1 Intermolecular interactions . . . 94
8.2.2 Intramolecular interactions . . . 95
8.3 Solvent model . . . 97
8.4 Details and methods . . . 98
8.4.1 Initializing the system . . . 98
8.4.2 Thermodynamic parameters . . . 99
8.4.3 Simulation algorithm . . . 99
8.5 Phase behavior . . . 101
8.5.1 Characteristic parameters of lipid bilayers . . . 102
8.6 Conclusions . . . 104

9 Mechanical properties of lipid bilayers 105
9.1 Introduction . . . 105
9.2 Poisson's ratio . . . 105
9.2.1 Simulation details . . . 107
9.3 Fluctuation spectrum . . . 111

9.4 Young's modulus 113
9.5 Conclusions 114

10 Lipid translocation and pore formation **115**
10.1 Introduction 115
10.2 Method 116
10.2.1 Free energy estimation 116
10.3 Lipid translocation 117
10.3.1 Transmembrane lipid translocation (Flip Flop) 118
10.3.2 Inter-membrane lipid translocation (Monomeric Exchange) . . . 122
10.4 Pore formation process 124
10.5 Conclusions 128

A Relaxed structure of pure DPPC **129**

B Calculation of forces **131**
B.1 Two body forces 131
B.2 Three body forces 132

Publications **135**

Acknowledgment **137**

List of Figures

1.1 Singer-Nicholson fluid mosaic model for the cell membrane 1

2.1 Three-dimensional structures of lipids 9
2.2 Experimental phase diagram of DMPC and DPPC bilayer. From [?] . . 9
2.3 Different bilayer phases 10
2.4 Chemical structure of DPPC 12
2.5 Chemical structure of cholesterol 12
2.6 Different head group structures of phospholipids 14
2.7 Saturated and unsaturated fatty acids 15
2.8 The asymmetry in the composition of membranes 17

3.1 Pseudoatomic orbitals for oxygen 26

4.1 Relaxed structure of pure and hydrated DPPC 37
4.2 Tilt angle in the hydrated monolayer DPPC 39
4.3 Relaxed structure of Dimer DPPC 40
4.4 Electron charge density profile of DPPC 43
4.5 Electric dipole p and quadrupole moments Q for pure and hydrated DPPC 45
4.6 Surface potential lines for DPPC 46
4.7 Surface potential of DPPE 46
4.8 Surface potential of hydrated monolayer DPPC 47
4.9 Electronic density of states of pure and hydrated DPPC 48
4.10 Electronic density of states of hydrated DPPC and DPPE 48

5.1 Fully and partially hydrated head part of DPPC 52
5.2 Vibrational density of states for pure and hydrated DPPCs and hydrated bilayer DPPC 56
5.3 Bending mode $\omega = 1419$ cm^{-1} of choline 56
5.4 Displacement vectors for $\omega = 33.02$ cm^{-1} and $\omega = 79.69$ cm^{-1} in hydrated DPPC 57
5.5 Displacement vectors for $\omega = 36.22$ cm^{-1} and $\omega = 74.24$ cm^{-1} in bilayer DPPC 58
5.6 Inverse participation ratio of pure and hydrated DPPC 59
5.7 Distribution of modes with participation of more than100 atoms 60
5.8 Participation ratio of exclusive modes of hydrated DPPC 61

5.9 Opposite effects of interfacial water on the extension of DPPC modes . 63
5.10 Inverse participation ratio of hydrated DPPC bilayer 64
5.11 Sine wave mapped to + and - signs 65
5.12 The phase velocities V_{ph} (ω) for pure and hydrated DPPC 66
5.13 The phase velocity V_{ph} (ω) of a hydrated DPPC bilayer. 67

6.1 (a) Spectral energy density and vibrational lifetimes of pure DPPC. (b) The density of states of the phonon frequencies are obtained by harmonic lattice dynamics computations. 74
6.2 (a) Spectral energy density and vibrational lifetimes of the complex DPPC,$(H_2O)_{50}$. (b) The density of states of the phonon frequencies are obtained by harmonic lattice dynamics computations. 75
6.3 Examples of vibrational modes at frequencies of 2.84, 4.40 and 37.60, corresponding to the frequencies of peaks in the spectral energy density of the DPPC,$(H_2O)_{50}$ complex. As is shown, the lipid's head part is not engaged in the high active modes. The water molecules are not shown here for clear illustration of the head part. 75
6.4 Decomposition of the spectral energy density of the complex of DPPC and water into the separate spectra of (a) DPPC and (b) bulk water. The corresponding vibrational lifetimes are also demonstrated. Plot (c) shows the product of the two spectral energy densities, illustrating the active ranges simultaneously for the bulk water and the lipid. 76

7.1 Ground state structure of DPPC,$(H_2O)_{50}$ 80
7.2 Probability of water ionization at 300 K 83
7.3 Probability density of $r_{O\text{-}O}$ distances of neighboring water molecules . . 84
7.4 Probability distribution of the magnitude of the electric fields experienced by water molecules 85
7.5 Potential iso-surfaces of DPPC,$(H_2O)_{50}$ for V= 500 and -500 mV . . . 86
7.6 Probability distribution of $r_{O\text{-}O}$ of the neighboring water molecules for DPPC,$(H_2O)_{50}$ and DPPE,$(H_2O)_{50}$ 86
7.7 Hydrogen bonds in (HO−H $\cdots$ O=P), (HO−H $\cdots$ O=C), (HO−H $\cdots$ C−O−P) and (HO−H $\cdots$ C−O−C) 87
7.8 Time fluctuations of $r_{O\text{-}O}$ and the potential $U(r)$ for (HO−H $\cdots$ O=P) 88
7.9 Potential U(r) of P−O^-, C−O−P, C=O and C−O−C 89

8.1 Lipid sketch of Düchs and Schmid model 94
8.2 Interactions applied in the model. 96
8.3 Initial configuration of the bilayer system 98
8.4 Phase space digram of the coarse grained model 101

9.1 Poisson's effect snapshots 108

9.2 Poisson's effect snapshots for gel phase, expansion perpendicular to the tilt direction 109
9.3 Poisson's effect snapshots for gel phase, expansion in the tilt direction . 109
9.4 Relaxation of $-\Delta L_\alpha/\eta_\beta L_\alpha$ in (a) fluid and (b) interdigitated. The plateau value reached after about 5000 MC steps, independent of the value of η, yields the Poisson's ratio ν. The fluid and interdigitated phases have the identical values for ν_{xy} and ν_{yx}, representing these phases as in-plane isotropic phases. 110
9.5 Relaxation of $-\Delta L_\alpha/\eta_\beta L_\alpha$ in the gel phase. The plateau value reached after about 5000 MC steps, independent of the value of η, yields the Poisson's ratio ν. In the gel phase, the obtained Poisson's ratio for elongation in the y-direction is $\nu_{xy} = 0.11$ (left axis) and for elongation in the x-direction is $\nu_{yx} = 0.54$ (right axis). 111
9.6 Fluctuation Spectra for three phases 113

10.1 Snapshots of transmembrane lipid translocation 119
10.2 Work distribution and free energy differences for transmembrane lipid translocation in fluid phase 120
10.3 Work distributions and free energy differences for monomeric exchange 123
10.4 Snapshots of the pore formation across a fluid-phase bilayer. 126
10.5 Free energy differences calculated from the distribution of the work in the pore formation processes for the gel and fluid phases ($N_{path} = 50$). 126

List of Tables

2.1 Head group composition of the membranes 13

4.1 Structural parameters of DPPC and hydrated DPPC. The x-axis lies in the plane of the tail, the y-axis is the long axis of the lipid and the z-axis is perpendicular to the tail plane. 38
4.2 Angle between the normal of the glycerol, *sn1* and *sn2* carbonyls with the normal of the tail plane 38
4.3 Electric dipole moments measured in different systems. 44
4.4 Electric quadrupole tensor Q ($ea_0{}^2$) with respect to center of mass, for a single DPPC and DPPC,$(H_2O)_{50}$ complex. 45
4.5 Energy band gap estimates for hydrated DPPC and DPPE. A decrease in the band gap upon the hydration was occurred. 47

6.1 The active vibrational modes of pure DPPC and the complex of DPPC,$(H_2O)_{50}$ at T=310 K and the estimated lifetimes. 74

7.1 Mean and standard deviation of $r_{O\text{-}O}$ and k_{eff} of H-bonds 89

8.1 Interaction potentials of the referenced model and corresponding parameters. r is the distance of the connecting vector of two particles, and as illustrated in Figure 8.1, θ is the angle between every three adjacent beads. 97
8.2 Characteristic parameters of lipid bilayers 103

9.1 Elastic constant 114

10.1 Comparison of the free energy barrier for the lipid translocation process estimated by different experimental and computational methods. 121
10.2 Comparison of the free energy barrier for pore formation estimated by different experimental and computational methods 127

Abbreviations

Ab initio Monte Carlo	AIMC
Ab initio Molecular Dynamics	AIMD
Basis Set Superposition Error	BSSE
Conjugate Gradients	CG
Coarse Grained	CG
Counterpoise method	CP
Density Functional Theory	DFT
Dilauroylphosphocholine	DLPC
Dimyristoylphosphocholine	DMPC
Dipalmitoylphosphatidicacid	DPPA
Dipalmitoylphosphatidylcholine	DPPC
Dipalmitoylphosphatidylethanolamine	DPPE
Dipalmitoylphosphatidylglycerol	DPPG
Dipalmitoylphosphatidylserine	DPPS
Dioleoylphosphocholine	DOPC
Double-ζ Polarized	DZP
Density Of States	DOS
Finitely Extensible Nonlinear Elastic Potential	FENE
Generalized Gradient Approximation	GGA
Kleinman-Bylander	KB
Linear Combination of Atomic Orbitals	LCAO
Local Density Approximation	LDA
Local Spin Density Approximation	LSDA
Monte Carlo simulation	MC
Molecular Dynamics simulation	MD
Phosphatidylcholine	PC
Phosphatidylethanolamine	PE
Potential of Mean Force	PMF
Palmitoyloleoylphosphocholine	POPC
Spectral Energy Density	SED
Spanish Initiative for Electronic Simulations with Thousands of Atoms	SIESTA
Self Consistent Field	SCF
van der Waals interaction	vdW

1 Introduction

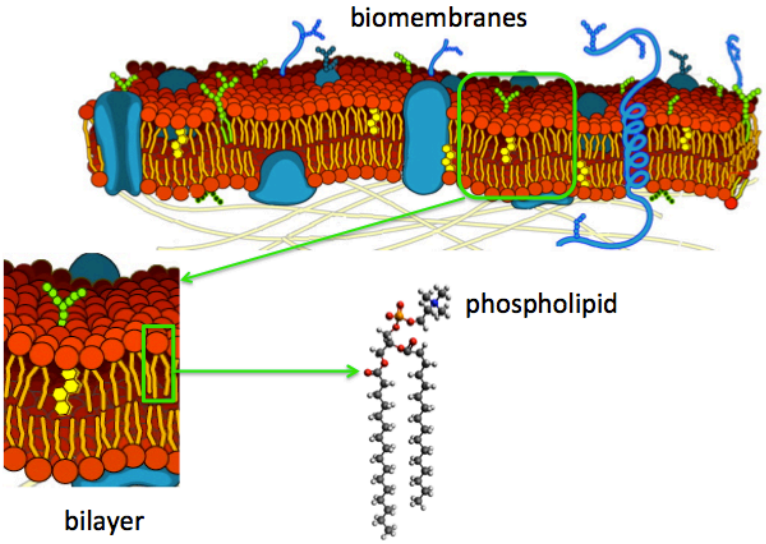

Figure 1.1: Singer-Nicholson fluid mosaic model for the cell membrane. Drawing provided by M. R. Villarreal and figure adopted from 1 in Dec. 1, 2012.

1.1 Importance of biological membranes

Biological membranes (or biomembranes) separate cells from the environment outside. They also provide the interfacial surface of the interior cell organelles. Consisting of complex compositions with a huge diversity in lipid species, proteins and other biomolecules, membranes play a crucial role in cell activities. The ion transportation, communication with other cells and energy conversion are among these functions.

The basic structural skeleton of the membrane is a lipid bilayer. A bilayer is formed of two layers of amphipathic lipids, predominantly phospholipids, with the hydrophobic chains facing each other at the core regions of the bilayer and the hydrophilic head groups exposed to the water environment. They are mostly in fluid phase, however,

[1] http://www.aquasourceproducts.com/phospholipid.html

bear in mind that bilayers constitute a stable structure, which can resist the conformational changes induced by the hydrophobic effect [?], and at the same time they are impermeable for the polar particles.

Divers compositions of lipids and proteins are heterogeneously distributed in the lateral structure of the membrane [?, ?]. On the basis of both chemical evidences (e.g. electron microscopy and chemical composition) and physical studies, the distinct domains of lipids and proteins form a mosaic structure for a biomembrane. However, the non-covalent nature of interactions between particles predicts a fluid phase for membranes in which individual particles are free to migrate in the plane of the membrane. The mosaic model for biomembranes initially proposed by Singer-Nicholson [?], is shown in Figure 1.1.

In experiments, structural deformations or curvatures of the membrane are often observed in the lipid domains consisting of vesicles. Thus, the studies on these related phenomena or activities could be helpful to understand the nature of the cell membrane [?, ?, ?, ?]. Some special cellular activities, such as fusion, fission and membrane deformation, are inferred to be associated with these lipid organizations [?].

Given the importance of membranes to biological functions and the fact that lipids are the key building blocks of membranes, the present work aims to deepen the understanding of the functionality of lipids by exploring chemical and physical properties that have previously been elusive.

1.2 Scope of the present work

The initial chapter will outline the basic principles of lipids and membranes, in order to obtain more general knowledge about these biomolecular systems.

In the following, the first part of this thesis will specifically investigate the chemical properties of lipids. Up to now, it has not been possible to obtain precise measurements because of the insufficient computational power for the analysis of a huge number of atoms, as is the case in biological systems. The present work applies an *ab initio* method, which is traditionally used for the study of the interaction of electrons, to the analysis of atoms in relatively large molecules like lipids. Considering the fact that the dipalmitoylphosphatidylcholine (DPPC) is the most abundant lipid found in biomembranes, the present work specifically focuses on this molecule; both as a single molecule, and as part of a molecular complex.

The second part of this work, is devoted to study lipid bilayers as a structure consist of a number of lipids. However, the complexity of this biological entities is simplified by considering a bilayer composed of only one type of lipid, the study of such a large system is far beyond the ability of the first principle approaches. Moreover, investigation of dynamical phenomena such as lipid translocation, which happens in the nanosecond time scales, makes it impossible to use more accurate approaches such as DFT based simulations. As a result, by taking the benefit of a less accurate but more efficient coarse

grained simulation method, some of the mechanical properties of uni-lipid bilayers were investigated. In addition, by performing the coarse grained simulation, the phenomena of lipid translocation across the bilayer and also in between them were simulated as well.

The following sections of this chapter provide a more detailed introduction to the concepts studied in Parts 1 and 2 of this thesis.

1.2.1 Part I: *Ab initio* calculation of lipid molecules

In the first chapter, the appropriateness of using the SIESTA package for the analysis of lipids is discussed. SIESTA has been developed as a fully self-consistent density functional method in order to perform first-principle calculations on very large and complex systems by using Order-N operations [**?**]. It uses numerical linear combinations of atomic orbitals as the basis set with a high degree of flexibility and efficiency. The core electrons are substituted by norm-conserving pseudopotentials [**?**]. In order to calculate the long range self consistent potential, i.e. Hartree and exchange correlation potentials and matrix elements, the basis functions and electron densities are projected on a real space grid, which allows the computational cost to be scaled linearly with the size of the system [**?**]. SIESTA benefits from a modified energy functional, whose minimization generates orthogonal wavefunctions. The advantage of these functionals is that without performing time consuming orthogonalization [**?**], the resulting energy and density are the same as if they had been obtained by the Kohn-Sham functionals. The sparse Hamiltonian and overlap matrices are calculated with an Order-N effort [**?**]. Total energy of the system, atomic forces and stresses are calculated with Order-N methods, using strictly localized Wannier-like electron wavefunctions, which makes it possible to find the minimum energy structure of the system as well as performing molecular dynamic simulations [**?**]. In the first chapter of this part, these procedures, which make SIESTA an impressively efficient and accurate method to perform *ab initio* calculations for systems with significantly large number of atoms, will briefly be introduced.

Having established the appropriateness of the linear scaling *ab initio* method, which was implemented in the reference package SIESTA, for the analysis of lipids, the second chapter of the first part reports the results of using this package in order to explore the chemical structure and electronic behavior of two important lipids. More specifically, throughout this part of the research, the structure and electronic properties of phospholipids, under different degrees of hydration at the single-molecule and monolayer type level were investigated. The present study is concerned with lipids structure, with an emphasis on two most abundant phospholipids namely dipalmitoylphosphatidylcholine (DPPC) and dipalmitoylphosphatidylethanolamine (DPPE). As the first step, the ground state structures of these biomolecules were sought and consequently the conformational rearrangement upon hydration were investigated. Searching for a structural unit of phospholipids can be interesting for providing appropriate information about

bilayers relaxed structures. To this end, a DPPC dimer is suggested as an appropriate unit structure for modeling monolayers of membranes in gel phase, and the suitability of such a unit structure was examined through the energy approximations. Some of the electronic properties of these biocomplexes, including surface potential, dipole and quadrupole moments, were investigated both in presence and absence of aqueous environment.

The obtention of the minimum energy structure of these two lipids allowed for a phononic analysis, this is the subject matter of the next chapter of Part 1. In this chapter a complete assignment of the vibrational spectrum of DPPC will be reported. The importance of these analyses is behind various applications have been found for phonon DOS in exploring the physical quantities of materials. The phonon frequencies can be used to calculate the thermodynamic properties of the system, such as free energy, entropy and heat capacity. Moreover, the eigenvectors are an effective method for understanding the polarization of the mode. In the next step, a discussion about the influencing role of the aqueous environment surrounding lipid head groups in energy transfer along the cell membranes, is presented. Many experimental work on this topic have already been reported [**?**].

However, the static investigation provides vast knowledge about biomolecules, as these molecules are dynamic entities, this window is insufficient for understanding many biological activities [**?**, **?**]. Hence, attention has turned to dynamical properties, and in particular the time scales over which a biomolecule performs a specific activity, or takes part in a phenomenon. It is well recognized that any information about the dynamics and characteristic time scales of biomolecules actions sheds light on many processes in which they participate. To this end, in Chapter 6, the spectral energy density approach is applied to study the relaxation time of vibrational phonons in DPPC molecule and the hydrated DPPC complex as an example of biological systems. In this chapter, the vibrational lifetimes and the spectrum of the active frequencies, which were calculated by applying the SED method for trajectories of dynamical evolution of the mentioned systems, acquired from *ab initio* molecular dynamics (AIMD) simulation, will be reported.

In the final chapter of Part 1, a further analysis was conducted in order to examine the dynamical phenomenon of the high proton conductivity along membranes. This phenomenon has already been investigated experimentally [**?**, **?**], however, many details about the high lateral proton conductivity remain elusive. For the study of the structural behavior and in order to understand the auto-ionization processes of water molecules at the water-phospholipid interface, *ab initio* molecular dynamics and *ab initio* Monte Carlo simulations were used to perform reliable calculations based on a sufficiently large number of steps to reflect the movement of molecules and their interactions. In addition, in order to rectify possible ambiguity in the results due to the application of different levels of density functional approximations, both local density approximation (LDA) and generalized gradient approximation (GGA) were used for the estimation of the exchange correlation energy functional term.

1.2.2 Part II: Coarse grained modeling of lipid bilayers

In Chapter 8, the generic coarse grained model were applied to simulate the bilayer is presented. This bead spring coarse grained model was initially introduced by Düchs and Schmid [**?**], in order to study the phase behavior of lipid monolayers. For the aim of the present study, the improved version of this model was applied, which was developed by Lenz and Schmid [**?**].

Elastic properties have a determining role in a number of membrane processes such as membrane fusion [**?**]. By considering a membrane as a two-dimensional matrix, its mechanical properties in the absence of anisotropies can be characterized by two elastic constants according to continuum elasticity theory. In common practice of material characterization, these are typically Young's modulus and Poisson's ratio. In Chapter 9, a method for determining the Poisson's ratio, ν, is introduced and the results of the application of this method for the coarse grained lipid membrane model for the fluid, gel and interdigitated phases are presented. This method is based on rescaling bead positions and implementing periodic boundary conditions to laterally extending the bilayer, instead of direct forcing. Having the bending rigidity, k_c, as obtained from the power spectrum of bilayer height fluctuations, the Young's modulus, E, will be calculated.

Transmembrane lipid translocation (flip flop) is an important, not yet well understood due to its nonequilibrium dynamical nature, with involvement in processes such as membrane asymmetry and viral infection. In the very last chapter of this work, by using the Jarzynski's equality, the free energy barrier was calculated for lipid flip flop process in the fluid and gel phases of the coarse grained model of lipid membranes. Using similar approach, the free energy cost of inter-membrane lipid translocation (monomeric exchange) was studied as well. Finally, the energy barrier was obtained for the formation of transient water pores that often precedes lipid translocation events and accounts for the rate limiting step of these pore associated lipid translocation processes.

2 Membrane lipids

Before engaging in the specific subject matter of parts 1 and 2 of this thesis, it is useful to review some of the basic concepts of the physical structure of membranes and their basic structural elements; bilayers. This background information is important for a better understanding of some of the concepts on which this thesis is based. This chapter therefore presents the overall properties and mechanisms of membranes and lipids. The chemical nature of lipids as the basic element of the bilayers will also be discussed. A full treatment of these subjects would be far beyond the scope of this thesis. Textbooks on biomembranes (e.g. [**?**]) can be used as references for more detailed information. In addition, some general review articles have provided a rich wealth of knowledge about the characteristics of lipid bilayers [**?**, **?**, **?**, **?**].

Cell membranes represent a complex composition of huge number of different lipids and proteins. This chapter will more specifically present the physical structure of membranes as a function of the lipid shape and their amphiphilic response to the watery environment. It will be shown that the bilayer phase is the most prevalent structure of membranes. For the aim of this work the chemical nature of lipids as the basic element of the bilayers will be introduced afterwards. It will also be demonstrated that the lipid composition changes in a coherent manner as a response to growth conditions that can be expressed in terms of intensive thermodynamic variables such as temperature, pressure, or the polarity of the aqueous medium.

2.1 Membrane structure

Lipid molecules are amphiphilic biological structures. Therefore, in an aqueous environment they aggregate in such a way that they shield the hydrocarbon chains from water and expose the polar head groups to the water molecules. Moreover, the lipid dispersion tends to reach the maximum distributional entropy. The lipid aggregates with less concentration in water which results in a higher entropy per molecule. However, the most important determining factor for the aggregation of lipids is that, independently of lipid concentration, the more the contact of hydrophobic chains with water the less the entropy per chain. Due to different lipid concentrations in aqueous environments, several phases of lipid water systems are formed. A key parameter that describes the preferred shape of lipid assembly is the packing parameter of the lipids, defined as [**?**]

$$P = \frac{V_{\mathrm{t}}}{l_{\mathrm{t}} A_{\mathrm{h}}}, \tag{2.1}$$

where V_t and l_t are the volume and the length of the hydrophobic tail, such that V_t/l_t is the average cross sectional area of the tail groups parallel to the surface, and A_h is the average area per head group. Among the most prominent phases, which are formed by lipids are:

- *Micelles, Cylindrical micelles.* When the surface area of the lipid head group is much larger than the average cross sectional area of the tail groups, lipids assemble in a spherical $P \leq 1/3$, (Figure 2.1.c) or cylindrical micelles $1/3 \leq P \leq 1/2$ (Figure 2.1.e). Phospholipids with a single aliphatic tail group can create formations within this range of packing factor. In a micelle, head groups lie on the sphere surface facing toward the water and tails fill the inner part of the sphere shielded from the water.

- *Lamellar phases.* When the head surface area is almost as large as the tail cross section area $1/2 \leq P \leq 1$, lipids can form a planar bilayer. Lipids with two aliphatic tail groups are able to assemble into this structure (Figure 2.1.a). A vesicle is a bilayer forming a closed structure (Figure 2.1.b).

- *Inverse hexagonal phase.* The inverse hexagonal phase forms at high temperature. The associated increase in entropy leads to an increase in the chain volume. Therefore, the cross sectional area of the tail groups is larger than the average area per head group, so $P > 1$ and the lipids form cylinders with the chains directed to the outside (Figure 2.1.d). To minimize the interfacial area of hydrocarbon chains and water, the cylinders assemble into two-dimensional hexagonal crystals [**?**]. Cholesterol and phospholipids with a small head group and two branched or unsaturated tails form the inverse hexagonal structure.

2.1.1 Lipid bilayer phases

In biological membranes lipids dominantly tend to form planar bilayers. Due to the variation of thermodynamic and chemical properties of the surrounding environment, lipid tail and head groups are differently ordered and various phases can exist in the bilayer phase digram (Figure 2.2). In fact cell membranes consist of a complex mixture of several lipid types with various characteristics. Despite the significant progress in experimental and computational methods, this complexity has prevented researchers from precisely understanding the overall phase behavior of such mixtures. Instead, in many cases, only the phase behavior of single lipid bilayers has been studied. This is also the case in the present work, the analysis was carried out in a bilayer composed of a single type of lipid. This section describes the general phase characteristics of the uni-type bilayer. The bilayer phases can exist in different states. The different states as temperature is increased can be summarized as follows:

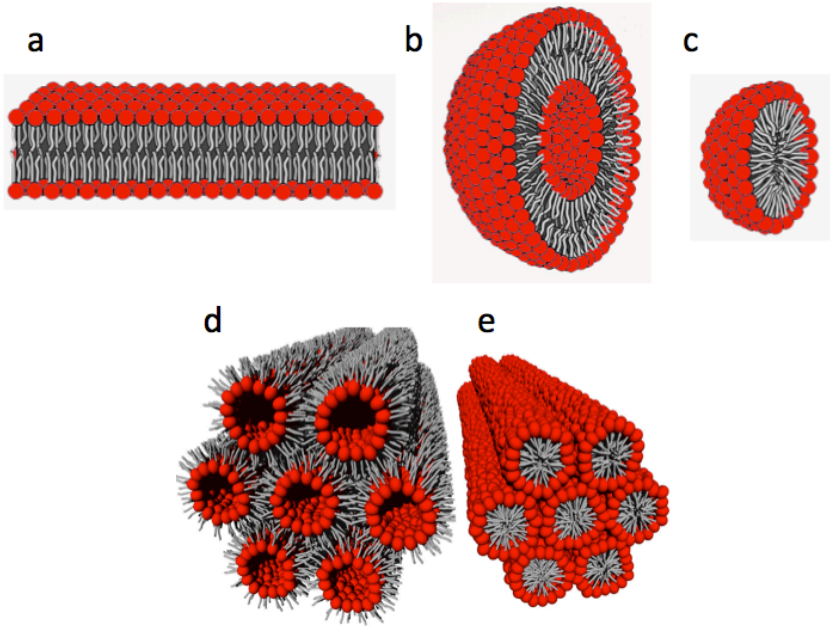

Figure 2.1: Illustration of three-dimensional structures of lipids. (a) bilayer, (b) vesicle, (c) micelle, (d) inverted hexagonal and (e) cylindrical micelle phase. The hydrophilic head groups and the hydrocarbon chains are shown in red and grey, respectively. Figures (a), (b) and (c) are adopted from 1 and figures (d) and (e) from [**?**], in Dec. 1, 2012.

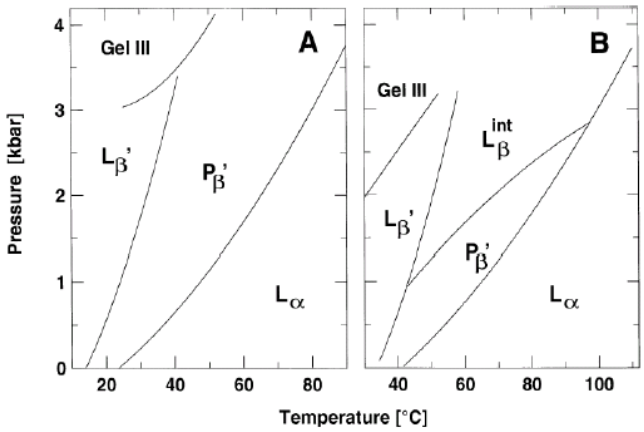

Figure 2.2: Experimental pressure-temperature phase diagram of (A) DMPC bilayer and (B) DPPC bilayer. The plot taken from [**?**].

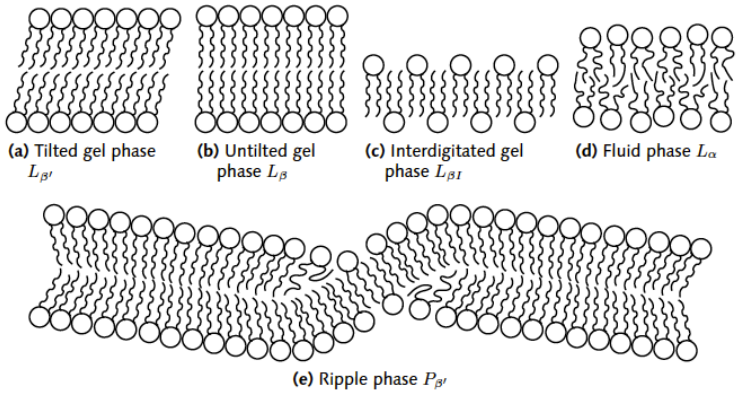

Figure 2.3: Illustration of different bilayer phases. Figure taken from [**?**].

- *Subgel* (L_c). At low temperatures, the lipid chains are ordered into all-trans chains, leading to long, stretched and densely packed chains which are located parallel to each other, resulting in a well-ordered structure similar to what is illustrated in Figure 2.3.b. In this crystalline lipid phase, the head groups are closely packed in a lattice with a pronounced orthorhombic structure.

- *Gel phase* (L_β) and *tilted gel phase* ($L_{\beta'}$). By increasing the temperature, the lipid bilayer undergoes a phase transition from subgel phase L_c, to gel phase L_β or tilted gel phase $L_{\beta'}$. In these phases lipids are mostly arranged in an all-trans configuration in the bilayer, but not all of them, as is the case in the L_c phase. The chemical nature of the head group and its interactions are crucial factors driving the transition. In the gel phase polar head groups distance from each other and are arranged into two-dimensional triangular lattices in the membrane plane. The size of the head group, and more importantly, its relation to the cross sectional area of the tails, i.e. the packing factor, determine the preferred shape adopted by lipids. In the $L_{\beta'}$ phase, the lipid chains are tilted with respect to the membrane normal. Phosphatidylcholines, with a bigger head group and a higher polarity, are tilted at about 30°, while phosphatidyletanolamines which have a smaller head group with weaker polarity do not display a distinguishable tilt angle. By increasing the tail cross section parallel to the bilayer plane, tilted chains minimize the mismatch between head and tail size. However, the tail chains are still well ordered and densely packed as was the case for the subgel phase, L_c. This phase is also called the solid-ordered phase (Figure 2.3.a and b).

- *Ripple phase* (P_β). Upon further temperature increase but prior to chain melting, the lipid systems in the tilted gel phase, $L_{\beta'}$, most likely undergo the pretransition to the ripple phase, P_β. In this phase the lipid bilayer consists of a partially melted lipid phase with a lower average degree of chain ordering than in the $L_{\beta'}$ phase.

The ripple phase exhibits periodic one-dimensional structures on the membrane surface [?]. The periodic arrangements of gel and fluid lipid domains form the ripples (Figure 2.3.e). Although some molecular dynamics simulations tried to shed light on the molecular structure of these phases, the nature of the transition is still elusive [?, ?]. The structural properties such as the wavelength of the ripple structure have been investigated by using a coarse grained model in [?]. More precise details about this phase including the chemical composition of lipids producing this phase can also be found in [?].

- *Liquid-crystalline phase* (L_α). By increasing the temperature yet again, the lipid bilayer undergoes what is referred to as the main transition. Above the transition temperature, T_m, the liquid-crystalline or fluid phase, L_α, is produced (Figure 2.3.d). In this liquid-disordered phase, both the chain order and the triangular lattice arrangement are eliminated. Therefore, the main transition is also called the chain order-disorder transition. The fluid phase is the most common phase found in the biological membrane [?]. This fluid-like phase forms a stable base for lipid membranes with molecules being free to move laterally in the membrane plane.

The other determining thermodynamic parameter, on which the bilayer phase behavior depends, is pressure. A high pressure in the system can cause a slight shift in the subtransition temperature. The creation of two extra phases for the lipid bilayer system was also predicted in higher pressure.

- *Gel III*. By increasing the pressure at low temperature, an additional subgel phase is created. This new subgel phase is called Gel III phase. Bilayers in this phase are ordered in a monoclinic chain packing.

- *Interdigitated phase* ($L_{\beta I}$). At intermediate temperatures and low pressures, interdigitated gel phase $L_{\beta I}$ is observed (Figure 2.3.c). Formation of the interdigitated phase by hydrostatic pressure is mainly driven by the packing of acyl chains. This is otherwise difficult to achieve because of the large cross sectional areas of the polar head groups. In this phase, the mismatched region of one leaflet is matched with the shorter chain of the other leaflet so that the bilayer thickness is low and is approximately the length of the longer chain [?, ?]. As a result the distance between head groups increases and no tilt is observed in this phase. Inserting small amphiphilic (co-surfactant) molecules such as ethanol, ethylene glycol, and generally alcohol, into lipid bilayer mixture, can also induce the interdigitated phase [?]. In the presence of the alcohol, the interdigitated phase is formed because the alcohol molecules rearrange themselves in between the head groups, which cause an increase in the average head-head distance.

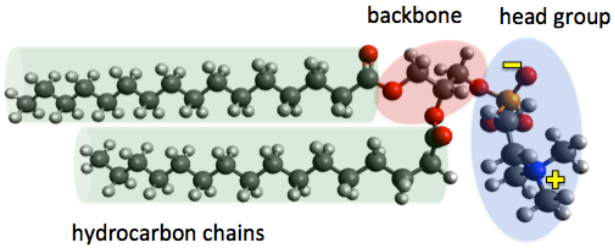

Figure 2.4: Chemical structure of a lipid (DPPC), showing head group, glycerol backbone and hydrocarbon chains.

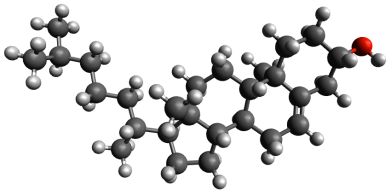

Figure 2.5: Chemical structure of cholesterol.

2.2 Composition of biomembranes

Lipid bilayers are the basic structural element of biomembranes, so the lipid type has a profound influence on the phase behavior of the membranes. The following sections of this chapter deal with the chemical structure of lipids; namely the head group, the hydrocarbon chain and the linkage. The lipid composition varies greatly depending on the different cell types as well as different organelles within cells. Some principles of lipid distribution along the membranes will briefly be introduced as well. Next, it will be discussed that the membrane lipids show asymmetry in their distribution on the two monolayers. Furthermore, the key role of thermodynamic variables such as temperature, pressure and the polarity of the aqueous medium in changing the lipid composition will be demonstrated.

2.2.1 Lipid structure

Lipids are amphiphilic molecules consisting of a hydrophilic head group, one or multiple hydrophobic hydrocarbon chains, and in many cases an extra linkage which connects the head part to the tail part, as is shown in Figure 2.4. The amphiphilicity is the driving force of spontaneous self-assembly of the lipid molecules into membrane structures. Lipids composing biological cells exhibit a rich wealth in chemical characteristics. Among the main groups of lipids which occur in the membrane are fatty acids, consist-

Membrane	PC	PE	PS	PI	SM	CL	Glycolipid	Cholesterol	Others
Erythrocyte (human)	20	18	7	3	18	-	3	20	11
Plasma (rat liver)	18	12	7	3	12	-	8	19	21
ER	48	19	4	8	5	-	tr	6	10
Golgi	25	9	3	5	7	-	0	8	43
Lysosome	23	13	-	6	23	≈5	-	14	16
Nuclear membrane	44	17	4	6	3	1	tr	10	15
Mitochondria	38	29	0	3	0	14	tr	3	13
Neurons	48	21	5	7	4	-	3	11	1
Myelin	11	17	9	1	8	-	20	28	6

Table 2.1: Head group composition of the membranes of rat liver cells, erythrocytes and nerve cells in weight percent. The table is taken from [**?**]. Abbreviations are as follows: PC = phosphatidylcholines, PE = phosphatidylethanolamines, PS = phosphatidylserines, PI = phosphatidylinositols, SM = sphingomyelin.

ing of a carboxylic acid of the form R-CO-OH, in which R can be a hydrocarbon chain such as phospholipids (Figure 2.6) and steroids such as cholesterol (Figure 2.5) as well as lanosterol. Other lipids such as sphingomyelin and ceramide are also found in membrane although they are proportionally less abundant than phospholipids. Other lipid molecules which exist in membranes are glycolipids consisting of a sugar component and two fatty acid chains. Glycolipids play a crucial role in cell signaling and also in the immune system [**?**].

Head group composition

The hydrophilic head composition of lipid membranes is very diverse. The chemical nature of head groups vary in their net charge, chemical compounds, polarity and also size. Figure 2.6 illustrates different kinds of head groups which are found in phospholipids. The most abundant lipids in nature are phospholipids with a glycerol backbone. Phospholipids usually consist of two hydrocarbon chains connected to the first and second position of the glycerol backbone and a phosphate-containing head group bound to the third position. The nomenclature for a lipid with a phosphatidylcholine head group and two palmitoyl chains is 1,2 palmitoyl-glycero-sn-3-phosphocholine, or briefly, dipalmitoylphosphatidylcholine (Abbreviation: DPPC).

The head group can differ in terms of polarity and carrying net charge. For example, phosphatidylcholines (PCs) and phosphatidylethanolamine (PEs) are zwitterionic, i.e. their net charge in the neutral pH is zero. However, the other four lipid types shown in Figure 2.6 are negatively charged. Naturally, no positively charged lipids exists. Among the phospholipids shown in Figure 2.6, only cardiolipin has a dimer of two phospholipids and two negative charges in the head part. This lipid is found in high concentrations in mitochondrial membranes, so these membranes are highly charged.

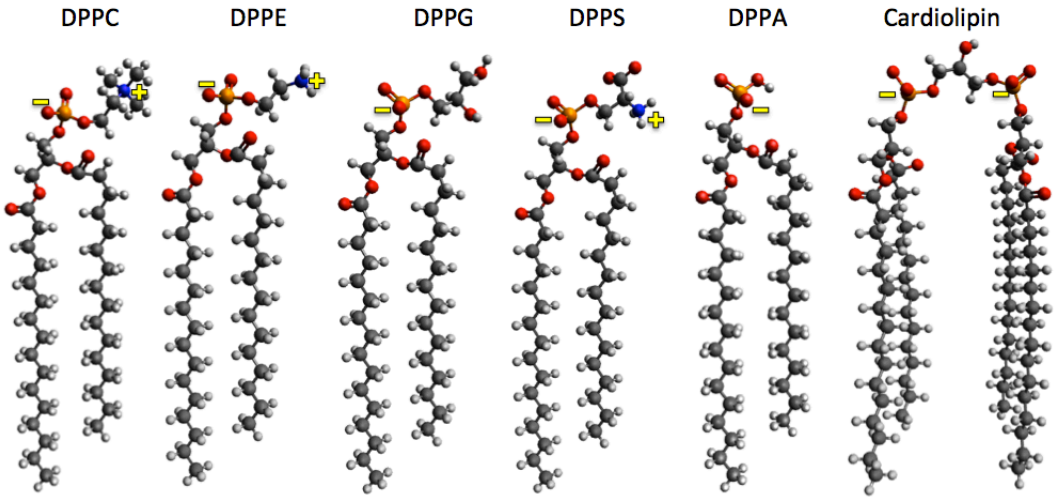

Figure 2.6: Head group structures of some phospholipids with palmitic fatty acid chains: phosphatidylcholine (DPPC), phosphatidylethanolamine (DPPE), phosphatidylglycerol (DPPG), phosphatidylserine (DPPS), phosphatidic acid (DPPA), and cardiolipin (with four chains and two phosphate groups).

The diversity of the size of the head groups has a profound effect on the bilayer phase and the preferred shape adopted by lipids. For example, the head group of dialkyl phosphatidylcholines is quite large which allows these lipids to form the interdigitated gel phase $L_{\beta I}$. This is very unlikely to happen for lipids with small head groups. In addition, the tilt angle observed in some bilayers is the direct result of the geometrical characteristics of the lipid head groups. Small head groups convey different properties, for example, an -OH group in the diacylglycerols, allow these lipids to assemble into micelles. The same situation occurs for sterols such as cholesterol (Figure 2.5), which has a key functional role within the membrane. Up to 20 wt.% of erythrocyte membranes and other plasma membranes of animal cells are composed of cholesterol and its weight can locally increase up to 50 wt.% in rafts. Ergosterol and lanosterol are also other important sterols which mostly occur in fungal plasma membranes [**?**] and procaryotes, respectively. The contribution of different lipid head groups in various cell membranes are different. This difference affects the physico-chemical functionality of membranes. As an illustration, Table 2.1 displays the lipid head group distribution of several organelles [**?**].

Hydrocarbon chain composition

As well as an impressive diversity in the head groups, membrane lipids also display a large diversity in their hydrophobic hydrocarbon chain composition. The acyl chains vary in chain length, number of branches and the degree of saturation. They usually

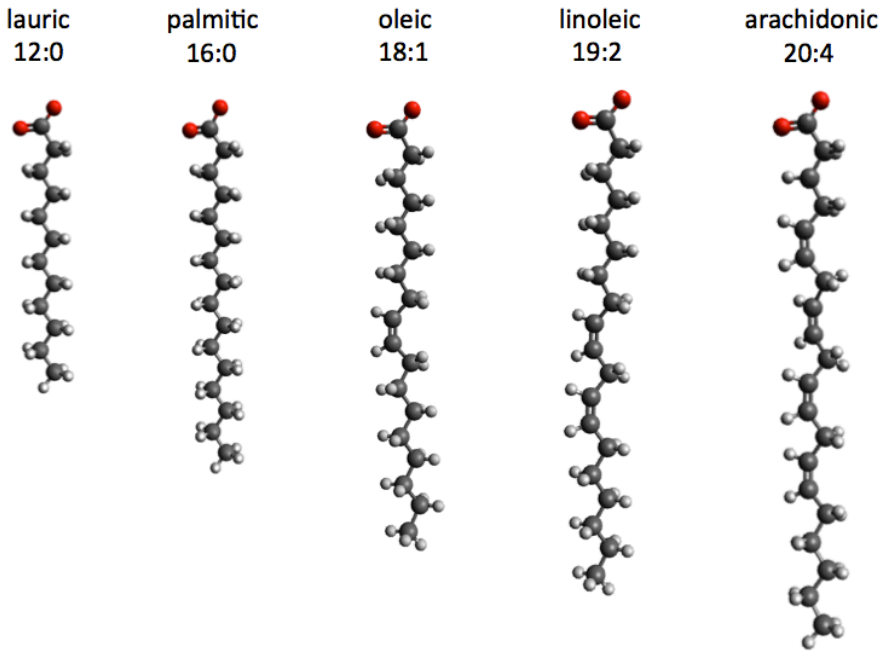

Figure 2.7: Some of saturated and unsaturated fatty acids that form the hydrocarbon chains of lipids.

consists of 12 to 24 carbon atoms, with predominantly an even number of atoms. The chain composition in biomembranes is different for lipids with different head groups [**?**]. For example the chain length in phosphatidylcholines is relatively short, ranging from 16 to 18 carbons, while sphingomyelins tend to have long chains with 24 carbons. The long chains in sphingomyelins are responsible for the formation of microdomains in biological cells [**?**]. One of the main properties in the lipid bilayers, which is affected by the length of the hydrophobic tails is the transition temperature, such that the longer the hydrophobic tails, the higher the phase transition temperature. The long length can also act as a driving factor in the formation of the interdigitated phase $L_{\beta I}$ in the lipid bilayers by canceling the effect of the interaction of the head groups at high pressures [**?**].

Lipids without any double bonds are called saturated lipids, and lipids with one or several double bonds in their fatty acid chains are called unsaturated lipids. Double bonds cause a kink in the hydrocarbon chain and the tail can not rotate around the bond anymore. The asymmetry created by the double bonds can affect the packing of the chains in the ordered gel and subgel phases and results in a significant decrease in the main transition temperature. A chain denoted with 16:1 stands for a chain with 16 carbons with one double bond, while 16:0 is used for a chain without a double bond. The degree of saturation can also influence the transition temperature in the lipid bilayers and it has found that the more the number of double bonds, the less the

melting temperature. Tails branching can also decrease the transition temperature by increasing the average cross section of the tail part.

In biological membranes, lipids are formed of one or several fatty acid chains. Lipids with two hydrophobic tails are the most prevalent. However, there are some special types of lipids such as cardiolipin, which consist of four hydrocarbon fatty acids (Figure 2.6). The chain composition is also different in different cells and in different organelles of the same cell, as was the case for lipid head groups. For instance the weight percentage of 15:0 carbon chains is much higher in the plasma membrane and much lower in mitochondrial membranes. Similarly, the plasma membrane contains a large portion of 16:0 carbons, while this contribution is much lower in mitochondrial membranes. The most abundant acyl chains are illustrated in Figure 2.7.

Linkage

Last but not least, the linkage between tails and the glycerol backbone significantly influence the bilayer structure and consequently the phase behavior of membranes. For instance in PCs, a linkage between fatty acid and backbone with alkyl or acyl can alter the phase between the gel phase L_β, and the interdigitated gel phase $L_{\beta I}$. The reason is that PCs with acyl linkages can form hydrogen bonds between the acyl oxygens, resulting in the stabilization of the gel phase L_β. This is not the case for PCs with an alkyl linkage [**?**]. In some lipids such as sphingomyelin and ceramide there is no glycerol backbone. These sorts of lipids usually have long saturated chains, responsible for the formation of microdomains in biological cells [**?**].

2.2.2 Asymmetry across membranes

The lipid composition can vary within the two leaflets of biomembranes. This asymmetry is due to different ambient physical properties, such as the electrostatic field gradients or differences in the chemical potential around the membrane. For instance, in nerve cells with a voltage difference of -70 mV, lipid distribution with respect to their charge is completely different for inner and outer leaflets. In addition, the energy consuming active phenomena inside the membrane also affect the lipid distribution. In Figure 2.8, the lipid composition for both monolayers of erythrocyte membranes is shown [**?**]. For erythrocyte membranes, the negatively charged phosphatidylserines are mostly located on the inside, while zwitterionic phosphatidylcholines and sphingomyelins are rather found on the outside. Furthermore, lipids (and also proteins) are not homogeneously distributed even within one monolayer leaflet. This heterogeneity causes phase segregation and domain formation within the monolayers. Formation of these domains is a driving force for some biological processes in cells such as fusion, fission and budding.

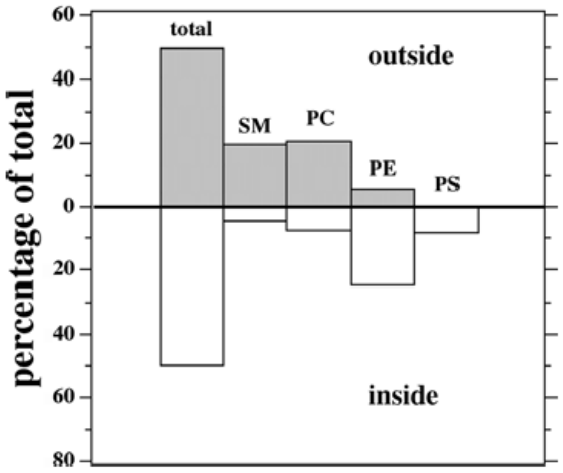

Figure 2.8: The asymmetry in the composition of membranes in the outer and the inner leaflet of the membrane. In human red blood cell membranes, phosphatidylcholines and sphingomyelin are found mostly on the exoplasmic leaflet side while phosphatidylethanolamine and phosphatidylserine are rather found on the cytoplasmic leaflet. This figure is taken from [**?**] using the data adapted from [**?**].

2.2.3 Temperature dependence of lipid composition

Lipid membranes display phase transitions under varying temperatures. Among these transitions, the melting transition occurs at critical temperature T_m, at which lipids in gel phase undergo a transition to the fluid phase. Critical temperature T_m, depends on the chain properties such as the chain length and the number of double bonds in the chain. The melting temperature increases by elongation of the chain length, while the more double bonds in a chain, the lower the melting temperature. For instance DOPC with one double bond in its hydrocarbon chain displays a melting temperature of around 20 °C, while the melting temperature for DSPC without any double bond is about 53 °C. Many biological phenomena such as nerve pulse propagation and membrane permeability directly depend on the melting transition. The changes in the ambient thermodynamic properties, i.e. temperature and pressure, significantly influence the lipid composition of biomembranes. The dependence of the lipid composition as well as the melting point on temperature increase has been widely investigated.

2.2.4 Pressure dependence of lipid composition

Pressure is another thermodynamic variable which influences the phase transitions of biomembranes. As was the case for temperature, when pressure changes, the physical properties of membranes change to adapt the organisms to the pressure changes.

Increasing the pressure of the growth environment results in increasing the melting temperatures. However this influence is not profound, such that 40 bar of pressure decreases the melting transitions by about 1 K [**?**, **?**].This result can be explained by the fact that the increase in pressure changes the concentration of unsaturated lipids with respect to saturated lipids. As mentioned above, unsaturated chains lower the melting point while saturated chains increase the melting point and are predominantly found at low pressures.

2.2.5 Other parameters affecting lipid composition

In addition to pressure and temperature, other thermodynamic variables, including pH, chemical and electrostatic potentials of all components of the biological systems are affecting the phase transition of the system. Alcohol like ethanol lowers melting temperatures, so it is predicted that the presence of alcohols affect the lipid properties in the same way as high growth temperature. Similarly, the presence of other solvents and chemicals, which can rearrange the lipid composition have been investigated [**?**]. The ambient pH is another influencing parameter, such that the decrease in ambient pH has the same effect as that of pressure increase. The reason is that in lower pH, the portion of negatively charged lipids is distinguishably higher and they can be protonated, which results in increasing their melting temperature.

2.3 Dipalmitoylphosphatidylcholine (DPPC) and dipalmitoylphosphatidyethanolamine (DPPE)

The most abundant lipids in the membranes of living organisms are the phospholipids (Table 2.1), in particular phosphatidylcholines (lecithins), phosphatidylethanolamines (PEs), and sphingolipids. Among these classes of lipids dipalmitoylphosphatidylcholine (DPPC) is a benchmark molecule which has been widely investigated in both experimental and computational studies. In Figure 2.6 the chemical structure of DPPC lipid is depicted. One of the reasons that makes this lipid distinguishable is that, up to 40 wt.% of lung surfactant is composed of DPPC. Lung surfactant needs to maintain low surface tension under expansion and contraction and DPPC is the chemical substance that tremendously reduces surface tension [**?**]. In Figure 2.6, the second most abundant phospholipid in biomembranes, dipalmitoylphosphatidylethanolamine(DPPE), is also shown. DPPE consists of a phosphate group in the head part as well as DPPC. The only structural properties of DPPE, which are different from DPPC, is that the ethanolamine group is connected to the phosphate component instead of the choline group in the head part of the DPPC. The two fully saturated hydrocarbon chains of this fatty acid consist of 16 carbons in each chain, which are esterified to the glycerol backbone form the tail part of the DPPE, as it is exactly the case in DPPC.

In the present work the *ab initio* method has been used to investigate a wide range of chemical and physical structures of these two important lipids. The rich wealth of data on these biomolecules allows a comparison of results and the evaluation of their accuracy.

2.4 Conclusions

In this chapter, a few preliminary concepts of chemistry and physics of lipids have been introduced. Depending on the lipids geometrical extension they form many different phases in an aqueous environment, such as micelles, bilayers and hexagonal phase. Biomembranes are mostly found in bilayer phases. Furthermore, lipid bilayers can occur in various phases depending on different thermodynamic parameters. The most abundant lipids in biomembranes are phospholipids which are naturally amphiphilic molecules with a hydrophilic head and a hydrophobic apolar tail moiety. The head groups vary in their net charge, size and polarity. The tail groups vary in the length and the degree of saturation. Every cell and organelle within the cell has a different composition of lipids with different proportions which are distributed heterogeneously along either leaflets of the membrane. The growth temperature and ambient pressure strongly influence the lipid composition. The chain composition adapts such that the variation of melting point of membranes follows the same direction of changes in either temperature or pressure. Lipid compositions are influenced by other thermodynamic variables such as the chemical potentials of solvents, as well.

Part I

Ab initio calculation of biological systems:

Physico-Chemical properties of DPPC and DPPE

3 The SIESTA method for *ab initio* Order-N simulation

3.1 Introduction

Towards the end of the last century, with steady increasing computational powers, much effort has been devoted to progress in the simulation of molecules and materials with enormous number of atoms with Order-N algorithms, whose computational costs scale only linearly with the number of atoms in the system [**?**], [**?**, **?**, **?**, **?**, **?**, **?**]. However just in the last two decades the emphasis is changing from developing the Order-N methods for classical molecular dynamic approaches [**?**], to establish linear scaling methods for ab initio quantum chemical techniques in which interaction of both ions and electrons constitute the atomic forces [**?**].

Quantum chemical methods are very broad in terms of the approximation and so the establishing of Order-N methods in these field has started from the empirical orthogonal tight-binding [**?**, **?**] as the most simplified one, followed by the *ab initio* nonorthogonal tight-binding and non-self-consistent Harris-functional methods [**?**, **?**], to the most complex and reliable fully self-consistent density functional theory (DFT) methods [**?**, **?**].

In a DFT-like method, the aim is solving the Schrödinger equation, besides the determination of the self-consistent Hamiltonian in Order-N iterations. Much effort was dedicated to the former [**?**, **?**, **?**] using empirical or semi-empirical Hamiltonians but much less so on the latter. Because of the difficulties arising from using plane waves, a localized basis set appears to be the natural choice and explicit use of locality became the key for achieving linear scaling [**?**]. One of the initial proposed approaches is the "blips" of Hernandez and Gillan. In this approach, by using the real space grid method they obtained reliable results for silicon system [**?**]. However this approach is very inefficient in respect of the computational requirements.

With an emphasis on the localized version of this methodology many packages have been established recently, like Gaussian, Amsterdam Density Functional (ADF), Dalton, QChem, Turbomole, Cambridge Analytical Derivatives Package (CADPAC), Vienna Ab-initio Simulation Package (VASP), and so on. Among these methods, SIESTA (Spanish Initiative for Electronic Simulations with Thousands of Atoms) has been introduced as a fully self-consistent density functional formulation, based on a flexible linear combination of atomic orbitals (LCAO) basis set, with essentially perfect Order-N scaling. Using these numerical atomic orbitals, allows extremely fast simulations

by applying a minimal basis set consisting of only a few valence orbitals per atom. On the other hand, the calculations can be done very accurately by including complete multiple-ζ and polarized bases besides off-site orbitals. These aspects of SIESTA, makes it a powerful platform to perform calculations depending on the required accuracy and available computational power [**?**].

The basic Born-Oppenheimer approximation is already considered in developing SIESTA as a DFT based method. Furthermore, the most basic approximations addressed the treatment of exchange and correlation in the Kohn-Sham version of DFT [**?**]. Standard norm-conserving pseudopotentials [**?**] are used to avoid the computations for core electrons and to smooth the valence charge density.

In order to solve these pseudopotentials more efficiently, they are transformed to Kleinman-Bylander form [**?**], as a result only two-center integrals are required to calculate the nonlocal part of the pseudopotential matrix elements [**?**, **?**]. Considering the scalar-relativistic effects, and nonlinear partial-core corrections in treat exchange and correlation in the core region, allows to treat special cases as alkali and metals, where semicore states are required to be included to achieve reasonably precise results [**?**].

Widespread possible parametrization of both the local (spin) density approximation (LDA/LSDA) [**?**] and the generalized gradient approximation (GGA) [**?**] are embedded in the method.

3.2 The LCAO Basis set

One of the key techniques to establish Order-N first principle methods is using the sparse Hamiltonian and overlap matrices [**?**]. In order to achieve the sparse Hamiltonian matrix, one possibility is neglecting the interactions between atoms when they are out of a given scope of neighbors or when the interactions are weaker than a given tolerance. The alternative approach is using the strictly localized basis orbitals, i.e. orbitals that vanish beyond a given cutoff radius $\mathrm{r_c}$ [**?**]. The latter is the preferred option because the localized orbitals constitute the basis set of a Hilbert space and the energy remains variational, which is important because it facilitates the test of convergence with regard to the radius confinement. Moreover, another advantage of using the basis orbitals approach is that numerical stability is ensured even when considering short ranges of localization [**?**]. The atomic orbitals used for this technique are the solution of Kohn-Shams Hamiltonian applied to isolated atoms using the same exchange correlation functional and pseudopotential as for the solid and molecule [**?**, **?**, **?**], or they are obtained directly by modifying the eigenfunctions of the atoms [**?**]. For I^{th} atom in the position $\mathbf{R}_\mathrm{I}$, atomic orbitals are presented as:

$$\phi_{I,lmn}(\mathbf{r}) = \phi_{I,ln}(\mathrm{r}_I)\mathrm{Y}_{\mathrm{lm}}(\hat{\mathbf{r}}_I), \tag{3.1}$$

in which $\mathbf{r}_I = \mathbf{r} - \mathbf{R}_I$, and l and m are the angular momentum labels. To increase the

radial flexibility a number of functions n, with different radial dependence, can be added per angular momentum channel. This is the concept of multiple-ζ. The algorithms used in this method perform all the required calculations numerically [**?**]. A variety of optimization approaches [**?**] can further improve the flexibility of the numerical atomic orbitals, making them both efficient and accurate. In the following sections some of these schemes are briefly explained. The aim is to obtain maximum efficiency whilst maintaining strict localization and keeping the size of the basis orbitals reasonably small. Transferability of the obtained basis sets is sought as well [**?**].

3.2.1 Radial flexibility

Orbital size. The number of orbitals per atom is one of the most important features of the numerical atomic orbitals. To generate the minimal basis set which has one single function per angular momentum, the method introduced by Sankey and Niklewski [**?**] was used as a starting point. Their basis functions are the numerical eigenfunctions of the atomic pseudopotential $\mathrm{V}_l(\mathrm{r})$ which are confined inside a given cutoff radius $\mathrm{r_c}$ (i.e. $\phi_l(\mathrm{r}_l^{\mathrm{c}}) = 0$).

In the context of SIESTA [**?**], higher-ζ functions are introduced to have more complete basis sets. The obtained orbitals are based on the split valence idea of quantum chemistry [**?**, **?**]. This method consists of adding a new basis function to each basis orbital which accurately reproduces the tail of the original orbitals from a given matching radius $\mathrm{r}_l^{\mathrm{dz}}$ outwards. Inside the split radius, $\mathrm{r}_l^{\mathrm{dz}}$ the form of these orbitals have a simple polynomial behavior:

$$\phi_l^{\mathrm{dz}}(\mathrm{r}) = \begin{cases} \mathrm{r}^l(a - b\mathrm{r}^2) & \text{if } \mathrm{r} < \mathrm{r}_l^{\mathrm{dz}} \\ \phi_l^{\mathrm{sz}}(\mathrm{r}) & \text{if } \mathrm{r} \geq \mathrm{r}_l^{\mathrm{dz}} \end{cases} \tag{3.2}$$

where a and b are chosen to ensure the continuity of the function and its derivative at $\mathrm{r}_l^{\mathrm{dz}}$. Within exactly the same Hilbert space, a further modified orbital can be defined as the difference between the smooth one $\phi_l^{\mathrm{sz(r)}}$ and the original, which gives a basis orbital strictly confined within the matching radius $\mathrm{r}_l^{\mathrm{dz}}$, i.e., smaller than the original orbitals. This is illustrated in Figure 3.1.

Orbital range. In order to obtain sparse Hamiltonian and overlap matrices for linear scaling algorithms, (Pseudo-) atomic orbitals are considered as the basis set. (Pseudo-)atomic orbitals, which are the DFT solution of the atom with the pseudopotential, are strictly localized by a spherical potential wall [**?**]. For the basis sets made of strictly localized orbitals, a single parameter that defines the confinement radii of different orbitals can be conceptualized as the orbital energy shift $\Delta\varepsilon$, i.e. the energy increase experienced by each orbital when confined to a finite sphere. In this way both the accuracy and the computational efficiency in the calculations is ensured by defining all radii in such a way that a balance between heigh precision results and a reasonable computational cost is obtained [**?**].

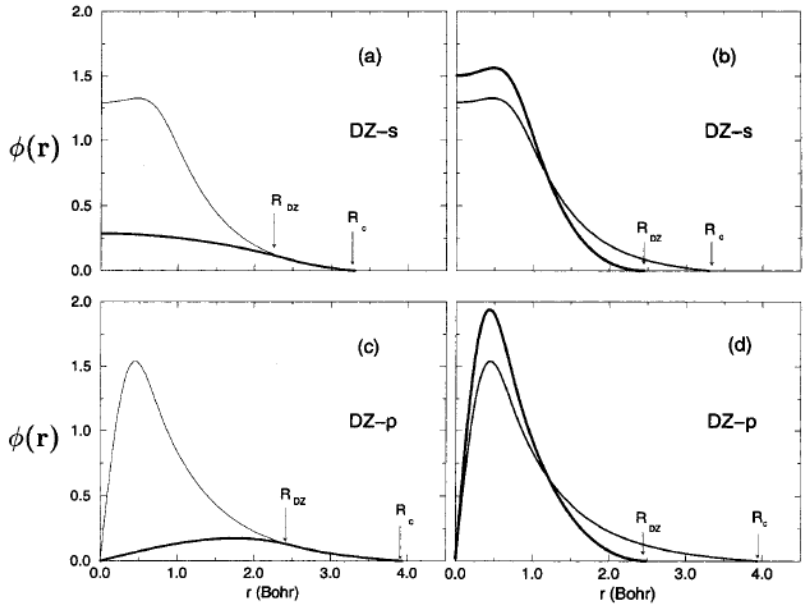

Figure 3.1: Schematics of confined pseudoatomic orbitals for oxygen. (a) and (b) show orbital s, and (c) and (d) show orbital p. R_c is the confinement radius obtained for $\Delta E_{PAO} = 250$ meV. The thinner lines depict the original pseudoatomic orbitals. Thicker lines illustrate the split smooth functions in plots (a) and (c) and represent double-ζ orbitals in plots (b) and (d). The plots were taken from [**?**].

Orbital Shape. Another aspect of the basis orbitals which can be fine-tuned is the orbital shape. The first and most important consideration is keeping the consistency between the pseudopotential and core region. Furthermore, the shape of orbitals is also affected by the ionic character of the atom since orbitals tend to shrink in cations but swell in anions. All these issues have been addressed in different ways. For SIESTA, it has been considered introducing δQ in the basis-generating free-atom calculations which aims to increase the adaptability of orbitals to a variety of ionic situations [**?**].

3.2.2 Angular flexibility

Polarization orbitals. To consider the effects of bond formation, polarization orbitals are required. Traditionally, one or more shells with higher angular momentum are added to polarize the most extended atomic valence orbitals l, however this is not a satisfactory method because of the unbounded extension of these empty atomic orbitals. Another possibility is using the Gaussian atomic orbitals which have maximum overlap with valence orbitals. This is a common procedure within quantum chemistry [**?**, **?**]. Among these approaches, SIESTA developers used the numerical orbitals resulting

from the actual polarization of the pseudoatom in the presence of a small electric field. They considered a valence pseudoatomic orbital $\phi_{lm}(\mathbf{r}) = \phi_l(\mathrm{r})\mathrm{Y}_{lm}(\hat{\mathbf{r}})$, with no higher unbounded shell. Then a small electric field ε in the z-direction is applied to polarize the valence atomic orbital. The consequence of applying the first-order perturbation theory is that the $l+1$ orbitals are produced which polarize the valence orbitals. The range of the polarization orbitals is directly related to the range of the orbitals they polarize. Regarding geometries, energy measurements and vibrational properties, it has been generally found that standard DZP basis orbitals have a similar accuracy to GGA functionals [**?**]. In addition, the standard DZP basis orbitals give convergent results of a satisfactory level, comparable to those resulting from plane-wave calculations.

3.2.3 Transferability

A crucial point as to the usefulness of basis orbitals is their transferability. The aim is looking for optimal orbital basis sets to be transferred to other systems without displaying a decrease in performance. Otherwise, new basis sets must be established for every system studied. As demonstrated in [**?**] the basis orbital method seems to give satisfactory results with regard to transferability.

So far, the definition and development of the LCAO basis set used in SIESTA have been described. In the following section, the Order-N operations for solving the Hamiltonian in the space spanned by the LCAO basis set will be addressed.

3.3 Order-N solution

Once the Kohn-Sham Hamiltonian matrix in the LCAO basis has been computed for a given charge density, we attempt to solve it within Order-N algorithm. In order to find the solutions, we are facing to two problems. First, the orthogonalization procedure and performing the standard iterations to find the solution are done through the N^3 scaling performances. The second, the Hamiltonian eigenvectors are extended over the whole system and overlap with each other. To tackle these problems, a method was firstly proposed by Mauri [**?**] and Ordejón [**?**, **?**]. A modification of this method, which was later done by Kim [**?**], was implemented in the code. To compute the band structure energy $\mathrm{E_{BS}}$ (accumulation of occupied eigenvalues), a modified band energy functional [**?**, **?**, **?**] is minimized with respect to the electronic orbitals Ψ_i, by means of a conjugate gradients (CG) algorithm, to yield $\mathrm{E_{BS}}$.

This modified band energy functional is defined in the form

$$\mathrm{E_{BS}} = 2\sum_{i,j}^{\mathrm{M}} (\mathrm{H}_{ij} - \eta \mathrm{S}_{ij})(2\delta_{ij} - \mathrm{S}_{ij}) + \eta N, \tag{3.3}$$

where the two stands for spins and N is the number of electrons. $H_{ij} = \langle\Psi_i|H|\Psi_j\rangle$, and $S_{ij} = \langle\Psi_i|\Psi_j\rangle$ are the Hamiltonian and overlap elements between the wave functions. The sum is over a set of functions equal or larger than the number of occupied states ($N/2$). The total charge is controlled by the Fermi level parameter η.

The elimination of the orthogonalization is the first step to achieve an Order-N scaling. By using this approach the minimization proceeds without any need to orthonormalize the electron states Ψ_i. In fact the orthogonality, as well as the correct normalization (unity below η and zero above it), results from the minimization of the modified functional with respect to variations of the wave functions Ψ_i. This is because, in contrast to the Kohn-Sham functional, E_{BS} is designed to penalize any nonorthogonality [**?**]. The Kohn-Sham ground state, with all the occupied Ψ_i orthonormal, is also the minimum of Equation(3.3), at which $E_{BS} = E_{KS}$.

To face the second problem, the minimization of the functional in Equation(3.3) is restricted to wave functions which are localized in space. These are Wannier-like wave functions centered on the positions of atoms in the system, and vanish beyond a given cutoff radius R_c (different from the cutoff of the LCAO basis orbitals r_c). The locality of the these wave functions provides a linear scaling algorithm. This R_c is a variational parameter which controls the accuracy of the calculation, and it is the only approximation involved in the Order-N solution of the Hamiltonian.

Once the wave functions solution of the Hamiltonian have been obtained with the Order-N functional, a new Kohn-Sham Hamiltonian is built from the new charge density, and the procedure is iterated until self-consistency is achieved [**?**]. At this point, the energy and atomic forces can be evaluated.

3.4 Calculation of the total energy

After the band energy has been minimized and the localized wave functions obtained, the new charge density is computed, completing a so-called self consistent field (SCF) cycle. From the density, a new Hamiltonian is produced, the procedure being repeated until self-consistency in the charge density or the Hamiltonian is achieved. At this point, the total energy can be computed as the sum of a band structure energy E_{BS} and some correction terms. The band structure is the sum of the energies of the occupied states Ψ_i. The energy E_{BS} can be calculated trough an Order-N algorithm as it was explained in Section 3.3. The correction terms are simple functionals which can be obtained from the electron density and the atomic positions. The Kohn-Sham total energy can then be written as

$$E_{tot} = E_{BS} - \frac{1}{2}\int V_H(\mathbf{r})\rho(\mathbf{r})d^3\mathbf{r} + \int [\epsilon_{XC}(r) - V_{XC}(r)]\rho(\mathbf{r})d^3\mathbf{r} + \sum_{I<J}\frac{Z_I Z_J}{R_{IJ}}, \qquad (3.4)$$

where I, J are atomic indices, $R_{IJ} = |R_J - R_I|$, Z_I, Z_J are the valence ion pseudoatom

charges and $\epsilon_{\rm XC}({\rm r})\rho(\mathbf{r})$ is the exchange correlation energy density. In order to avoid the long-range interactions of the last term, we construct from the local pseudopotential $\mathrm{V}_I^{\rm local}$, which has an asymptotic behavior of $-\mathrm{Z}_I/\mathrm{r}$, a diffuse ion charge, $\rho_I^{\rm local}({\rm r})$, whose electrostatic potential is equal to $\mathrm{V}_I^{\rm local}({\rm r})$:

$$\rho_I^{\rm local}({\rm r}) = -\frac{1}{4}\nabla^2 \mathrm{V}_I^{\rm local}({\rm r}). \tag{3.5}$$

Notice that we define the electron density as positive, and therefore $\rho_I^{local}(r) \leq 0$. Then, we write the last term in Equation(3.4) as

$$\sum_{I<J} \frac{\mathrm{Z}_I \mathrm{Z}_J}{\mathrm{R}_{IJ}} = \sum_{I<J} \mathrm{U}_{IJ}^{\rm local}(\mathrm{R}_{IJ}) + \sum_{I<J} \delta\mathrm{U}_{IJ}^{\rm local}(\mathrm{R}_{IJ}) + \sum_I \mathrm{U}_I^{\rm local}, \tag{3.6}$$

where $\mathrm{U}_{IJ}^{\rm local}$ is the electrostatic interaction between the diffuse ion charges in atoms I and J, and $\delta\mathrm{U}_{IJ}^{\rm local}$ is a small short-range interaction term to correct for a possible overlap between the soft-ion charges, which appears when the core densities are very extended. $\mathrm{U}_I^{\rm local}$ is the fictitious self-interaction of an ion charge (notice that the first right-hand sum in Equation(3.6) includes the $I = J$ terms):

$$\mathrm{U}_{IJ}^{\rm local}(|\mathrm{R}|) = \frac{1}{2}\mathrm{U}_{II}^{\rm local}(0), \tag{3.7}$$

Defining $\rho_I^{\rm NA}$ from $\mathrm{V}_I^{\rm NA}$, analogously to $\rho_I^{\rm local}$, we have that $\rho_I^{\rm NA} = \rho_I^{\rm local} + \rho_I^{\rm atom}$, and Equation (3.4) can be transformed, after some rearrangement of terms, into:

$$\begin{aligned} \mathrm{E}_{\rm tot} &= \sum_{\mu\nu}(\mathrm{T}_{\mu\nu} + \mathrm{V}_{\mu\nu}^{\rm KB})\rho_{\mu\nu} + \frac{1}{2}\sum_{IJ}\mathrm{U}_{IJ}^{\rm NA}(\mathrm{R}_{IJ}) + \sum_{I<J}\delta\mathrm{U}_{IJ}^{\rm local}(\mathrm{R}_{IJ}) - \sum_I \mathrm{U}_I^{\rm local} \\ &\quad + \frac{1}{2}\int \delta\mathrm{V}_{\rm H}(\mathbf{r})\rho(\mathbf{r})\mathrm{d}^3\mathbf{r} + \int \mathrm{V}^{\rm NA}(\mathbf{r})\delta\rho(\mathbf{r})\mathrm{d}^3\mathbf{r} + \int \epsilon_{\rm XC}(\mathrm{r})\rho(\mathbf{r})\mathrm{d}^3\mathbf{r}, \end{aligned} \tag{3.8}$$

where $\mathrm{V}^{\rm NA} = \sum_I \mathrm{V}_I^{\rm NA}$ and $\delta\rho = \rho - \sum_I \rho_I^{\rm atom}$. $\mathrm{U}_{IJ}^{\rm NA}(\mathrm{R})$ is a radial pairwise potential that can be obtained from$\mathrm{V}_{\rm IJ}^{\rm NA}(\mathrm{r})$ as a two-centre integral.

Finally, Equation(3.8) is the total-energy equation actually used by SIESTA, its meaning may be further clarified if the $I = J$ terms of $1/2\sum_{IJ}\mathrm{U}_{IJ}^{\rm NA}(\mathrm{R}_{IJ})$ are combined with $\sum_I \mathrm{U}_I^{\rm local}$ to yield

$$\begin{aligned} \mathrm{E}_{\rm tot} &= \sum_{\mu\nu}(\mathrm{T}_{\mu\nu} + \mathrm{V}_{\mu\nu}^{\rm KB})\rho_{\mu\nu} + \frac{1}{2}\sum_{I<J}\mathrm{U}_{IJ}^{\rm NA}(\mathrm{R}_{IJ}) + \sum_{I<J}\delta\mathrm{U}_{IJ}^{\rm local}(\mathrm{R}_{IJ}) + \sum_I \mathrm{U}_I^{\rm atom} \\ &\quad + \frac{1}{2}\int \delta\mathrm{V}_{\rm H}(\mathbf{r})\rho(\mathbf{r})\mathrm{d}^3\mathbf{r} + \int \mathrm{V}^{\rm NA}(\mathbf{r})\delta\rho(\mathbf{r})\mathrm{d}^3\mathbf{r} + \int \epsilon_{\rm XC}(\mathrm{r})\rho(\mathbf{r})\mathrm{d}^3\mathbf{r}, \end{aligned} \tag{3.9}$$

where

$$\mathrm{U}_I^{\mathrm{atom}} = \int_0^\infty (\mathrm{V}_l^{\mathrm{local}}(\mathrm{r}) + \frac{1}{2}\mathrm{V}_I^{\mathrm{atom}}(\mathrm{r}))\rho_I^{\mathrm{atom}}(\mathrm{r})4\pi\mathrm{r}^2\mathrm{dr}, \tag{3.10}$$

is the electrostatic energy of an isolated atom.

The last three terms in Equation (3.8) are calculated using the real-space grid. In addition to getting rid of all long-range potentials (except that implicit in $\delta\mathrm{V}^{\mathrm{H}}(\mathrm{r})$), the advantage of Equation (3.8) is that, apart from the relatively slowly varying exchange correlation energy density, the grid integrals involve $\delta\rho$, which is generally much smaller than $\rho(\mathrm{r})$. Thus, the errors associated with the finite grid spacing are drastically reduced. Critically, the kinetic energy matrix elements can be calculated almost exactly, without any grid integrations.

3.5 Atomic forces and stress calculation

Molecular dynamics simulations and geometrical optimizations required calculation of atomic forces. In SIESTA atomic forces are obtained by direct derivation of $\mathrm{E}_{\mathrm{tot}}$ (Equation (3.9)) with respect to the atomic positions. It is possible to compute the forces simultaneously with $\mathrm{E}_{\mathrm{tot}}$. Calculating the forces from direct differentiation of total energy implies that, the Pulay-like correction is considered automatically [**?**]. It is important because the basis set is not complete and moves with the atoms. The force on atom i is:

$$\begin{aligned}\mathbf{F}_i &= -\sum_{\mu\nu}\rho_{\mu\nu}\frac{\partial \mathrm{H}^0_{\mu\nu}}{\partial \mathbf{R}_i} + \sum_{\mu\nu}\mathrm{E}_{\mu\nu}\frac{\partial \mathrm{S}_{\mu\nu}}{\partial \mathbf{R}_i} - \frac{\partial \mathrm{U}_{ii-ee}}{\partial \mathbf{R}_i} \\ &\quad +2\sum_{\mu}\rho^0_{\mu}\langle\frac{\partial\phi_\mu}{\partial \mathbf{R}_i}|\mathrm{V}^{\delta}_{\mathrm{H}}|\phi_\mu\rangle \\ &\quad -2\sum_{\mu\nu}\rho_{\mu\nu}\langle\frac{\partial\phi_\mu}{\partial \mathbf{R}_i}|\mathrm{V}^{\delta}_{\mathrm{H}} + \mathrm{V}_{\mathrm{XC}}|\phi_{\mathrm{mu}}\rangle.\end{aligned} \tag{3.11}$$

where $\mathrm{H}_0 = \mathrm{p}^2/2\mathrm{m} + \mathrm{V}_{\mathrm{NL}} + \mathrm{V}_{\mathrm{NA}}$, and $\rho_{\mu\nu}$ and $\mathrm{E}_{\mu\nu}$ are the density and energy-density matrices, respectively [**?**]. The first three terms are calculated interpolating the table data, whereas the last two terms are computed by numerical integration in the grid, as was done for the matrix elements of the Hartree and exchange correlation potentials in the Kohn-Sham Hamiltonian [**?**]. By definition, the stress tensor is the derivative of total energy with respect to strain tensor

$$\sigma_{\alpha\beta} = \frac{\partial \mathrm{E}_{\mathrm{tot}}}{\partial \epsilon_{\alpha\beta}}, \tag{3.12}$$

where α and β are Cartesian coordinate indices. During the deformation, all vector positions, including those of atoms and grid points (and of course lattice vectors), change according to

$$r'_\alpha = \sum_{\beta=1}^{3} \delta_{\alpha\beta} + \epsilon_{\alpha\beta} r_\beta. \tag{3.13}$$

The shapes of the basis functions, Kleinman-Bylander (KB) projectors and atomic densities and potentials do not change, but their origin is displaced according to Equation(3.13). The change in E_{tot} is essentially due to these position displacements, and therefore the calculation of the stress is almost perfectly parallel to that of the atomic forces, thus being performed in the same sections of the code.

However, there are three exceptions to this parallelism. The first concerns the change of the volume per grid point or, in other words, the Jacobian of the transformation (3.13) in the integrals over the unit cell. The second special contribution to the stress lies in the fact that, as we deform the lattice, there is a change in the factor $1/|r - r'|$ of the electrostatic energy integrals. And finally, special stress contribution arises in GGA exchange correlation, from the change of the gradient of the deformed density $\rho(r) \rightarrow \rho(r')$. Precise explanations can be found in [**?**].

3.6 Conclusions

SIESTA platform was presented as one of the first fully operational Order-*N* implementations of DFT. The scientific and technical requirements of the code which enable it to calculate all terms of the DFT Hamiltonian and to solve the Schrödinger equation in strictly Order-*N* operations were briefly discussed. In summary, the SIESTA method provides a very general and rich scheme to perform a wide range of calculations from very fast to very accurate, depending on the simulation's demands. Benefitting from Order-*N* operations, besides very optimized methods to run the program, SIESTA allows DFT simulations of a massive number of atoms of almost every type of materials and system structures. It is therefore considered that SIESTA is an appropriate package for the study of lipids with a significant number of atoms, which the current work is specifically concerned with.

4 Molecular and electronic structure of phospholipids

4.1 Introduction

Phospholipid membranes are essential functional and structural components of cells that are involved in numerous cellular physico-chemical processes occurring within the cells or between them. Despite the apparent importance of membrane electrostatic behavior for the functioning of membranes, insights into the electronic structure of the phospholipid membrane are scarce. Specifically, the magnitude, the orientation and the origin of the dipole potential remain amongst the least understood aspects of the biological membrane [?, ?, ?, ?, ?, ?, ?, ?, ?, ?]. The differences in the reported values for the surface potentials are considerable and sometimes of the same order of magnitude as the potential itself. These problems are difficult to address because of the complexity of membrane systems [?]. Some of the experimental techniques, which have been used for studying biological systems with their specific limitations, will be presented in the following.

This work aims to address the above mentioned gaps in the understanding of lipids. To this end, this chapter will report the results of the electronic calculations, which were done in order to find the precise chemical and electronic structures of DPPC and DPPE. The investigations of the influence of the interfacial water molecules on both the molecular structure and electronic properties of DPPC will be reported as well.

4.1.1 Experimental methods and their limitations

A typical membrane lipid comprises hundreds of atoms. The amphiphilic lipids are the most prevalent particles inside the membranes, therefore they are responsible of several membrane functions. It is important to understand how they are arranged with respect to the other lipids or proteins. Numerous experimental approaches are now available for exploring the structure and function of biological molecules and cellular components.

One of the primary techniques for determining the relative positions of the various atoms is the X-ray diffraction. Although the X-ray diffraction is a promising technique for studying the structure of biological molecules, it does suffer from the disadvantage that the molecules have to be investigated in an environment other than the natural

environment in which they normally operate. Especially, hydrated phospholipids are difficult subjects for structural investigations. To be able to apply the X-ray diffraction technique, a large number of molecules should be crystalized to perform an ordered arrangement of molecules in which the individual molecules are surrounded by their identical molecules. The structure of the benchmark lipid, DPPC, has been studied with X-ray diffraction with limited success [**?**]. The main obstacle in elucidating the structure are fluctuations that lead to smearing of the Bragg peaks [**?**].

The technique of nuclear magnetic resonance (NMR) permits investigation of biological molecules in their natural environments, and in this respect it can be said to complement the X-ray method. However, NMR spectroscopy of DPPC vesicles and the bilayer has turned out to be challenging due to broad spectral line widths and quadrupolar splitting [**?**].

Electron spin resonance (ESR), and optical spectroscopic techniques have been applied to gain structural insight into hydrated DPPC as well. The reported structural parameters of phospholipids by these methods have significant uncertainties. Each technique has its own drawbacks. For example, the optical spectroscopy is helpful, but since it is indirect, it needs consistent input from theory.

4.1.2 Application of the first principle approach in the force field extending

Classical simulations have proven useful in studying systems, which are experimentally difficult to investigate, such as lipid membranes, by providing a quantitative basis for better understanding of them. Nevertheless, classical simulations are affected by imperfections in the force fields [**?**]. Several methodological studies were devoted to validation of the different force fields used in bilayer simulations. For instance, the average area per lipid defined in constant pressure or zero tension simulations, is a parameter which is most often used to define the quality of the force field. Area per lipid is one of the most fundamental properties of a lipid bilayer and one of the most common ways to determine whether the bilayer system has reached equilibrium. When the area per lipid reaches a stable value, other structural properties (density distributions, NMR order parameters) do not change either. Simulated area per lipid can be also compared with experimental values available from X-ray or neutron diffraction and volumetric data. Because of these reasons, it is important to perform a general method for obtaining this key parameter precisely.

Ab initio calculations are, in principle, able to address these challenges [**?**]. However, due to the inherently large system size, first principle treatments were not feasible to this date, given the non-linear scaling of the computational effort with the system size. Just recently, the linear scaling version of density functional theory (DFT) with localized Wannier-like wave functions has been developed, which makes such calculations feasible [**?**]. The algorithm, which was explained in the previous chapter, is based on the concept

of locality and uses a modified energy functional, which avoids direct wave function orthogonalization. For a system composed of N atoms, the computational complexity is reduced from Order-N^3 to nearly Order-N [**?**, **?**].

4.2 DPPC molecular structure

In the present study, the structure of DPPC was investigated under different degrees of hydration using the first principle method, which is implemented in the SIESTA software [**?**]. In the following, details of the simulation will be explained. Subsequently, the results for the relaxed structure of the referenced lipid, DPPC will be reported. Finally, the results obtained for the electronic structure of this phospholipid will be explained. Furthermore, the same properties of the second most important phospholipid, i.e. DPPE, were also examined and will be briefly reviewed.

4.2.1 Technical details of the ground state calculation

In order to calculate the ground state structure of a DPPC monomer, the molecule was first built by putting atoms together in such as way that the number of valence electrons of each of the atoms and their hybridizations were respected. The Troullier-Martins type pseudopotentials [**?**] were used along with a double-ζ single polarized basis set as implemented in the density functional code SIESTA (see [**?**] and Chapter 3). By applying this basis set, two confined orbitals are used for each magnetic quantum number m in the valence shell of every chemical element. Polarization orbitals are added to obtain a more precise description of the deformation of the atomic orbitals, if the atoms are part of the molecule. For example, for the carbon atoms (which are all part of the molecule), this choice results in 13 basis functions, 8 double-ζ functions, and 5 polarization orbitals.

The local density approximation (LDA) was used as the exchange correlation energy functional, with Ceperley-Alder parametrization [**?**]. Although, in some cases, even for nonmagnetic elements, it has been shown that LSDA can give better results in comparison with LDA [**?**], it happened not to be the case in the present calculations. The generalized gradient approximation (GGA) was not also applied because, in a molecular structure, steep changes in electronic charge density are in general not expected. Later it will be discussed that the solutions obtained from LSDA, GGA and LDA were basically identical. The mesh cutoff is set to 450 Ry constants, which was the smallest value above which the ground state energy as a function of the mesh-cutoff is found to become almost constant.

Among various local minimization methods, the conjugate gradient scheme, which is one of the most reliable and efficient algorithms, was used to find the ground state of present complexes. The density matrix tolerance was set to be 10^{-6}. It means that when the maximum difference between the output and the input on each element of

the density matrix in a self-consistent cycle is smaller than the mentioned threshold, the charge density is considered to have converged. In order to avoid any local minima in the energy landscape, the maximum displacement of the atoms was set to a large value of 0.5 Bohr in each conjugate gradient step. The molecule was relaxed until the maximum force on the atoms fell bellow 0.005 eV/Å.

4.2.2 Pure DPPC structure

In order to find the minimum energy structure of a DPPC lipid, since only a single molecule was considered, the length of the unit cell vectors were set to a much longer value than the size of the molecule. The cell vectors which used for performing the calculation of a DPPC molecule was set to $20 \times 40 \times 20$ $\mathring{A}^3$, which in every side was almost as twice as the extension of the molecule in that direction. Consequently, only the Γ point in the reciprocal space for energy integration was considered in the calculation. In order to determine the ground state of the hydrated lipids, the first step was to obtain the relaxed structure of a single water molecule with the same simulation parameters. The configurational properties of a DPPC molecule relaxed to its minimum energy state are presented in Tables 4.1 and 4.2. In order to provide researcher with the accurate result of this work, coordinates of the relaxed structure of a bare DPPC are presented in Appendix A.

4.2.3 Hydrated DPPC structure

In order to investigate the effect of the surrounding aqueous environment on changing the molecular structure of the DPPC lipid, a few number of lipid-water complexes have been constructed. For this purpose, the replicas of the water molecules were placed around the relaxed structure of a DPPC monomer in the vacuum, in such a way that the water molecules thoroughly covered the hydrophilic head group of DPPC. Then, systems were relaxed to their minimum energy state, through the procedure was above mentioned. The influence of watery environment on the lipid configurational properties was investigated by adding various number of water molecules to the system, including 20, 36, 50 and 75 water molecules per lipid.

Upon hydration, it was found that DPPC undergoes a dramatic long-range conformational change (Figure 4.1 and Table 4.1). With 50 water molecules [**?**, **?**], the head group of the lipid and the proximal tail region are fully covered. The glycerol plane rotates and assumes a parallel orientation with respect to the plane of the tails and the glycerol backbone lines up with the sn_1 chain with an angle of 171.4°. The sp^2 planes of sn_1 and sn_2 carbonyls make an angle of about 23.8°, and the carbonyl groups take an anti-parallel orientation (Table 4.2). These conformational rearrangements lead to a change in the compaction of the structure (Table 4.1). By increasing the number of water molecules to 75, the conformation of the lipid was not significantly altered. A pure DPPC has been commonly referred to as a cylindrical molecule [**?**]. However, in

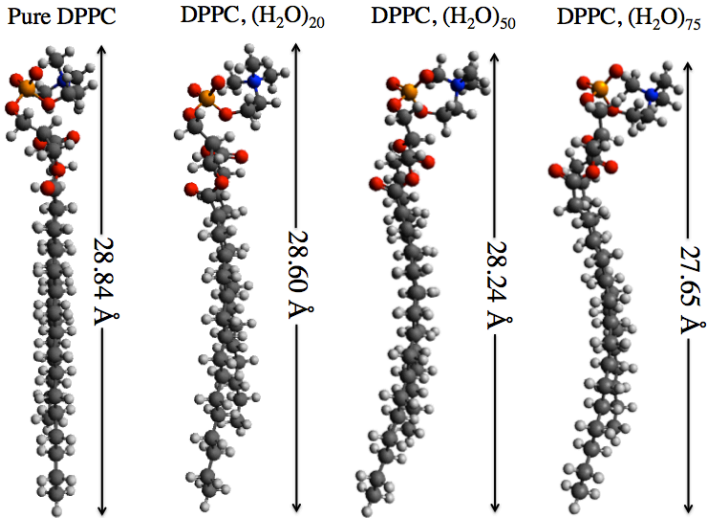

Figure 4.1: The minimum energy configurations of pure DPPC and hydrated DPPC. The effect of water molecules are clarified by bending the hydrophobic chains. Water molecules are not displayed in order to allow a clearer visualization of the lipid configurations.

the present study it was found that the ground-state shape (at zero temperature) of the hydrated DPPC differs from a cylindrical geometry and adopts a sickle-like overall shape (Figure 4.1) with tail bending angles of about 24° and 14° relative to the molecular axis of non-hydrated DPPC.

This conformational rearrangement is favored because it allows water chains to bridge the oxygen atoms of the lipid. Water-lipid interaction energy was estimated to be about −0.20 eV (−19.30 kJ/mol) for a DPPC system with 50 water molecules by producing 11 water-lipid H-bonds. This estimation was obtained by separating the water cluster from the lipid part and comparing the energy of the the two parts with the energy of the system (see subsection 4.2.5). Thus, the energy difference also includes the interaction energy of the water cluster with the electric field of the lipid.

To gain further understanding about the mechanistic basis underpinning the conformational changes, the number of water molecules was reduced to 20 and the resulting structure of DPPC was calculated. The hydration which corresponds to 20 water molecules was found to be sufficient to hydrate the hydrophilic parts of the lipid head and build water bridges. Indeed, the phosphate and ester group oxygens form hydrogen bonds similar to what is found with full hydration and the water chains connecting the groups occurred. Therefore, with partial hydration, a similar conformational rearrangement and overall shape modification was found. The configurational characteristics of DPPC under different levels of hydration are summarized in Tables 4.1 and 4.2.

	Linear extension ($\mathring{A}$)	Ellipsoid radii of head ($\mathring{A}$)		Ellipsoid radii of tails ($\mathring{A}$)	
		a_x	a_z	a_x	a_z
DPPC	28.84	7.62	4.26	6.91	4.17
DPPC, $(H_2O)_{20}$	28.60	7.64	4.79	7.25	5.72
DPPC, $(H_2O)_{50}$	28.24	7.23	5.72	7.83	4.09
DPPC, $(H_2O)_{75}$	27.65	7.64	6.10	7.93	6.03

Table 4.1: Structural parameters of DPPC and hydrated DPPC. The x-axis lies in the plane of the tail, the y-axis is the long axis of the lipid and the z-axis is perpendicular to the tail plane.

	Glycerol	$sp2$ of sn_1 carbonyl	$sp2$ of sn_2 carbonyl
DPPC	124.04	160.26	77.00
DPPC, $(H_2O)_{20}$	135.72	115.08	77.39
DPPC, $(H_2O)_{50}$	153.76	102.97	49.01
DPPC, $(H_2O)_{75}$	150.39	78.16	58.86

Table 4.2: Angle between the normal of the specified planes with the normal of the tail plane. The *sn1* carbonyl refers to which positioned along the tail, while the *sn2* carbonyl refers to which is located perpendicular to the hydrocarbon chains.

4.2.4 Dimer DPPC structure

The structure of two neighboring DPPC molecules (2-DPPC) with associated water molecules were studied to gain a better understanding about the influence of the neighboring lipids. To obtain the ground state structure of the hydrated double DPPC monolayer, two relaxed DPPCs were placed parallel to each other, with opposite dipole moment vectors. Then, the head part of this structure was covered by $N_{H_2O} = 64$ water molecules. The full system was again relaxed with the same procedure as was explained for a pure DPPC. The sample was also considered as a cluster.

Bearing in mind the experimental area per lipid value in a lipid membrane, the unit cell vectors were arranged so that the dimer with water molecules made a periodic structure. Then, another relaxation with periodic boundary conditions was executed, this time also allowing relaxation of the unit cell. Since, in this case, a "crystal" was under consideration, a $3\times3\times1$ grid in the reciprocal lattice for k-grid sampling sampling was used. In the final relaxation step, the lipids were tilted and the relaxed configuration was reached (Figure 4.8). The maximum force was again less than 0.005 eV/Å, and the maximum stress tensor element was less than 0.25 GPa. The target pressure was set to be 0.0 GPa.

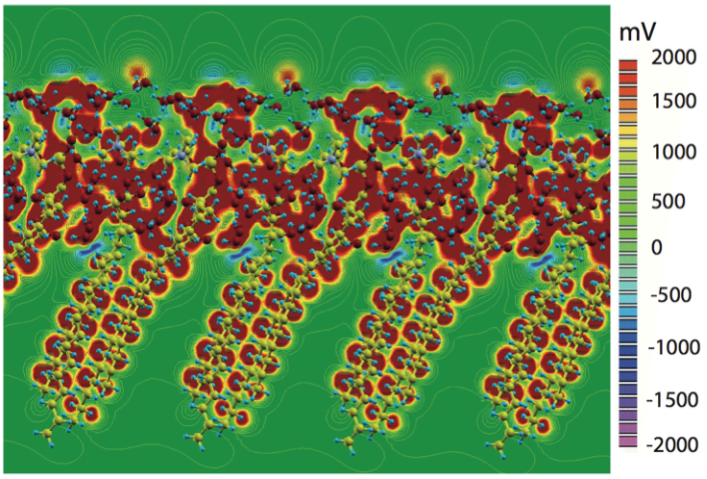

Figure 4.2: Tilted gel-phase type structure of relaxed hydrated double DPPC, with 32 water molecules per lipid. The tilt angle is about 28 degrees.

Under relaxation of the dimer DPPC, it was observed that the two DPPC molecules adopt an orientation in which the dipole moments are in a nearly anti-parallel arrangement and the two tail planes face each other (Figure 4.3). In this arrangement the tail plane of one of the lipids convexes towards the other one. The results of this study are in agreement with previously reported experimental evidence for long-range cooperative distortion of lipid tails [**?**]. In a minimum energy configuration, units of 2-DPPC are expected to pack in such a way that the dipole-dipole interactions are most favorable (Figure 4.3). The area per lipid is found to be about 46 $\mathring{A}^2$. For the hydrated DPPC membrane, this value is in agreement with experimentally measured values in tilted gel phase as well as classical simulations of the system [**?**, **?**, **?**, **?**].

A further stage in the examination was the investigation of the nature of intermolecular interaction in hydrated 2-DPPC. It was observed that two water bridges connect the sn_2 carbonyls of the two DPPCs, in accordance with previous studies [**?**]. The carbonyl groups and the two water bridges adopt a nearly planar geometry. The hydrated 2-DPPC complex is stabilized by the dipole-dipole interactions, water bridges and van der Waals interaction of the tails. Based on these observations, it is proposed that the 2-DPPC complex can be considered as the structural unit of the DPPC membrane. This assumption is in agreement with previous studies [**?**, **?**, **?**, **?**] including X-ray diffraction studies, where the reported super lattice unit cell of DPPC contains two lipid molecules [**?**].

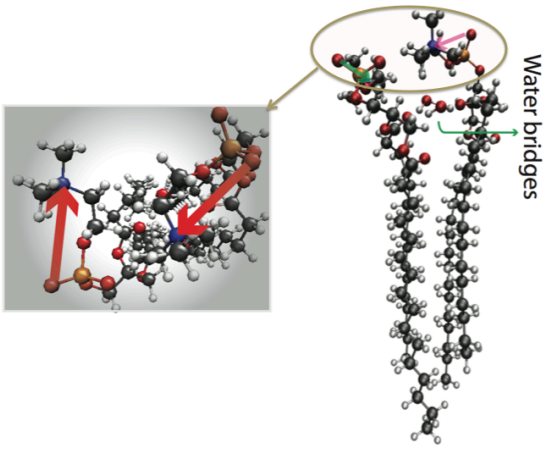

Figure 4.3: Two antiparallel lipids are proposed as the structural unit in the DPPC membrane. The Double DPPC structure is simulated under two-dimensional periodic boundary conditions. The area per lipid is calculated to be 46 $\mathring{A}^2$. Water molecules are not displayed in order to allow a clearer visualization of the lipid configurations.

4.2.5 Hydration energy estimation

To further understand the contribution of different interactions to the stability of the hydrated 2-DPPC complex, the energy of the water bridges was estimated. The hydration energy for the complex is calculated as follows:

$$\mathrm{E} = -\frac{1}{n}\left[\mathrm{E}(\mathrm{DPPC},(\mathrm{H_2O})_n) - \mathrm{E}_{\mathrm{BSSE^{CP}}}(\mathrm{DPPC}) - \mathrm{E}_{\mathrm{BSSE^{CP}}}((\mathrm{H_2O})_n)\right], \tag{4.1}$$

where n is the number of water and E denotes the total energy. The basis set superposition error (BSSE) was dealt with using the counterpoise method (CP) [**?**] by applying ghost atoms, namely by removing the atoms but keeping the basis functions of them. For example, in the case of $\mathrm{E}_{\mathrm{BSSE^{CP}}}(\mathrm{DPPC})$, the water molecules were removed, but the basis functions were retained and computed for the total energy calculation of the lipid. To estimate the contribution of two water bridges to the stability of the hydrated 2-DPPC, the stabilization energy was calculated by:

$$\begin{aligned} \mathrm{E} \;=\; & -\frac{1}{2}[\mathrm{E}(\mathrm{2DPPC},(\mathrm{H_2O})_{n-2}(\mathrm{H_2O})^*{}_2) \\ & -\mathrm{E}_{\mathrm{BSSE^{CP}}}(\mathrm{2DPPC},(\mathrm{H_2O})_{n-2}) - \mathrm{E}_{\mathrm{BSSE^{CP}}}((\mathrm{H_2O})^*{}_2)]. \end{aligned} \tag{4.2}$$

The star superscripts denote the water bridges. It was found that the removal of the bridges destabilizes the system by ~ 2.05 eV(-197.79 kJ/mol) per water bridge.

4.2.6 Contribution of van der Waals interactions

An important consideration in the total energy of the system is van der Waals (vdW) interaction, which is generally necessary between two parallel DPPC molecules within a unit cell, the neighboring unit cells, and even among the tails of a single DPPC. The vdW interaction was taken into account during the calculations in order to determine its potential effect on the results.

To assess the potential effect of vdW interactions, corresponding simulations were also performed using vdW functionals, based on the [**?**, **?**], for the hydrated DPPC and hydrated double DPPCs, which allowed comparison with the results illustrated in Figure 4.1. Apart from small local differences, the structures were basically the same. For example, the difference between the angle joining the tilted tails of the lipid in the vdW calculation (155°) and the reported LDA calculation (156°) was less than 0.7%. The difference between the length of the lipid in the vdW calculation (28.30 $\mathring{A}$) and the reported LDA calculation (28.24 $\mathring{A}$) was less than 0.3%. In the case of the hydrated double DPPC, the total energy of the system was about 1.2% lower when the vdW functional was used. The structure of the hydrated double DPPCs system showed little changes and the electric dipole was found to be very close to the LDA value which was about 0.48 D.

4.2.7 GGA and LSDA vs. LDA

Examination of the relaxation of DPPC molecules with different levels of hydration and the 2-DPPC complex as the unit structure of a monolayer was also carried out using more accurate approximations. To address exchange correlation functionals, the local spin density approximation (LSDA) and the generalized gradient approximation (GGA) were used. Following the explanations about LSDA and GGA approximations in subsection 4.2.1, similarly to the use of the vdW functionals, only minor differences were observed. It can therefore be concluded that calculations using LDA are sufficiently accurate.

In the next section of this chapter, the electrical properties of hydrated DPPC and hydrated DPPC monolayer type are examined to gain insight into the structure-function relationship. It is also interesting to consider the structure of hydrated DPPE and this will be briefly overviewed in the next section

4.3 Electronic structure of DPPC

In this section, the relation between the structure and the electrical properties of the single and dimer DPPCs are addressed. As the first step, the estimated charge density profile of pure DPPC lipid is demonstrated. Electronic dipole and quadrupole moments of the head part of pure DPPC is calculated and the effect of water in changing the magnitude and orientation of these quantities are investigated. In addition, some of

these electrostatic parameters for hydrated DPPE were obtained and are presented, as well. This section also deals with the electrostatic potential resulted from the lipids, which is still among the quantities that are of computationally challenging. In order to perform the purposed measurements, the ground state configuration of corresponding systems, which was obtained in the previous section, were applied.

4.3.1 Charge density profile

The charge density profile of non-hydrated DPPC was estimated as one of the most useful electrical properties of every system. Once the minimum energy configuration was reached, the valence pseudocharge density of the system at every mesh point was computed. In the referenced software applied to perform the calculation of this study, the number of the valence pseudocharges in a volume unit of $Bohr^3$ is calculated as the charge density at the mesh. To estimate the charge density in every local point along the lipid length, a disc with negligible thickness 0.078 $\mathring{A}$ was considered. Then, the charge density was calculated by averaging over the disc. The calculated charge density, which is shown in Figure 4.4.a, is in perfect agreement with the electron density profile from X-ray studies [**?**, **?**, **?**]. The total charge density was obtained by sum of the ionic (resulted from psudopotentials) and valence charge density at the mesh, (Figure 4.4.b). Unsurprisingly, the head group carries a high charge density in the vicinity of the phosphate oxygen and the quaternary nitrogen. However, the centers of positive and negative charges do not coincide perfectly with the phosphorus and nitrogen atoms. Therefore, estimation the dipole and quadrupole moments of the system would have been instructive to gain deeper understanding about lipids under investigation.

4.3.2 Electronic dipole and quadrupole moments

Electronic dipole and quadrupole moments of a DPPC in pure and hydrated state and also in the vicinity of another lipid were computed as other electronic properties of these systems. Measurements of the charge density within the system of a single DPPC showed a slight difference between the position of the positive and negative charge centers and the position of the PO^- and N^+ compositions. In the same way, the orientation of the electric dipole, p, was estimated to be approximately about $\Phi = 56.51°$ and $\Theta = 18.34°$ (from the plane of the head), while for the $PO^- - N^+$ vector in the identical system, the orientation was approximately about $\Phi = 65.69°$ and $\Theta = 18.66°$. The electric dipole of DPPC was calculated to be about 10.30 Debye (D). Hence, the dipole moment of DPPC is almost 5 times larger than that of a water molecule with about 1.85-2.6 D [**?**, **?**, **?**]. The $PO^- - N^+$ dipole was around 21.30 D ($d \sim 4.43$ Å). According to these results, it seems that the absolute value of charges around the atoms N^+ and PO^- are distributed in space, resulting in smaller charge concentration around these atoms.

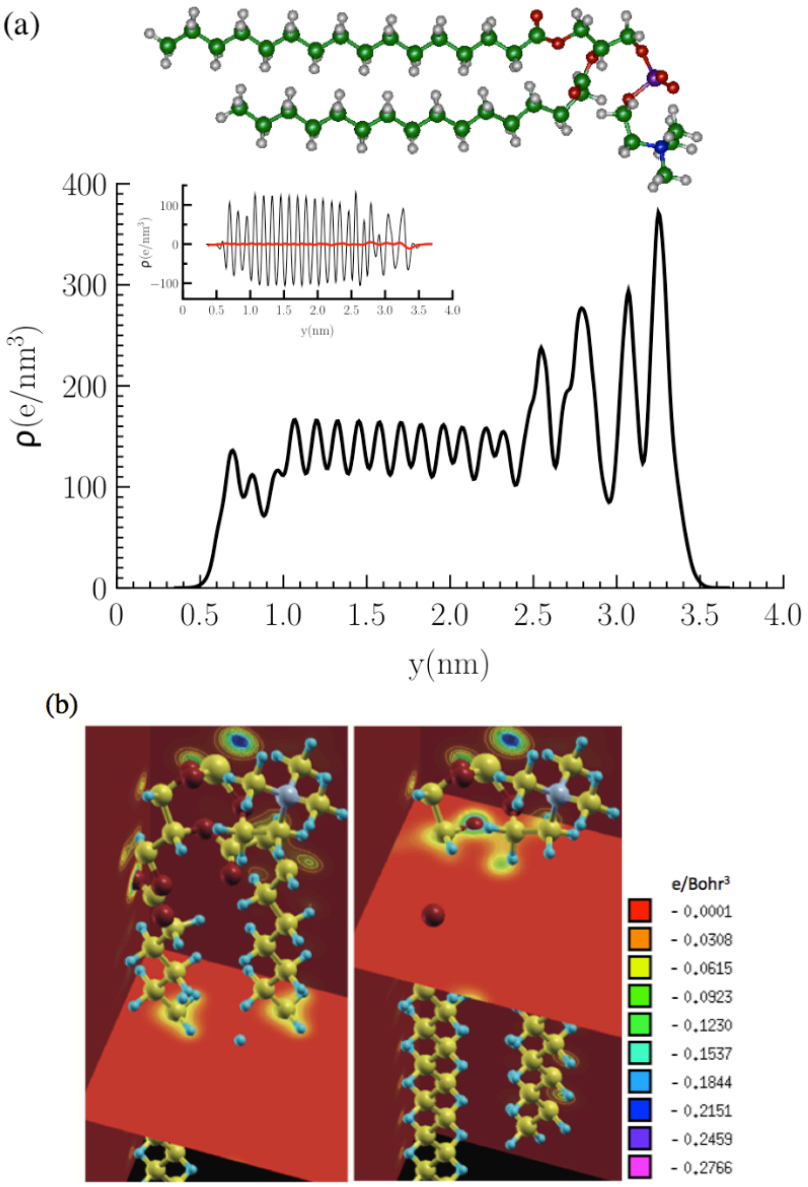

Figure 4.4: Plot (a) shows the electron charge density along the long axis of the pure DPPC. The electron density was calculated by taking the average over the disc with a thickness equals 0.078 $\AA$. The inset indicates the total charge density along the long axis of the lipid and its average. Plot (b) shows cross sectional views of the total charge density of the same system.

As for the electrical properties of hydrated DPPC, the presence of water leads to a conformational change in the entire molecule and the electric moments were therefore expected to be affected. The $PO^{-}-N^{+}$ distance was reduced by nearly 0.9 $\mathring{A}$ to 3.558 $\mathring{A}$ in hydrated DPPC with 20 water molecules. The conformational change induced by the anisotropic hydration causes an increase ($> 80\%$) in the dipole moment of the full system, bringing it to 18.42 D.

As the number of water molecules was increased from 20 to 50, the dipole moment was reduced to 9.87 D. The reason is that the dipole moments of the isotropically oriented molecules are canceled. In Figure 4.5, how the orientation of electrical moments have changed by hydrating the lipid head part are shown. For DPPC with 75 water molecules, a dipole moment of about 10.42 D was calculated which again was in agreement with experimental reports [**?**, **?**]. For 2-DPPC with 64 water molecules, a net electric dipole of about 0.48 D was found. The electric dipole moment of DPPE was also estimated to be about 8.52 D, which is less than the dipole moment of a DPPC molecule. It is noteworthy that the distribution of charge density is more diffuse in hydrated DPPC as compared to pure DPPC, which causes higher order electric moments to become significant (Table 4.4). This implies that hydrated DPPC interacts with the electric field gradient in its environment and it influences its interaction with ions.

It was also found that the single DPPC has an electric quadrupole moment, Q. The quadrupole tensor for the single DPPC was also calculated with respect to the center of mass of lipid and its results are compared with the electric quadrupole moment of hydrated DPPC. The result is given in Table 4.4. The magnetic dipole moment was negligible for both single and hydrated systems.

Molecule	Electric dipole (D)
Pure DPPC	10.30
Pure DPPC (PO^{-} – N^{+})	21.30
DPPC,$(H_2O)_{50}$	9.87
DPPC,$(H_2O)_{75}$	10.42
2DPPC,$(H_2O)_{64}$	0.48
DPPE,$(H_2O)_{50}$	8.52
Water	$\sim 1.85 - 2.6$

Table 4.3: Electric dipole moments measured in different systems.

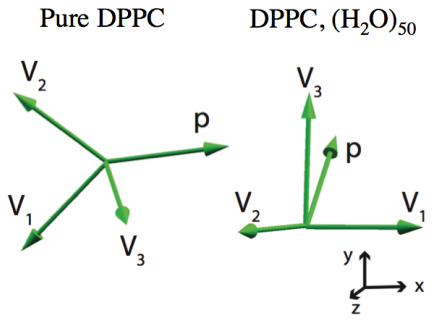

Figure 4.5: Electric dipole moment p and eigenvectors of the quadrupole moment Q are illustrated for DPPC and hydrated DPPC ($N_{H_2O} = 50$). The y-axis coincides with the long axis of the lipid and the x-axis lies within the plane of the tails of the lipid. The rotation of the electric dipole and quadrupole moments due to the effect of the hydration is clear in the figure.

DPPC			DPPC,$(H_2O)_{50}$		
-33.6962	-200.8788	-87.0458	144.7582	-10.0254	32.9994
-200.8788	-58.16953	-55.2874	-10.0254	-252.0582	13.7930
-87.0458	-55.2874	91.8657	32.9994	13.7930	107.2999

Table 4.4: Electric quadrupole tensor Q ($ea_0{}^2$) with respect to center of mass, for a single DPPC and DPPC,$(H_2O)_{50}$ complex.

4.3.3 Surface electric potential

Figure 4.6 presents the electric potential profile of DPPC with calculated equipotential lines. The total electrostatic potential (surface potential) is defined as the sum of the Hartree potential plus the local pseudopotential, at the mesh points, which are used to calculate the real-space quantities (e.g. charge density). Similarly, measurements carried out for hydrated DPPE lipid, and the results is depicted in Figure 4.7.

The surface potential fluctuates between positive and negative values along the normal to the lipid surface and within the surface with 0.5 nm spacing. Therefore, a sensor scanning the surface or approaching the surface along the normal will sense positive or negative potential values depending on its position. Figure 4.8 displays the surface potential of a DPPC monolayer type structure illustrating the inhomogeneities of the electrostatic potential at the membrane surface. This spatial fluctuation of the potential may account for some of the seemingly contradictory experimental reports on the membrane surface potential [?, ?, ?, ?, ?, ?, ?, ?, ?, ?]. This study can be extended to other lipids that together with PC define the electrical properties of cellular membranes.

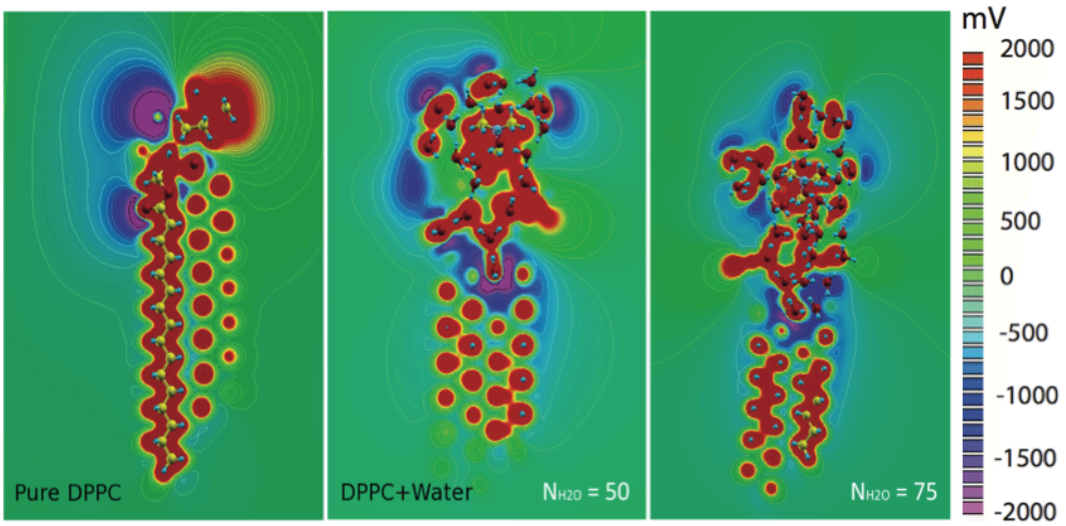

Figure 4.6: The calculated surface potentials are presented by equi-potential lines for DPPC with $N_{\mathrm{H_2O}} = 0, 50, 75$. The color coding scheme is the same in all panels.

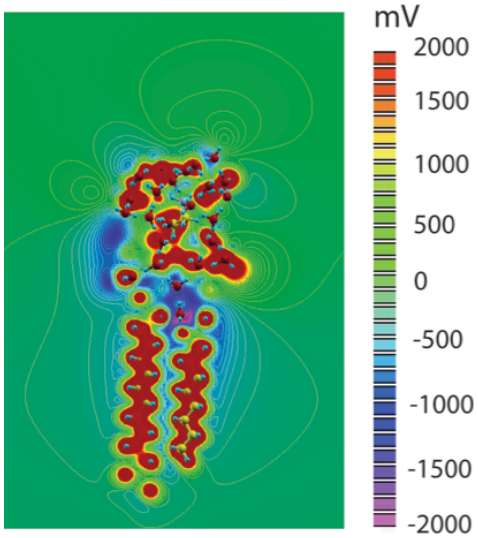

Figure 4.7: The calculated surface potential of DPPE with 50 water molecules.

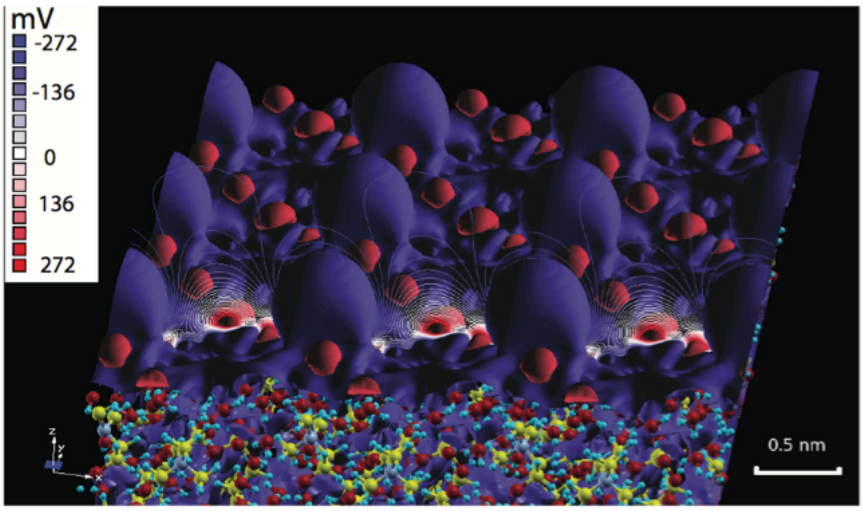

Figure 4.8: Surface potential of DPPC monolayer type structure. The inhomogeneities of the electrostatic potential at the surface is illustrated in the figure.

4.3.4 Electronic density of states of DPPC and DPPE

The electronic density of states (DOS) of a DPPC lipid with different levels of hydration was calculated (Figure 4.9). By using the profile of density of states, the band gaps between the HOMO and LUMO states can be estimated. For DPPC, a reduction in the energy gap upon hydration was observed which is in agreement with experimental findings [**?**, **?**, **?**]. The energy gaps for pure DPPC and water-DPPC complexes are tabulated in Table 4.5. A comparison between the electronic DOS of DPPC,$(H_2O)_{50}$ and DPPE,$(H_2O)_{50}$ complexes are illustrated in Figure 4.10. The results show a slightly higher energy band gap estimated for DPPE with respect to DPPC.

Phospholipid	Energy band gap (eV)
DPPC	4.20
DPPC,$(H_2O)_{50}$	3.40
DPPC,$(H_2O)_{75}$	3.35
DPPE,$(H_2O)_{50}$	3.50

Table 4.5: Energy band gap estimates for hydrated DPPC and DPPE. A decrease in the band gap upon the hydration was occurred.

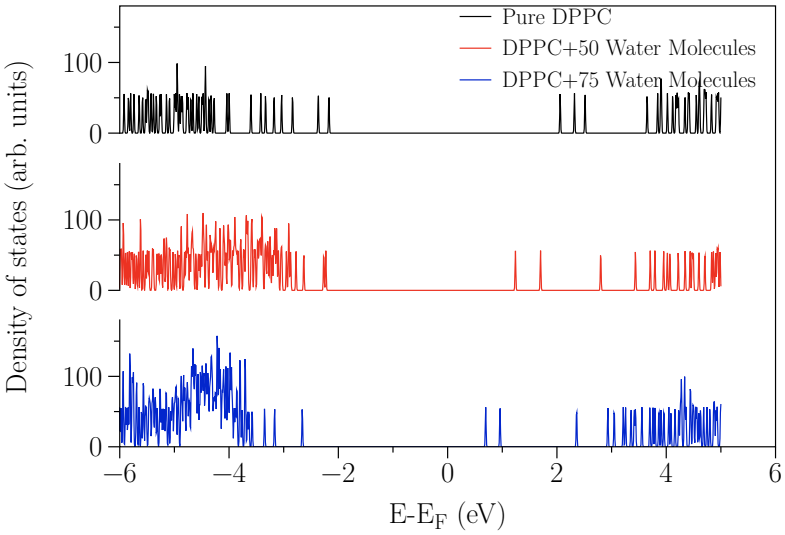

Figure 4.9: Electronic density of states of pure and hydrated DPPC lipids.

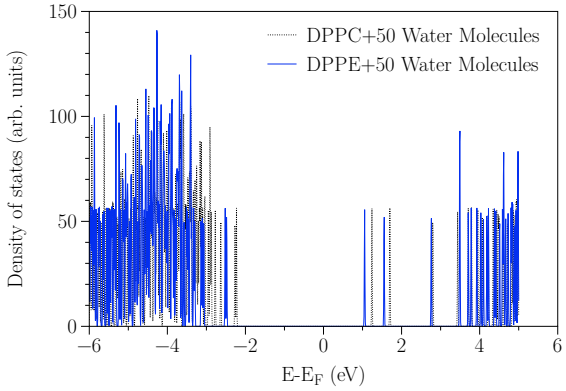

Figure 4.10: Electronic density of states of hydrated DPPC and DPPE lipids.

4.4 Conclusions

In this chapter, the molecular interplay between the lipid and the interfacial water was examined. It was illustrated that upon hydration, the phospholipid undergoes drastic long range conformational rearrangements which lead to a sickle-like ground state shape. In addition, by performing a large scale calculation, which applies the periodic boundary conditions, the influence of neighboring DPPC molecules in a monolayer type configuration was explored. On the basis of this investigation, the structural unit of the tilted gel phase PC appears to be a water-bridged PC dimer. Moreover, it is found that hydration dramatically alters the surface potential, dipole and quadrupole moments of the lipids and consequently guides the interactions of the lipids with other molecules and the communication between cells. By comparing the obtained structure with the existing experimental data, the structural findings are validated. Through the energy consideration, the results of the present study confirm previous X-ray diffraction studies suggesting that the super lattice unit cell of DPPC contains two lipid molecules [**?**].

5 Extended vibrations in membrane lipids

5.1 Introduction

Cell membranes are subject to energy input from various sources such as the sun, exothermic chemical reactions, and mechanical perturbation by the cytoskeleton and the extracellular matrix. To understand the stability and functioning of membranes, it is thus important to acquire a better understanding of how the membrane deals with this influx of energy. An important role is played by the water molecules hydrating the membrane phospholipid molecules [**?**, **?**]. Therefore, to gain a deeper understanding of energy transfer phenomena, it is necessary to investigate the molecular mechanisms of energy storage and transfer of the combined phosphoilipid-water system [**?**]. This is also highly relevant in nanotechnology where membranes are often the soft material of choice for nanoscale devices [**?**]. Obtaining molecular insights into energy transfer in combined lipid-water systems is challenging, as lipid head groups are complex structures, involving hydrophobic patches with an otherwise highly hydrophilic area. Interfacial water on the hydrophilic parts has characteristic structures and dynamics, distinct from those of water layers on hydrophobic surfaces.

Experimentally, progress in the study of assembled interfacial water structures has been made using ultrafast electron crystallography, and it was found that the energy transfer in these structures occurs on ultrashort time scales [**?**]. The energy transfer dynamics of a lipid monolayer interfacing an aqueous environment has also been studied with time-resolved surface sum-frequency generation [**?**]. The results of this study indicated the presence of two distinct categories of water molecules, showing fast and slow energy transfer dynamics, and fast energy transfer across a monolayer of lipids [**?**]. However, a molecular scale assignment of the mechanism behind the energy transfer and the different types of water has remained a challenge [**?**].

Classical approaches (Molecular Dynamics and Monte Carlo simulations) have been extensively used to investigate energy transfer in a wide range of materials with significant success [**?**].

Density functional theory (DFT) treatments are in principle more accurate [**?**, **?**], but have not been feasible for large molecular systems because of the enormous computational cost as a result of the cubic scaling relative to the number of atoms. Here, for the purposes of the present work, those limitations were circumvented by adopting

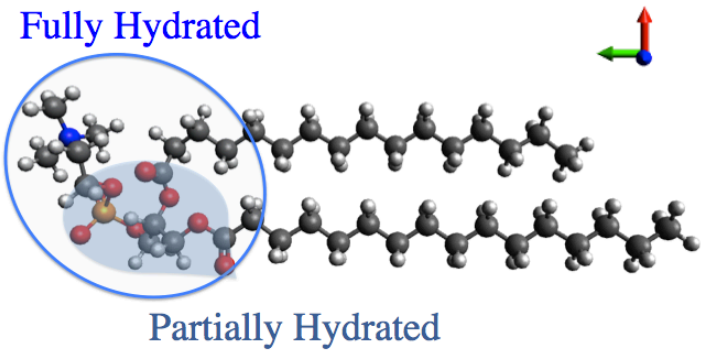

Figure 5.1: Molecular structure of DPPC, under the conditions of fully and partially hydrated head part.

the approach developed recently in the realm of condensed matter physics (see Chapter 3 and [**?**]). On the basis of this DFT scheme, in this work a general framework is developed for accurately calculating the rate of energy transfer for large biomolecular systems. The fruitfulness of such an approach to biomolecular processes was envisioned long ago but left undeveloped until now [**?**]. Through the present work, this approach is examined for lipid-water systems (Figure 5.1). However, it is a general one that can be readily extended to other biomolecular systems. The focus of this chapter is on energy transfer through the most prevalent lipid types in cells, namely phospholipids, with the emphasis on the most abundant phospholipid in the cell membranes; DPPC. The vibrational characteristics were studied within the linear response regime. To gain a better understanding of the theory behind this method, the classical theory of vibration modes of a cluster will firstly be introduced. Then, the *ab initio* calculations for determining vibrational modes of DPPC and water-DPPC complexes, will be discussed. Analyzing of existing modes and the number of atoms, which participate in every mode will be reported thereafter. Finally, a new method to calculate the wavelength will be introduced and consequent phase velocities of the normal modes of various hydrated systems of DPPC found by determined wavelengths, will be presented.

5.2 Theory of vibrational modes of a cluster

In order to investigate the vibrational behavior of a single DPPC and DPPC-water complexes, as these systems are considered as clusters, the theory of vibration frequencies of clusters were applied. According to this theory [**?**], after the general, or one of the local minimum states of the system have been obtained, the potential energy is expanded around the relaxed positions in terms of atomic displacements. Being at one of the local minima, the total force on each atom is expected to be zero, so the linear term

of Taylor expansion of the potential energy is negligible. According to the harmonic approximation all statements with a power greater than two are also negligible. Moreover, the matrix of the second derivatives should all be positive as a consequence of being in the minimum energy configuration. With these approximations the potential energy of the system is given by:

$$\mathcal{U}(\mathbf{r}_1, \cdots, \mathbf{r}_N) = \mathcal{U}_0 + \frac{1}{2} \sum_{\varrho,\varrho'} \kappa_{\varrho,\varrho'} \ \mathrm{q}_\varrho \ \mathrm{q}_{\varrho'}, \tag{5.1}$$

in which $\mathbf{q}$ is the vector of small displacement of atoms from their equilibrium positions ($\mathrm{q}_\varrho(t) = \mathrm{r}_\varrho(t) - \mathrm{r}_\varrho(t_0)$), and the collective index $\varrho = (i, \alpha)$ stands for the Cartesian component α of the displacement vector of the i^{th} atom. For a cluster consisting of N atoms in 3D, ϱ changes from 1 to $3N$. The force constants matrix F, is a $3N \times 3N$ matrix, whose elements represent the second derivative of potential energy at the equilibrium state:

$$F_{\varrho,\varrho'} = \frac{\partial^2 \mathcal{U}}{\partial \mathrm{q}_\varrho \partial \mathrm{q}_{\varrho'}}. \tag{5.2}$$

Given the expression for the potential energy as a function of force constants and displacements, the Newtonian equations of motion are written as:

$$m_\varrho \frac{d^2 \mathrm{r}_\varrho}{dt^2} \simeq -\sum_{\varrho'} F_{\varrho,\varrho'} \mathrm{q}_{\varrho'}(t) \quad (\forall \ \varrho \ \epsilon \{1, \cdots, 3N\}). \tag{5.3}$$

In the linear regime this formula can be interpreted as a harmonic oscillator, as if particles are connected by springs. A harmonic solution for this equation can take the form $\mathrm{q}_\varrho(t) = \mathbf{e}_\varrho \cos(\omega t + \phi)$. By substituting this solution in Equation 5.3 a set of linear equations are obtained which defines the vibrational modes of the system in the amplitudes $\mathbf{e}_\varrho$ and frequencies ω. To make the system of equations symmetric, it is necessary to imply a change of variable by setting $\mathrm{s}_\varrho = \sqrt{m_\varrho} \ \mathrm{q}_\varrho$. The resulting equations for amplitude $\mathbf{e}_\varrho$ are:

$$\sum_{\varrho'} \left(\frac{F_{\varrho,\varrho'}}{\sqrt{m_\varrho m_{\varrho'}}} - \omega^2 \delta_{\varrho,\varrho'} \right) \mathbf{e}_{\varrho'} = 0 \quad (\forall \ \varrho \ \epsilon \{1, \cdots, 3N\}). \tag{5.4}$$

This linear system has a non-zero solution for $\mathbf{e}$ if the determinant of the matrix $F_{\varrho,\varrho'}/\sqrt{m_\varrho m_{\varrho'}} - \omega^2$ is zero. As a result, the eigenvalues of the matrix $F_{\varrho,\varrho'}/\sqrt{m_\varrho m_{\varrho'}}$ are the squares of the vibrational frequencies of the cluster. For a system consisting of N particles in three dimension, the matrix $F_{\varrho,\varrho'}/\sqrt{m_\varrho m_{\varrho'}}$ has $3N$ eigenvalues, six of which will be zero due to pure translations and rotations in the system in a relaxed state. All the remaining eigenvalues are positive, reflecting the fact that the system is in one of its local minima of energy and any configurational deviation from the ground state position results in an increase in potential energy $\mathcal{U}$ of the system. Given the above definitions, the normal modes of the system are defined by eigenvectors with $3N$ components, $\mathbf{e}_\varrho^\lambda$, corresponding to every eigenvalue ω_λ. For every mode λ, the polarization

vector $\mathbf{e}_{\varrho}^{\lambda}$ includes N three-dimensional vectors associated to N atoms of the cluster, representing the amplitude and the direction along which every atom oscillates in the mode.

$$\sum_{\varrho'} \frac{F_{\varrho,\varrho'}}{\sqrt{m_{\varrho} m_{\varrho'}}} \mathbf{e}_{\varrho'}^{\lambda} = \omega_{\lambda}^{2} \delta_{\varrho,\varrho'}. \tag{5.5}$$

These eigenvectors, $\mathbf{e}$, satisfy conditions of orthonormality and completeness:

$$\sum_{\varrho} \mathbf{e}_{\varrho}^{\lambda} \mathbf{e}_{\varrho}^{\lambda'} = \delta_{\lambda,\lambda'} \qquad \text{orthogonality,} \tag{5.6}$$

$$\sum_{\varrho} \mathbf{e}_{\varrho}^{\lambda} \mathbf{e}_{\varrho'}^{\lambda} = \delta_{\varrho,\varrho'} \qquad \text{completeness.} \tag{5.7}$$

Therefore, the displacement of atoms can be expanded by the set of eigenvectors which form a complete orthonormal basis of the $3N$ dimensional space:

$$\mathrm{q}_{\varrho}(t) = \frac{1}{\sqrt{m_{\varrho}}} \sum_{\lambda=1}^{3N} A_{\lambda}\ \mathbf{e}_{\varrho}^{\lambda}\ \cos(\omega_{\lambda} t + \phi_{\lambda}), \tag{5.8}$$

where the $6N$ coefficients $(A_{\lambda}, \phi_{\lambda})$ are determined from the $6N$ initial conditions on positions and velocities of the atoms.

The resulted frequencies can be used to estimate how well a system is stable in a given mode. The presence of negative frequencies shows that the system is not in its ground state. Soft modes with very small ω close to zero, make the system mechanically unstable, and thus leading to a phase transition. In addition, the eigenvectors related to each eigenfrequency is used to explore the polarization of the mode. Further calculations, including mechanical properties of the system, the infrared and Raman active spectra of molecules, are also become feasible to do by using the eigenvectors.

In the following, the *ab initio* calculation for determination of the eigenmodes of the referenced systems will be reported.

5.3 *Ab initio* calculation of vibrational modes

In this section, vibrational modes of biomolecular complexes, formed of a single DPPC molecule and a DPPC with a few water molecules hydrating its head part, are presented. In order to apply the theory of vibration, the relaxed structure of each complex at its ground state should be determined. Taking the approach described in Chapter 4, firstly the minimum energy configuration of a pure DPPC molecule at zero temperature is calculated. The energy transfer in DPPC is expected to occur mostly through

vibrational transitions in the electronic ground state; it is expected not to involve contributions from electronic excitations [**?**]. In the relaxed state, the maximum force exerted on each atom drops below 0.005 eV/$\mathring{A}$.

5.3.1 Vibrational dynamics of pure DPPC

The vibrational spectrum of DPPC is calculated by using the so-called frozen-phonon method. According to this method, once the system ground state is attained, each atom is displaced from its equilibrium position by a small value of 0.2 Bohr in order not to exceed the linear regime limit. Then, the forces exerted on every atom are calculated with the method that has already been discussed in Chapter 3. Once the force of every atom resulted from all other atoms is calculated, the force constant matrix is built. The final step to find the vibrational mode involves diagonalization of the force constants matrix. The eigenvalues of the constants matrix are the frequencies of the system and related vibrational modes are represented by their three-dimensional eigenvectors. The vibrational energy can be transferred by three different types of oscillations. In the present study, T_x refers to the transverse-acoustic modes with vibrations in the plane spanned by the two tails, T_z refers to the transverse-acoustic modes with vibrations perpendicular to this plane, and T_y refers to the longitudinal-acoustic modes with vibrations along the tail chain axis.

The vibrational density of state (phonon DOS) of pure DPPC is given in Figure 5.2. As it is clear from the figure, for a single DPPC, the most active modes are located in frequency range of about $100 < \omega < 1500$ cm^{-1} with the highest peak on frequency $\omega = 1400$ cm^{-1}. Another active area of the vibrational modes of the system belongs to a tiny range of frequencies around $\omega = 3000$ cm^{-1}. The system does not show any vibrational modes in the frequency range of $1600 < \omega < 2800$ cm^{-1}.

So far it has been a challenge, in the case of lipids and other biomolecules, to resolve and assign vibrational modes, particularly at low frequencies. According to the approach described above, all vibrational modes can be assigned. A few examples are given in Figure 5.3 and 5.4. More significantly, the present approach allows to fully assign the vibrational spectrum of hydrated DPPC as well as identifying modes involving the vibration of interfacial water.

5.3.2 Vibrational dynamics of hydrated DPPC

After the vibrational spectrum of a pure DPPC is determined, an intriguing question is how the vibrational dynamics are affected upon hydration of the lipid. To address this question, one DPPC molecule whose hydrophilic head part is partially hydrated (PH) in one case and fully hydrated (FH) in the other case (Figure 5.1), was relaxed to the minimum structure. To hydrate the hydrophilic regions, 20 water molecules were considered to provide a reasonable coverage, while a full coverage is achieved with about

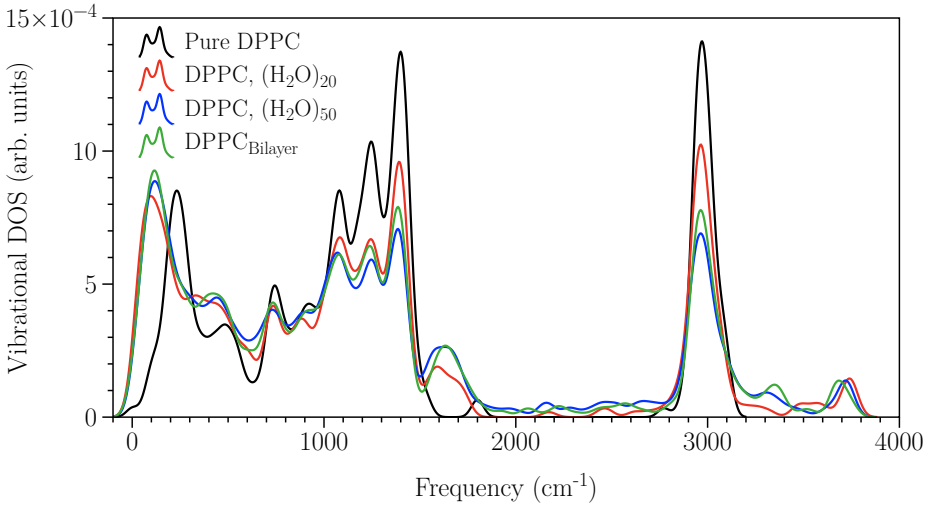

Figure 5.2: Vibrational density of states for DPPC, hydrated DPPCs and hydrated bilayer DPPC.

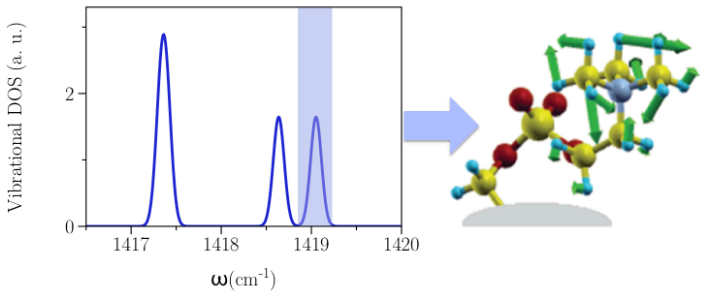

Figure 5.3: One bending mode of CH_2 and CH_3 groups of choline, illustration of the ability to accurately assign the entire density of states.

50 water molecules. Then, the vibrational DOS for DPPC under different degrees of hydration were calculated and are presented in Figure 5.2.

In the presence of water molecules, results confirm a drastic change in the vibrational DOS, including major changes in the low-frequency region $\omega < 500$ cm^{-1}. A red shift in frequency domain of $\omega < 500$ cm^{-1} is clear. Other active regions are also affected upon the hydration of the lipid. This change is obvious in the region from 1000 to 1800 cm^{-1} and in the high-frequency region from 2800 to 3200 cm^{-1}.

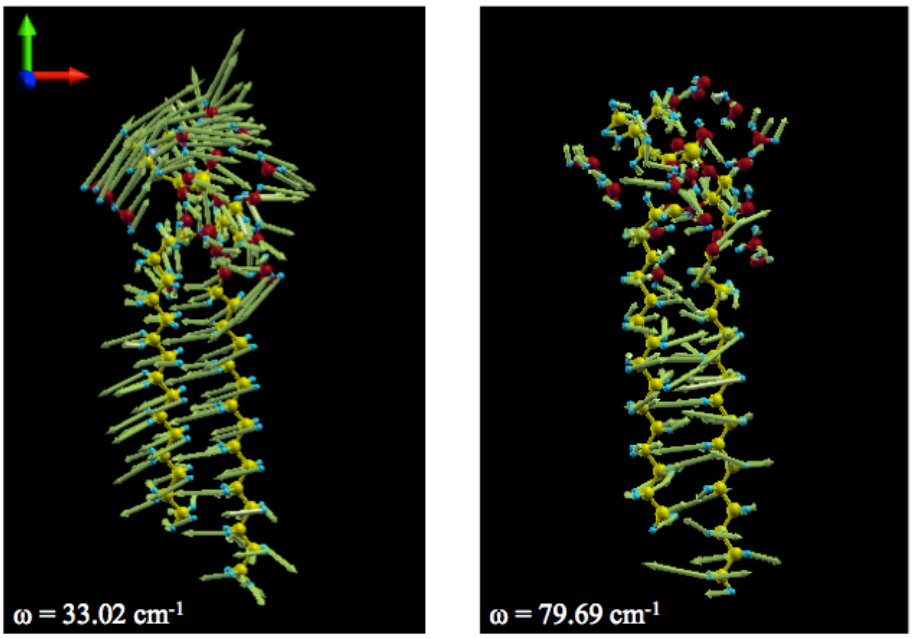

Figure 5.4: On the left, the lipid part of the eigenmode at 33.02 cm^{-1} is shown, which is important in energy transfer along FH-DPPC. On the right, a breathing mode at 79.69 cm^{-1} is displayed. The breathing mode carries thermal energy efficiently within the plane of the membrane.

5.3.3 Vibrational dynamics of hydrated bilayer DPPC

By extending the mentioned analysis, the vibrational density of state of a structural unit of bilayer DPPC can be computed. In this context, the term bilayer refers to two DPPCs located in such a way that their tail regions face each other. To hydrate the bilayer, the head groups of the two lipids were covered with 36 water molecules, which is sufficient to cover the whole head parts.

The ground state configuration of this structure was obtained through the same method as was used for the other molecular systems (see Chapter 4). Following the obtention of the relaxed structure, the eigenvalues of the force constant matrix were calculated to obtain the vibrational modes. The resulting vibrational DOS of the bilayer DPPC is also shown in the Figure 5.2. By looking at the phonon DOS of the bilayer system, no significant change from those of DPPC,$(H_2O)_{50}$ is observed. This implies that the water coverage of the head groups is a determining factor for the observed change in the vibrational mode of the system.

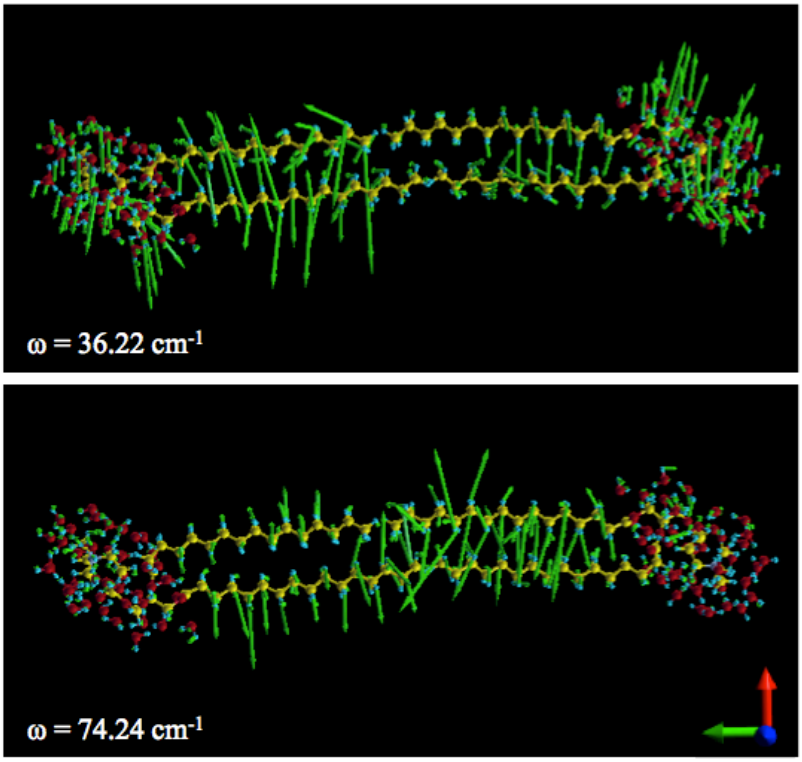

Figure 5.5: In the upper figure one of the extended modes of the bilayer at 36.22 cm^{-1} is displayed. In the lower figure a breathing mode at 74.24 cm^{-1} is shown, where the two lipids are in antiphase.

5.4 Inverse participation ratio

Studying the nature of active vibrational modes in the presence of water molecules makes it possible to gain mechanistic insights into the energy transfer process. A characteristic factor in realizing an active mode, is the number of contributing atoms in that mode, which is quantified by the inverse participation ratio [**?**, **?**]:

$$P^{-1} = \frac{\sum_{i=1}^{N} |e_i^{\omega}.e_i^{\omega}|^2}{|\sum_{i=1}^{N} e_i^{\omega}.e_i^{\omega}|^2} \tag{5.9}$$

where e_i^{ω} is the polarization vector of the i^{th} atom in the mode ω. Obviously, the more the extended mode, the less the inverse participation ratio. For a DPPC-water complex consisting of N atoms P^{-1} is equal to $1/N$, when all N atoms participate in a given mode. This corresponds to the translational zero modes. P^{-1} is equal to 1 when only one atom involved in a mode.

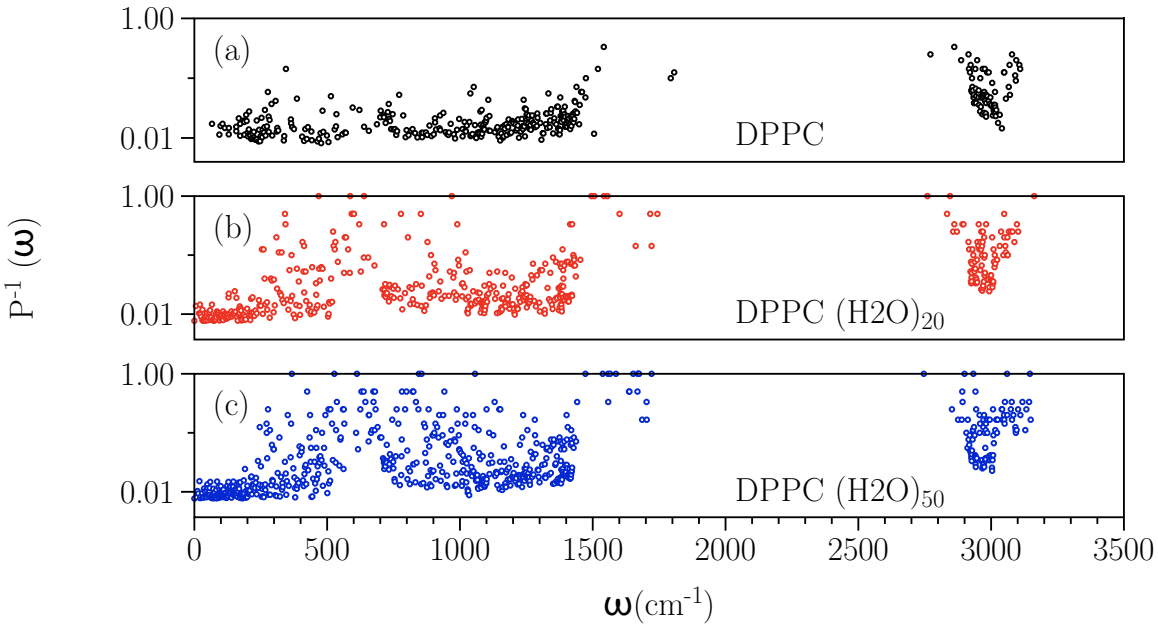

Figure 5.6: Water induces the emergence of low-frequency vibrational modes. The inverse participation ratios for DPPC in (a) the non-hydrated (black), (b) partially hydrated (red), and (c) fully hydrated (blue) DPPC.

5.4.1 Active modes of DPPC

In Figure 5.6 and Figure 5.10, the inverse participation ratios are illustrated for monomer DPPC-water complexes and hydrated bilayer DPPC, respectively. The obtained results show that water molecules substantially influences the number of atoms that contribute to the vibrational modes (Figure 5.6). Intriguingly, the emergence of modes with nearly all atoms involved is observed at frequencies below 250 cm^{-1} (Figure 5.6.b, c).

Quantifying the number of modes with more than 100 involved lipid atoms, while DPPC consists of a total number of atoms equal to 130, shows the profound effect of water in changing the vibrational modes of the system. Fully hydrated DPPC has 102 modes within this range of participation, 5-fold more than non hydrated DPPC with 19 modes. In partially hydrated system, DPPC,$(H_2O)_{20}$, only 69 modes are found with high participation (Figure 5.6.b). In all cases, no such modes exist for $\omega > 1500cm^{-1}$. Interestingly, in the hydrated cases, many modes with less than 20 lipid atoms involved are mostly observed within the frequency range of 500 and 1500 cm^{-1} (Figure 5.9.a). Modes with $P^{-1} > 0.1$ appeared between 1500 to 1700 cm^{-1} and around 3000 cm^{-1}. Thus, hydrated DPPC acts as a low-pass filter for vibrational energy transfer.

Another striking observation with possible implications for intermolecular energy transfer is the emergence of a breathing mode at 79.69 cm^{-1} in DPPC,$(H_2O)_{50}$ complex

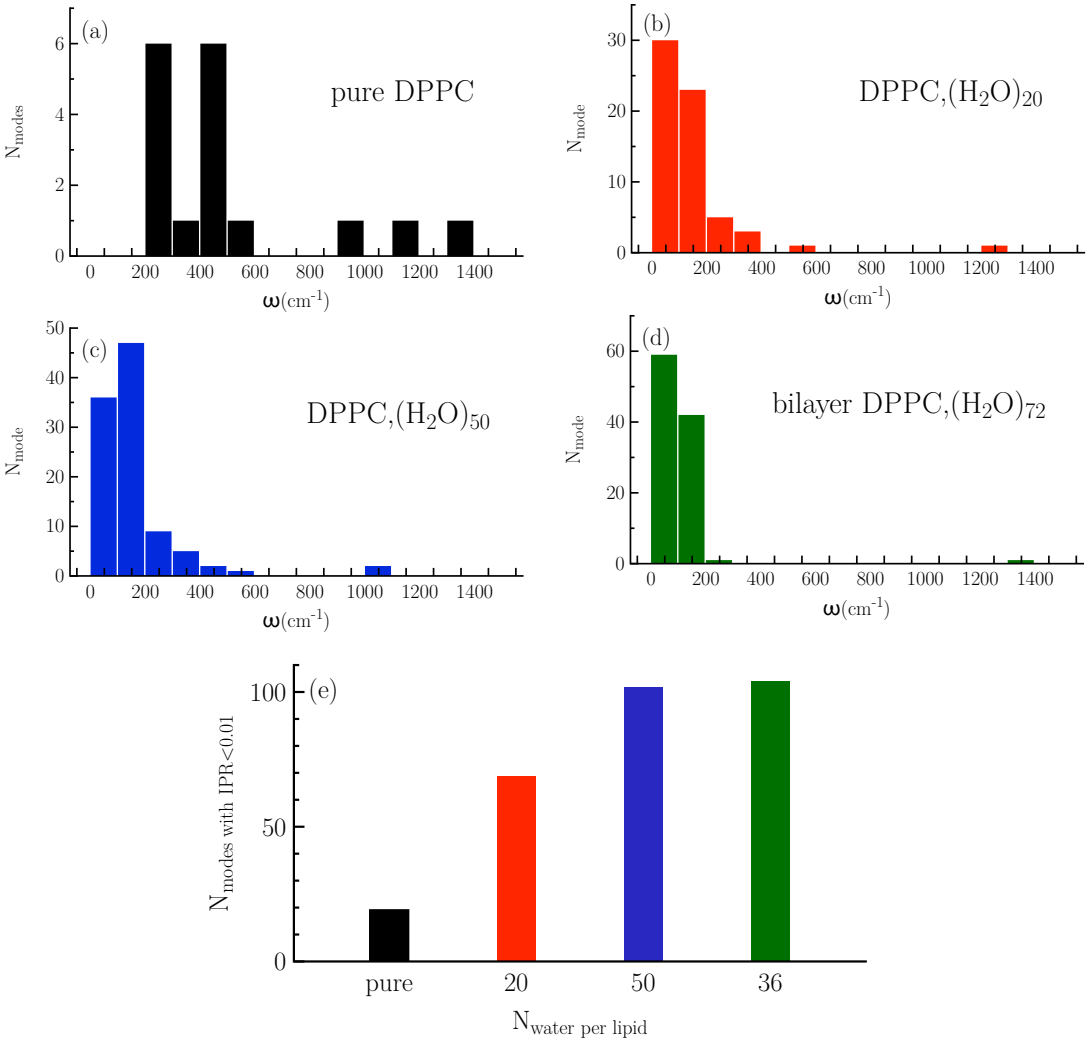

Figure 5.7: Distribution of modes with participation of more than 100 atoms of DPPC in the systems (a) the non-hydrated (black), (b) partially hydrated (red) and (c) fully hydrated (blue) DPPC. Panel (d) shows the distribution of modes with participation of more than 100 atoms per each lipid molecule in the hydrated bilayer DPPC complex (green). In all cases, no such modes exist for $\omega > 1500\text{cm}^{-1}$. Panel (e) demonstrates the number of modes with the inverse participation ratio smaller than 0.01 for the systems listed above. Again, for the bilayer system IPR < 0.01 per lipid molecule was considered.

(Figure 5.4). In this mode the entire tail region contracts and expands periodically in the tail plane, which is represented here by the x-direction. This likely facilitates energy transfer in the plane of the leaflet. In the bilayer DPPC, the breathing mode occurs at lower frequency $\omega = 74.24$ cm^{-1}, (Figure 5.5).

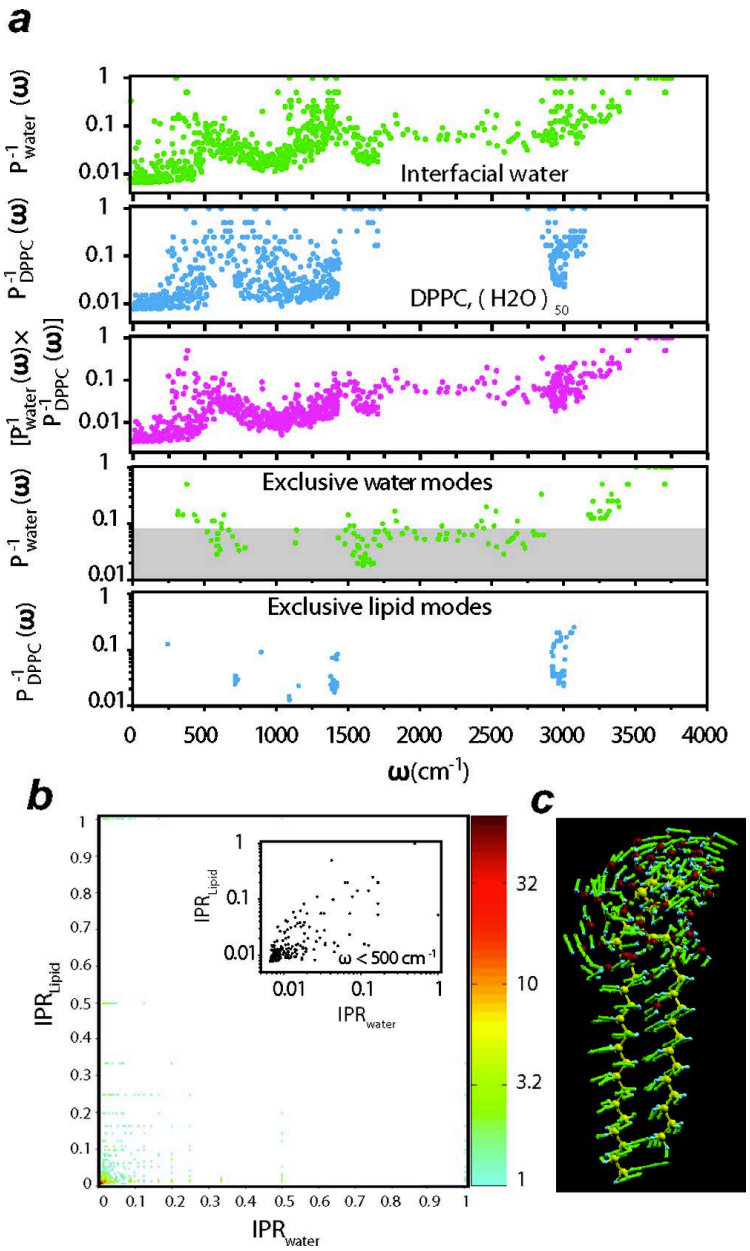

Figure 5.8: (a) Inverse participation ratio of the interfacial water part (first panel) and of the lipid part (second panel) of FH DPPC. The last two panels depict modes that are exclusively water modes (green) and exclusively lipid modes (blue). The gray zone in the fourth panel marks the modes with more than 12 water atoms involved. In panel (b), the correlation of the participation of lipid atoms and water atoms is illustrated. In panel (c) an extended mode (22.04 cm^{-1}) is depicted with a nano-vortex of water.

5.4.2 Active modes of interfacial water

Following the analysis of vibrational modes of DPPC complexs, vibrations of the interfacial water were investigated as well. Previous studies on the vibrational DOS of bulk water, have shown that O−H stretching modes of water molecules appears at frequencies above 3400 cm^{-1} [**?**]. According to this study, the bending mode of water has its maximum at 1650 cm^{-1} with a width of about 200 cm^{-1}. At low frequencies, a two-band feature with peaks near 55 and 170 cm^{-1} has been reported and assigned to vibrations of water multimers. In bulk water, the participation does not exceed 12 atoms and there are no modes involving several tens of water molecules. However, the results of the *ab initio* calculations of the present work indicate a distinctly different behavior of the vibrational modes of the interfacial water of fully hydrated DPPC (Figure 5.8.a). In 554 modes (73% of modes with water involvement), P_{water} exceeds 12, and in 137 modes more than 100 water atoms are involved. The long-range delocalization of these modes originates from the indirect connection of water molecules via the neighboring lipid structure. In 135 modes, the exclusive participation of water atoms is observed. Among all modes, in only 73 modes does P_{water} exceed 12 with a maximum of 55 participating water atoms.

5.4.3 Extended modes of lipid-water complexes

In the present work, the modes with more than 100 involved atoms are called as "extended modes". The modes extending over the lipid and the interfacial water are important in energy transfer processes. The extended modes expose themselves with an intriguing arrangement of vibration arrows, namely, vortex-like (Figure 5.8.c), breathing-like (Figure 5.4.b), and circulating arrangements. The change of dipole moment $d\mu/dq$ associated with these modes renders them amenable to studies by THz spectroscopy. Figure 5.8.b shows that the modes of hydrated DPPC with low P_{lipid}^{-1} are extended over the lipid and the water part with P_{lipid}^{-1} and P_{water}^{-1} smaller than 0.01.

In Figure 5.7, distributions of modes with participation of more than 100 atoms are shown for the non-hydrated DPPC, partially and fully hydrated DPPC. In all cases, no such modes exist for frequency greater than 1500 cm^{-1}.

5.4.4 Active modes of hydrated bilayer like DPPC

The analysis of the vibrational eigenmodes for bilayer systems revealed that at frequencies below 250 cm^{-1}, the vibrational modes are extended over almost all atoms, from both lipids and water molecules on both sides (Figure 5.5). In this frequency region, 104 modes are found in the form of extended modes which is comparable with the number of modes in the DPPC,$(H_2O)_{50}$ complex (Figure 5.7.e). For 193 modes within the frequencies $500 < \omega < 1500$ cm^{-1}, less than 20 atoms per lipid participate in the vibration (Figure 5.9.b). One of the most interesting result arise from these

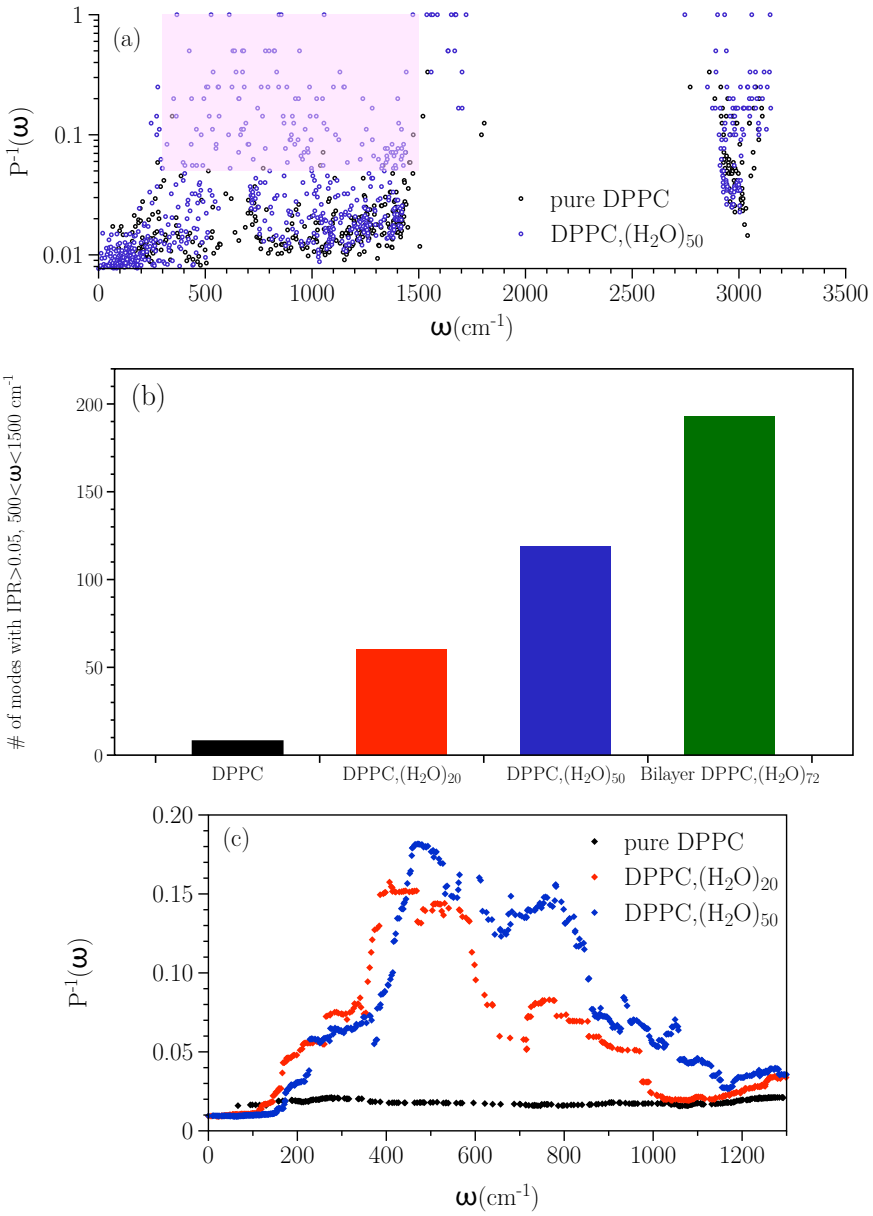

Figure 5.9: Opposite effects of interfacial water on the extension of DPPC modes. Panels (a) and (b) show a drastic increase (∼15-fold) in the number of local lipid modes in the range of 500-1500 cm^{-1} upon full hydration of the lipid. Panel (c) shows the averaged P^{-1} over nearby frequencies vs frequency to illustrate the opposite behavior of interfacial water on modes below 250 cm^{-1} and the modes at higher ω. For non-hydrated DPPC, the averaged P^{-1} is almost constant and independent of frequency for $\omega < 1500$ cm^{-1}.

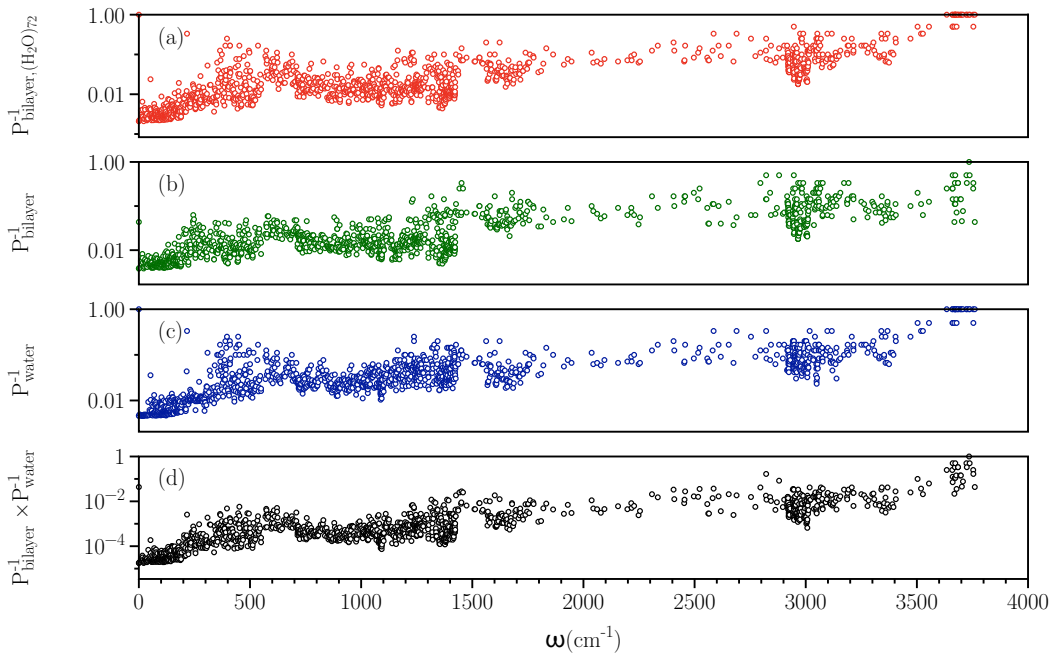

Figure 5.10: Inverse participation ratio of (a) hydrated bilayer, (b) lipid part, (c) the interfacial water part.

analyses is that at least one atom of both the lipid and water part involve in all normal modes of the systems. It means that there is no exclusive mode for these two different components. In the frequency interval of $1000 < \omega < 1500$ cm^{-1}, the lipid part is much involved in the vibration than the water part (Figure 5.10).

5.5 Estimation of phase velocity

5.5.1 Method

To derive the phase velocity for a given frequency ω, it is necessary to determine the wavenumber k, since $V_{ph} = \omega/k$. The vibrational eigenvectors of the system were used to determine the wavenumber. Considering a wave with sine function displacement and a given frequency ω, the wave can be mapped to plus-minus signs with discrete lattice size Δ, as shown in Figure 5.11. Then, the wavelength will be obtained by:

$$\lambda = \Delta \times 2 \times \frac{\text{(total number of (+) and (−) signs)}}{\text{(number of zones with (+) and (−) signs)}}. \tag{5.10}$$

For example, for the configuration shown in Figure 5.11.a, 12 different sings are distributed in 3 distinct zones, so the wavelength of this wave is equal to $\lambda = \Delta \times 2 \times 12/3 = 8\Delta$.

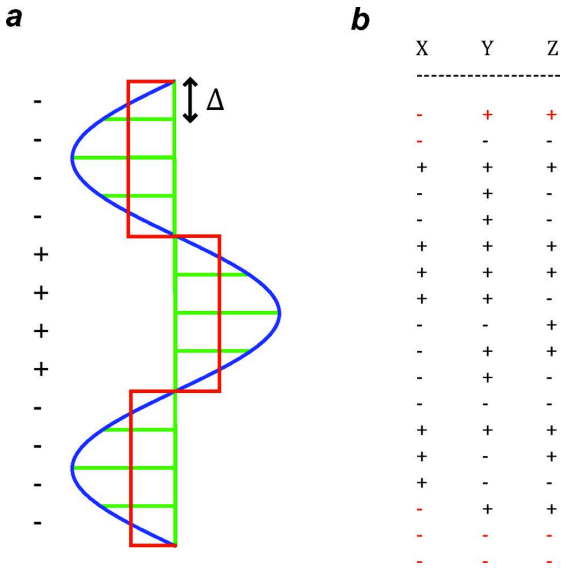

Figure 5.11: (a) Sine wave mapped to + and − signs with discrete lattice size Δ. (b) Plus-minus configurations belonging to x, y, and z polarizations of the mode at 202.9 cm^{-1} in fully hydrated DPPC.

5.5.2 Phase velocities of normal modes in DPPC complexes

An analogous analysis was done for the eigenmodes of the DPPC lipid. Propagation of the wave across the lipid displaces the atoms from their equilibrium position in 3 dimensions. Accordingly, for a given ω three wavelengths belonging to three directions are found and hence, three corresponding phase velocities can be determined. For instance, for a frequency equal to 202.9 cm^{-1} in a fully hydrated lipid, three wavelengths $\lambda_x = 6.76$ $\mathring{A}$, $\lambda_y = 6.87$ $\mathring{A}$ and $\lambda_z = 3.9$ $\mathring{A}$ were obtained. The corresponding phase velocities were 4115, 2967, and 2374 m/s with polarization in x, y, and z directions, respectively. The plus-minus configurations belonging to each polarization are given in Figure 5.11.b.

In the hydrocarbon chain of DPPC, the carbon atoms are considered as the affected points of the wave, therefore, lattice size Δ is defined as the average distance between adjacent carbons and is about 1.3 $\mathring{A}$. For the sake of simplicity, the propagation of the wave along the tail section of DPPC is taken into account, which results in having only one discrete lattice size Δ, in each direction. The other reason to take the tail part but not the head group into account was that, the energy propagation from head group to the end of tail group was the aim of these calculations. Generally, 18 carbon atoms of the lipid tail were considered for the calculation. For each polarization mode, the boundary signs in the plus-minus chain were not taken into account (red signs in Figure 5.11.b). This is due to the uncertainty in the displacement of the boundary atoms; beyond the calculated chain of signs it is not clear whether the sign will change

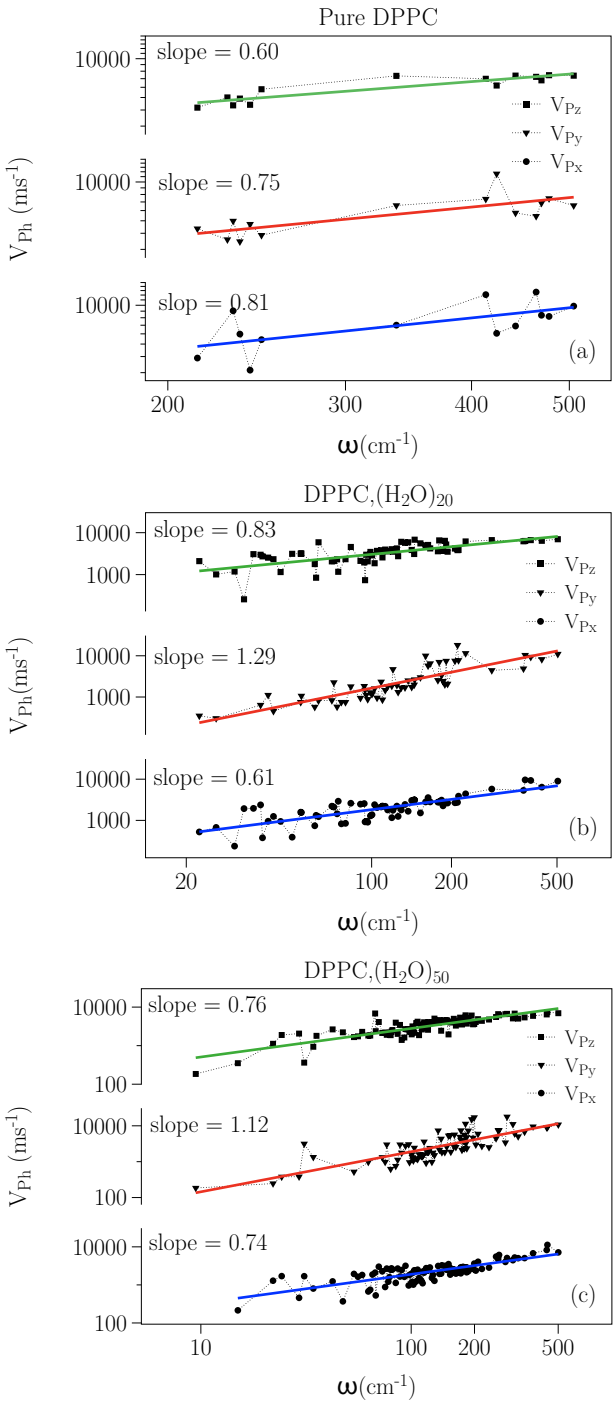

Figure 5.12: The phase velocities V_{ph} (ω) for (a) DPPC, (b) PH-DPPC, and (c) FH-DPPC (see Figure 5.1 for the coordinate axis).

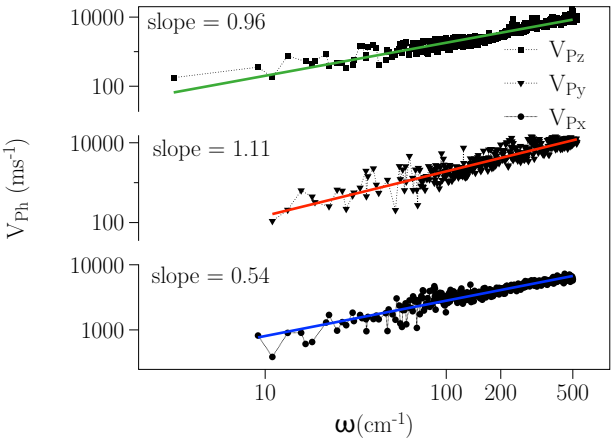

Figure 5.13: The phase velocity V_{ph} (ω) of a hydrated DPPC bilayer.

or continue with the sign of the boundary atoms. The ω dependence of phase velocities for DPPC,$(H_2O)_n$, in which n=0, 20, 50, are illustrated in Figure 5.12.

Experimentally, in order to calculate the time scale for energy transfer in hydrated DPPC, it is assumed that the O−H stretching mode of the interfacial water is excited by an incident laser pulse [**?**]. The vibrational relaxation of O−H is followed by a thermalization process, which occurs with a relaxation time smaller than 0.1 ps [**?**]. The high-frequency modes are predominantly local modes which cannot propagate the energy in the lipid. Only modes with frequencies bellow $\omega = 250$ cm^{-1} can carry the vibrational energy from head to tail. The typical velocity of the mode with the highest vibrational DOS in the interval $0 < \omega < 250$ cm^{-1} is about 3200 m/s. For $\omega = 250$ cm^{-1} the wave velocity is about 5500 m/s. The distance between the hydrogen atom of the choline methyl group and the hydrogen of the CH_3 at the tail is nearly 28 $\mathring{A}$. Hence, it can be determined that the time scale of energy transfer from the head to the end of the tail is around 0.5-0.9 ps. This time scale is in excellent agreement with the results of recent time-resolved sum frequency generation (tr-SFG) studies [**?**].

Similarly, Figure 5.13 illustrates the results of calculation of the phase velocity for hydrated bilayer-like DPPC. In this case, the energy transfer through the hydrophobic region, consisting of two series of hydrocarbon chains, was investigated. This study addresses the question that how the energy propagates from one chain to the other when their atoms are not explicitly bonded. The measurements showed that, in comparison to the system contains one DPPC, in the bilayer like structure, a few more number of frequencies are able to propagate in whole chain region. For frequencies in the interval $0 < \omega < 370$ cm^{-1} the estimated phase velocity was below 5500 m/s. As an example for frequency $\omega = 250$ cm^{-1}, the phase velocity is 4724.65 m/s. Given that the length of the total chain region is about 42.45 $\mathring{A}$, the time scale of energy transfer from the head part of one lipid to the other lipid is estimated to be 0.89 ps.

5.6 Conclusions

In summary, in the present work it was found that hydration has a significant effect on the vibrational dynamics of phosphatidylcholine, leading to the emergence of extended vibrational modes that involve multiple lipid molecules from opposing leaflets and their hydration shells. In real biological environments, a large number of lipid molecules of various kinds assemble to form a membrane. The cooperativity among the lipids is highly important for the formation and stability of the membrane. The results of this study show that even for the relatively small system of two hydrated DPPCs, cooperativity in the membrane is very important. It also affects the vibrational properties and associated conductivity of the system. It is hoped that the present study will stimulate further investigation of the vibrational dynamics and energy transfer of lipids by considering the effect of the additional neighboring lipid molecules and the lipid chemical heterogeneity known to occur in natural membranes.

6 Vibrational lifetimes of pure and hydrated DPPC

6.1 Introduction

Biological membranes are dynamic entities that are involved in processes that occur at various time and length scales. Motions in lipid bilayers range from the long wavelength undulation and bending modes of the bilayer, with typical relaxation times of nanoseconds and lateral length scales of several hundreds of lipid molecules, to the short wavelength density fluctuations in the picosecond range happening on the nearest neighbor distances of lipid molecules (see [?] and references therein). Local dynamics in lipid bilayers, consisting of dynamics of individual lipid molecules including vibrations, rotations, librations (hindered rotation), and diffusion, have been investigated by, for example incoherent neutron scattering and NMR to determine the short wavelength translational and rotational diffusion constant [?, ?].

The characteristic time scales are also relevant to the vibrational energy transfer across lipid membranes, which is a very important phenomenon in many biological processes that have been studied extensively [?, ?]. Thus, there have been several recent studies on the dynamics and characteristic time scales of lipid-like assemblies, lipid membranes and the associated molecules [?, ?, ?, ?, ?]. Experimentally, femtosecond time-resolved studies that probe energy dynamics in biomolecules provide important information about, and insight into, the functions of biomolecules, which cannot be obtained from static experiments alone [?, ?, ?, ?, ?]. Information about what takes place at the membrane's surface is crucial to understanding viral infection and targeted drug delivery.

Recent experiments [?] have indicated that the hydration of lipid headgroups by water enables efficient energy transfer across membrane leaflets on sub-picosecond time scales. This fact has also been demonstrated by the *ab initio* calculations whose results are presented in Chapter 5. In the present work, it is shown that the extended vibrational modes that emerge upon hydration underlie this phenomenon. The dynamics of membrane-associated proteins and their affinities to downstream components might be affected by coupling to the vibrational dynamics of the lipid bilayer membrane [?]. Advances in two-dimensional IR spectroscopy have made it possible to probe the vibrational coupling between lipids and the associated proteins [?]. Predicting the vibrational properties of lipid bilayer of biomembranes is, however, a nontrivial task due

to the system size and the interactions of lipid atoms with nonbonded solvent molecules. Moreover, cellular membranes function at relatively high temperatures which is characteristic of the physiological conditions in which they exist.

In a harmonic approximation, phonons do not scatter, therefore, they have infinite lifetimes. In the vibrational density of state, or the vibrational spectrum, they exhibit peaks that are of the delta-function type. However, at nonzero temperatures, the phonons scatter, thus, have finite lifetimes due to the anharmonic interactions. The scattering process leads to a shift in the phonon spectrum and the broadening of the phonon peaks. At low temperatures, the estimation of the vibrational lifetimes, based on harmonic and third-order anharmonic lattice dynamics calculation, is reasonably accurate for bulk crystals [**?**]. However, this is not the case for biological membranes, due to the fact that, at the relevant temperatures of biological systems, higher-order events are not negligible anymore.

Experimentally, there have been several femtosecond laser-based studies, that attempted to address the dynamics of model biological membranes, such as water-lipid interactions [**?**, **?**, **?**, **?**, **?**] and transmembrane proteins [**?**, **?**]. However, these recent experimental works have produced data only for the high-frequency regime (40−55 THz) and knowledge for the low-frequency region still remains to be explored.

Theoretically, various methods have already been developed for predicting the vibrational lifetimes, such as the perturbation method [**?**], the normal mode analysis [**?**, **?**, **?**], and the spectral energy density analysis [**?**, **?**, **?**]. The perturbation method is used in the frequency domain and uses Fermi's golden rule to calculate the three-phonon scattering rates that result from lattice anharmonicity. In this model, the temperature effect can be included only implicitly by tuning the phonon occupation number based on the phonon density of states at zero temperature. Typically, anharmonic lifetimes calculation is limited to three-phonon scattering events, which is a good assumption only at low temperatures.

The idea of the spectral energy density (SED) methods is based on applying atomic velocities resulted from molecular dynamics simulations to find the spectral energy density of the system [**?**, **?**]. By mapping the position of atoms onto individual phonon normal modes, the SED method is able to derive the spectral phonon relaxation time from either the phonon population decay in the time domain, or the phonon linewidth in the frequency domain. As atoms dynamically evolve according to the full anharmonicity of the interatomic interactions, all order phonon processes are taken into account in the MD simulation. Therefore, the lifetimes predicted by SED method include the effect of n-phonon scattering events. Aside from these reasons, the simplicity is the major merit of the SED analysis.

For this reason, the SED method was chosen to study the relaxation time of vibrational phonons in DPPC molecule and hydrated DPPC complex as an example of biological systems. In the following, this method is briefly introduced. Then, vibrational lifetimes which were calculated by applying the SED method for trajectories of dynamical evolution of the mentioned systems, acquired from *ab initio* molecular

dynamics (AIMD) simulation, will be reported.

6.2 Spectral energy density formalism

The SED method involves the effect of n-phonon scattering events by not expensive computational efforts. Therefore, it presents a robust and efficient approach for evaluating vibrational lifetimes. This technique was initially proposed by Thomas and his colleagues [**?**], in order to investigate the fully anharmonic phonon properties of carbon nanotubes in the presence and absence of water molecules. The method does not require special adjustable parameters and can be readily integrated with highly accurate and computationally expensive AIMD simulations in order to extract the fully anharmonic phonon frequencies and the associated phonon scattering rates for individual modes [**?**, **?**, **?**]. Moreover, since the SED is obtained directly from the projected atomic velocities correlation functions, there is no distinction between normal and umklapp phonon scattering processes. Both effects are fully included in the calculations of the phonon lifetime. The effect of umklapp processes is not negligible for the study of phonon properties of systems with nonbonded interactions, for instance those which occur between the lipid and water molecules.

A system consisting of either one lipid molecule or a complex of lipid and water molecules is described as a cluster, for which only the Γ point is involved in density functional calculations. Therefore, following the initial works established in [**?**, **?**], a specific case of the SED formalism is defined for Γ point calculations. In this formalism, computation of the spectral energy density is based on the projected velocity time series of all atoms onto the eigenvectors of the vibrational modes $\mathrm{q}_\varrho(\nu;\mathrm{t})$. The contribution of the displacement of the i^{th} atom in the normal mode is determined by:

$$\mathrm{q}_\varrho(\nu;\mathrm{t}) = \frac{1}{\sqrt{N}} \sum_{\varrho=1}^{3N} \sqrt{\mathrm{m}_i}\ \mathrm{e}_\varrho(\nu)\ \mathrm{u}_\varrho(\mathrm{t}). \tag{6.1}$$

The cumulative index $\varrho = (i, \alpha)$ refers to the atom i and the α component of its displacement vector, such that $\mathrm{u}_\varrho(\mathrm{t})$ indicates the α component of the displacement vector of the atom i with the mass m_i at time t. For a cluster consisting of N atoms in three dimension ϱ varies from 1 to $3N$. The polarization vector corresponds to the normal mode is represented by $\mathrm{e}_\varrho(\nu)$. The relaxation time scales τ of the vibrational modes are determined by evaluating the spectral energy density, $\Psi(\omega)$ as a function of the normal frequencies ω and the wavenumber ν [**?**, **?**]. The average kinetic energy of normal mode ν at Γ point is defined as:

$$\langle \mathcal{T}(\nu) \rangle = \sum_{\varrho=1}^{3N} \left[\frac{1}{2\tau_0} \int_{-\tau_0}^{\tau_0} \dot{\mathrm{q}}_\varrho^*(\nu;\mathrm{t}) \dot{\mathrm{q}}_\varrho(\nu;\mathrm{t}) \mathrm{dt} \right]. \tag{6.2}$$

By applying Parseval's theorem, the kinetic energy is transferred to the frequency space:

$$\langle \mathcal{T}(\nu) \rangle = \sum_{\varrho=1}^{3N} \frac{1}{4\tau_0} \left| \frac{1}{\sqrt{2\pi}} \int_{-\tau_0}^{\tau_0} \dot{\mathrm{q}}_\varrho(\nu; \mathrm{t}) \exp(-\mathrm{i}\omega \mathrm{t}) \mathrm{dt} \right|^2 , \tag{6.3}$$

in which ω refers to the angular frequency. According to the definition, the spectral energy density calculated at the Γ point is obtained by:

$$\begin{aligned} \Psi(\omega) &= 2\langle \mathcal{T}(\nu) \rangle \\ &= \frac{1}{4\pi\tau_0 N} \sum_{\varrho=1}^{3N} \mathrm{m}_i \left| \dot{\mathrm{u}}_\varrho(\mathrm{t}) \exp(-\mathrm{i}\omega \mathrm{t}) \mathrm{dt} \right|^2 . \end{aligned} \tag{6.4}$$

In each phonon mode, a number of vibrational frequencies are available for atoms, which depends on the level of anharmonicity of inter atomic potentials and the rate of the phonon scattering processes. The Lorentzian function $\mathcal{L}(\omega)$ describes the accessible ranges of frequencies for each mode with their centers at the fully anharmonic vibrational frequency ω_p. It was proved that the spectral energy density is a linear superposition of $3N$ Lorentzian function,

$$\Psi(\omega) = \sum_{\nu=1}^{3N} \mathcal{L}(\omega, \nu), \tag{6.5}$$

and the Lorentzian function is represented as:

$$\mathcal{L}(\omega, \nu) = \frac{I_\mathrm{p}}{[2\tau(\omega - \omega_\mathrm{p})]^2 + 1} , \tag{6.6}$$

in which, I_p stands for the combination of the coefficients as the weighting factors for the Lorentzian functions and determines the peak amplitude in the spectral energy density profile. The frequency at the peak's centre is denoted by ω_p, and τ measures the mode's lifetime.

Finally, in order to estimate the lifetime of each dominated frequency indicated by peaks, the spectral energy density profile $\Psi(\omega)$, is fitted by the Lorentzian function at the position of each peak. In the following, AIMD simulations, through which the velocity time series were captured, will be described in detail, and the obtained results for the mentioned systems will be presented as well.

6.3 *Ab initio* molecular dynamics simulation (AIMD)

To obtain the time series of atomic positions and consequently their velocities to employ in the SED formulae, the referenced systems were simulated by using the AIMD simulations. To achieve this aim, the minimum energy configuration of pure DPPC was firstly

determined. The relaxed configuration of the DPPC molecule was then used to construct the system of DPPC and water bulk. As the next step, the minimum structure of the lipid-water complex was generated. The headgroup of the lipid was hydrated by 50 water molecules. As was explained in Chapter4, the ground state calculations were performed by using density functional theory approaches implemented in the SIESTA code. The calculated ground state structures were used as the initial configurations for the *ab initio* molecular dynamics simulations at T=310 K, which is the temperature of the human body. The generalized gradient approximation with Perdew-Burke-Ernzerhof parametrization was chosen to approximate the electron exchange correlation potential. Troullier-Martins-type pseudopotentials along with double-ζ singly polarized basis sets are also considered as calculation parameters of first principle calculations. The coordinates of the atoms were relaxed using the conjugate gradient method until the maximum force exerted on the atoms fell below 0.005 eV/$\mathring{A}$. The simulated systems are considered as cluster, therefore only the Γ point in the reciprocal space was needed for energy integration.

Total simulation time for two systems was about 3 ps with a time step of Δt=0.1 fs, which is about one hundredth of the shortest vibration period in this system. The temperature was held constant with the Nosé-Hoover thermostat. Therefore, all vibrational modes and their lifetimes were determined at temperature T=310 K, which corresponds to the temperature at which they are most active. The results of these calculation are presented in the next section.

6.4 Calculation of spectral energy density of pure and hydrated DPPC

The spectral energy density profiles of both the pure and hydrated DPPC were estimated by performing the SED analysis [**?**] on the velocity time series, which were obtained through AIMD simulations. Figure 6.1.a presents the spectral energy density profile of pure DPPC. The active vibrational modes of pure DPPC at 310 K are under the frequency of 100 THz for which evaluated lifetimes are of about 1 ps.

Similarly, the active vibrational modes of hydrated DPPC at 310 K are depicted in Figure 6.2.a. The range of the active phonon modes and the related lifetimes for the complex of water and lipid do not show a huge discrepancy with those calculated for the pure DPPC. The active modes and their relaxation times are listed in Table 6.1. Figure 6.3 depicts three vibrational modes of DPPC with its head part hydrated with 50 water molecules at frequencies of about 2.84, 4.40 and 37.60 THz. These frequencies are spatially extended modes. Referring to this figure, it will be concluded that the highest active modes are not the prefered modes for the head part, such that under these extended vibrational modes the headgroup's atoms do not move.

The frequencies at which both the lipid and water molecules contribute to the spectral

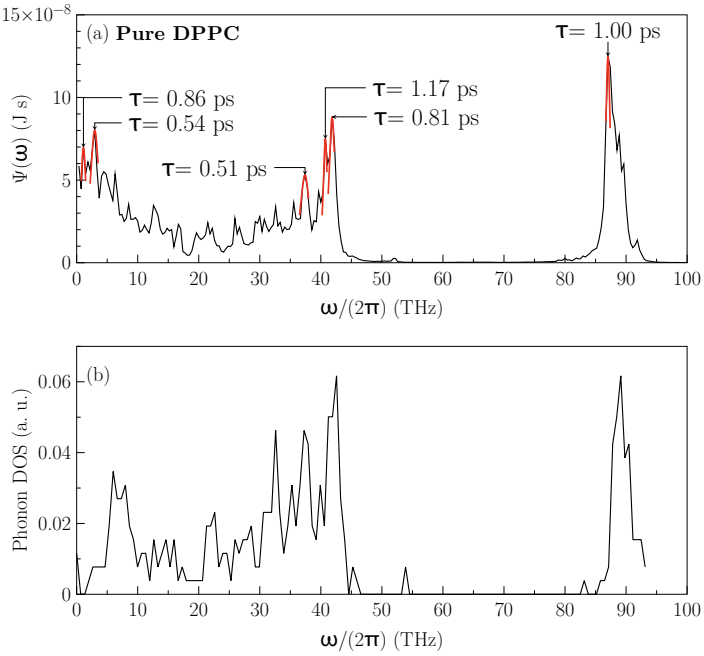

Figure 6.1: (a) Spectral energy density and vibrational lifetimes of pure DPPC. (b) The density of states of the phonon frequencies are obtained by harmonic lattice dynamics computations.

Pure DPPC		$DPPC,(H_2O)_{50}$	
Frequency (THz)	Lifetime (ps)	Frequency (THz)	Lifetime (ps)
1.11	0.86	2.80	0.75
2.96	0.54	4.40	0.86
37.40	0.51	37.60	0.69
40.74	1.17	42.00	1.41
41.85	0.81	87.60	0.52
87.03	1.00		

Table 6.1: The active vibrational modes of pure DPPC and the complex of $DPPC,(H_2O)_{50}$ at T=310 K and the estimated lifetimes.

energy density profile were examined. For this purpose, the spectral energy density of DPPC and water bulk were calculated separately and depicted in Figure 6.4. As shown in Figure 6.4.b, water molecules are active in a wide range of frequencies, from 0.5 THz to 55 THz, with some peaks around 2.80 THz and 48.75 THz. In the range of 45−55 THz, bulk water has the main contribution to the total spectral energy density. The lipids are active mainly at frequencies 4.40, 5.20, 37.60, 42.00, and 87.58 THz, as

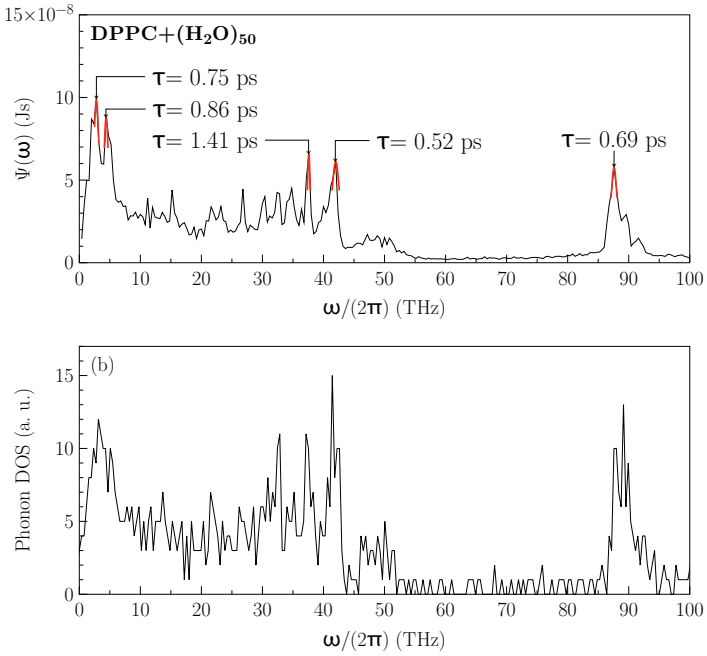

Figure 6.2: (a) Spectral energy density and vibrational lifetimes of the complex DPPC,$(H_2O)_{50}$. (b) The density of states of the phonon frequencies are obtained by harmonic lattice dynamics computations.

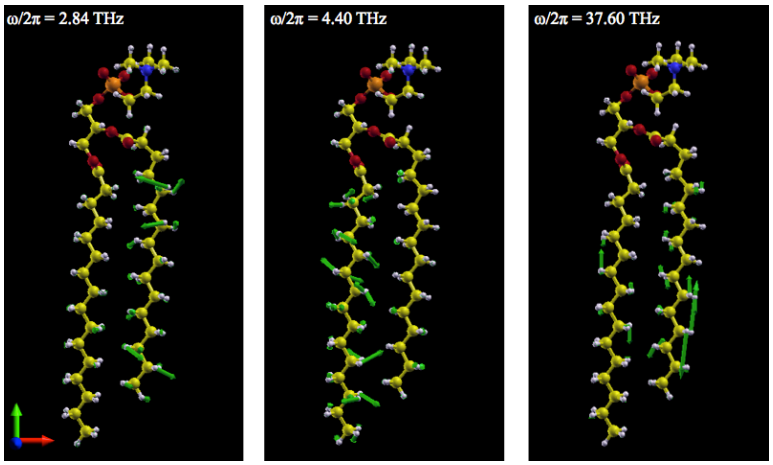

Figure 6.3: Examples of vibrational modes at frequencies of 2.84, 4.40 and 37.60, corresponding to the frequencies of peaks in the spectral energy density of the DPPC,$(H_2O)_{50}$ complex. As is shown, the lipid's head part is not engaged in the high active modes. The water molecules are not shown here for clear illustration of the head part.

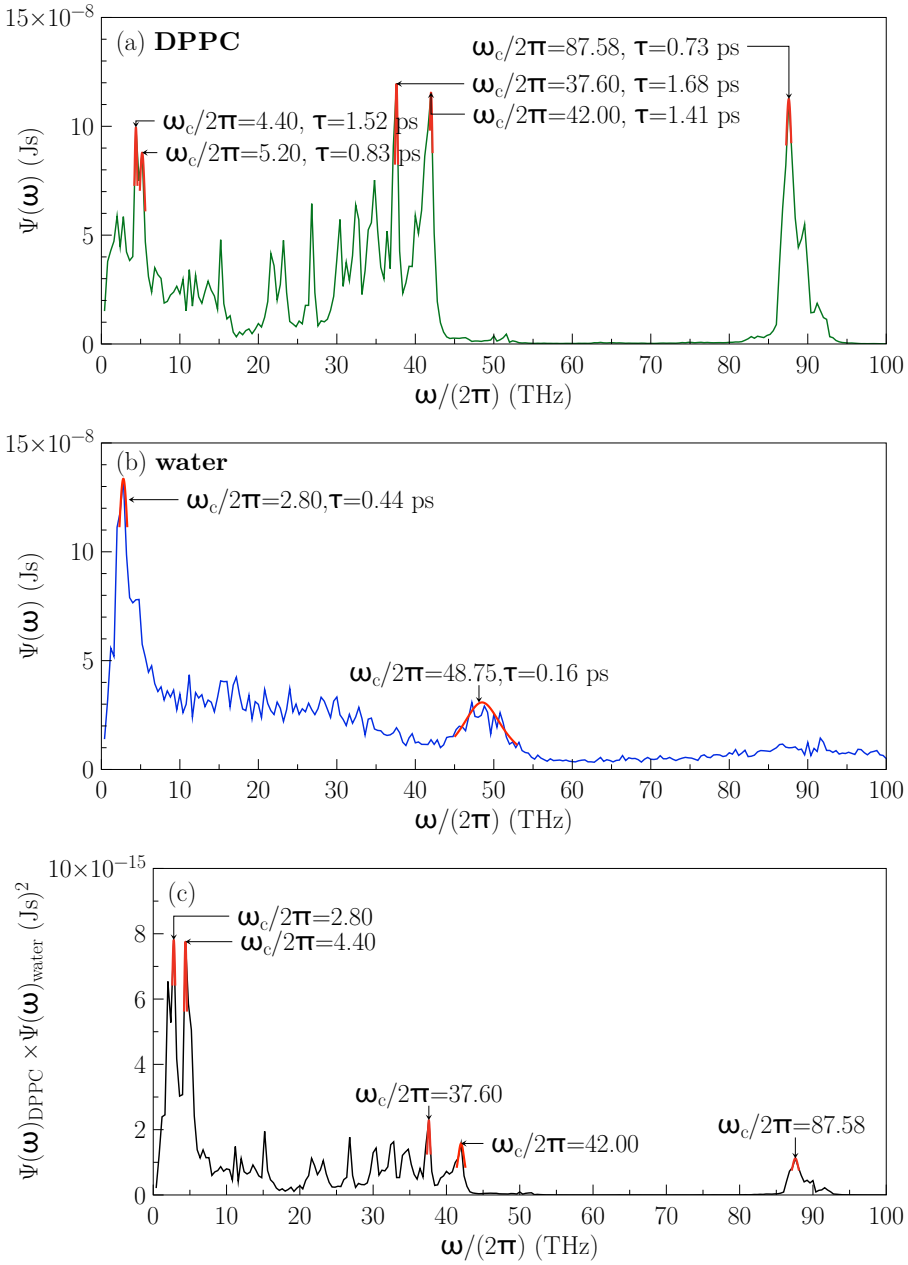

Figure 6.4: Decomposition of the spectral energy density of the complex of DPPC and water into the separate spectra of (a) DPPC and (b) bulk water. The corresponding vibrational lifetimes are also demonstrated. Plot (c) shows the product of the two spectral energy densities, illustrating the active ranges simultaneously for the bulk water and the lipid.

indicated in Figure 6.4.a. The multiplication of the two profiles for lipid and water molecules is illustrated in Figure 6.4.c, which presents the active modes of the lipid in the vicinity of water molecules.

6.4.1 Comparison of SED with harmonic approximation phonon DOS

In order to examine the effect of neglecting the interaction anharmonicities in estimating the vibrational modes, the profile of the density of states of the phonon frequencies obtained by harmonic lattice dynamics computations are illustrated in Figure 6.1.b and 6.2.b. By comparing the profiles of the density of states and spectral energy densities (Figure 6.1.a and 6.2.a) it can be established that the locations of the peaks in both profiles are reasonably in accordance with each other, indicating that the phonon frequency shifts due to anharmonic effects are negligible. Full vibrational modes of the DPPC and hydrated DPPC were estimated within the linear response regime in the same way as explained in Chapter 5. It can be concluded that integrating beyond 3 ps, which is approximately three times greater than the longest phonon lifetime, does not change the predicted phonon properties.

6.4.2 Comparison of SED analysis with experiment

A comparison of some of the results presented here with experimental findings is also instructive. As discussed earlier, a relaxation time of about 0.69 ps was found for the peak in the spectral energy density profile of hydrated DPPC with a frequency of 87.60 THz. This result is in agreement with the relaxation time measured using time-resolved sum frequency generation [**?**]. The experimental value for the lifetimes in the high frequency range of 83.94−89 THz were reported to be (sub-) picoseconds. It is worth noting that the estimated relaxation times, particularly for the low-frequency modes, are affected when neighboring lipid molecules are considered. In contrast to the high-frequency vibrational modes that are often localized, low-frequency modes extend over neighboring lipid molecules and the surrounding interfacial water. Physically, the local vibration of a few atoms including the H-bonds will be almost independent of the other lipids. However, for vibrations with long wavelengths, the mean free path of such modes will be on the order of the lipid length and, hence, there will be interactions with other lipids too.

6.5 Conclusions

Summarizing, the *ab initio* molecular dynamics simulation was employed to calculate the lifetimes of the vibrational modes of the DPPC and DPPC-water systems. So far, experimental data for only the high-frequency regime were achieved and no data exist

yet for the low-frequency region. The results obtained in the present work agree well with the recent experimental results for high frequencies. While, the computed lifetimes of the low-frequency modes still need to be tested in the future. The computational method can be used to further investigate the system and to gain insight into energy transfer in other biomolecular systems. In addition, the approach may be used to compute the same properties for other types of polymers, as a long-standing problem.

7 Enhanced auto-ionization of water at phospholipid interfaces

7.1 Introduction

Phospholipids are amphiphilic molecules that in an aqueous environment self-assemble into bilayers and form the major structural constituents of biomembranes. While the affinity of the lipid's head group to interfacial water has been widely addressed in the literature, the exact chemical nature of this coupling is not fully understood and its strength remains to be quantified. In particular, it is not clear how this coupling affects the structure and dynamics of the interfacial water layer and the proton transport. Enhanced proton conduction along phospholipid-water interfaces was first observed in the mid 1980s [**?**, **?**]. Recent studies, by means of scanning tunneling microscopy (STM), confirmed a significant lateral conductivity [**?**]. This conductivity is believed to be of functional importance because lateral proton diffusion along membrane surfaces represents the most efficient pathway for H^+ transport between protein pumps [**?**]. The molecular mechanism underlying the high lateral proton conductivity has not yet been fully understood [**?**, **?**, **?**, **?**, **?**].

This chapter is devoted to the report of the results of the *ab initio* Molecular Dynamics (AIMD) and the *ab initio* Monte Carlo (AIMC) simulations of interfacial water molecules, covering the head groups of DPPC and DPPE lipids. Particularly, the auto-ionization and the influencing factors in the enhancement of this phenomenon in the interfacial water, will be discussed. The effecting factors are strong local electric field induced by the lipid head group and the strength of hydrogen bonds between the atoms of the head group and the atoms of water. To study the former, the effect of the electric field induced by the dipole moment of the head group of zwitterionic DPPC was detected. To investigate the latter, the behavior of interfacial water molecules covering the head group of DPPC and DPPE was simulated, with the knowledge of that PE group does not show an electric field as strong as PCs.

In the following, firstly the AIMD and AIMC techniques will be explained. The auto-ionization of neat water and interfacial water will be briefly presented later. This chapter will be continued by dealing with the enhancing mechanisms of dissociation of water molecules at the interface of the referenced lipids.

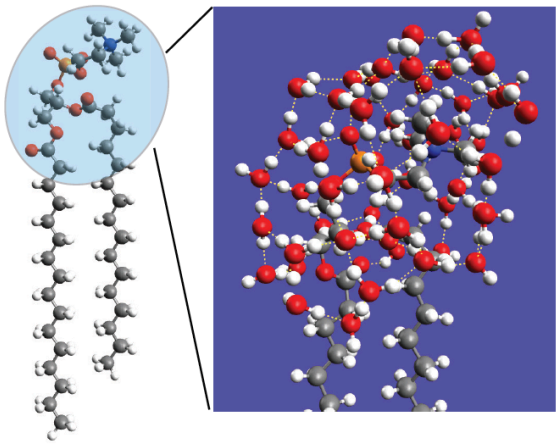

Figure 7.1: Ground state structure of DPPC,$(H_2O)_{50}$.

7.2 AIMD and AIMC simulations

In order to investigate the ionization phenomenon of interfacial water molecules, one DPPC molecule was exposed to a different number of water molecules to achieve various levels of hydration of the lipid's head group part. To this end the relaxed DPPC,$(H_2O)_{20}$, DPPC,$(H_2O)_{50}$ and DPPC,$(H_2O)_{75}$ complexes were used as the initial configurations for the *ab initio* molecular dynamics (AIMD) and the *ab initio* Monte Carlo (AIMC) simulations. The relaxed structure of these complexes was previously obtained within the DFT scheme and described in Chapter 4. Furthermore, to gain insight into the behavior of water molecules in the vicinity of a lipid monolayer, a complex of 2-DPPCs,$(H_2O)_{64}$ was also used. To construct this structure, two relaxed DPPCs are positioned parallel to each other with opposite dipole moment vectors. The relaxed configuration obtained from this arrangement resembles the structural unit of a membrane monolayer (for more details see Chapter 4).

The AIMD within local density approximation (LDA) were performed for the isolated DPPC,$(H_2O)_{50}$ complex (with no periodic continuation) in a time interval of 3 ps. To be able to track each small movement of all atoms, the time step needs to be precisely determined. Using the shortest vibration time as a basis, which is inversely related to the largest vibrational frequency of the system, one hundredth of this time, i.e. dt = 0.1 fs is considered as the time step in the MD algorithm. In these simulations the forces acting on atoms are determined based on the charge density which was obtained by using the DFT method as was explained in Chapter 3. This simulation was carried out in a canonical ensemble (NVT). The temperature was kept fixed at 300 K with the Nosé-Hoover thermostat [**?**, **?**].

Although this simulation was performed with a very efficient Order-N algorithm,

implemented in the SIESTA package, it was figured out that the AIMD is very time consuming method such that it took about 10 month CPU time on 12 parallel processors, (Intel(R) Xeon(R) CPU, X5650 @ 2.67 GHz) to draw the dynamics of this complex system for a period of only 3 ps. For this reason, in order to simulate the rest of mentioned complexes, the AIMC technique was applied, by which the real required time for thermalizing a system with large number of atoms is significantly decreased. In addition to computational costs, molecular dynamics methods have another disadvantage, which sometimes may lead to unreliable results. The problem is that in an AIMD simulation, the system might be trapped in a local energy minimum, leading to poor conformational sampling. In contrast, the random nature of AIMC technique would easily lead to barrier crossings. As a result, it is more likely to cover the whole phase space through the AIMC simulation. The standard Metropolis algorithm was used for performing the *ab initio* MC simulations. In this algorithm every MC step involves the following processes:

- For a given initial configuration, the total energy of the system $\mathrm{E_{init}}$ is obtained from an *ab initio* calculation. As previously mentioned, the total energy was obtained by using two different approximations, namely LDA and GGA for the exchange correlation term in the Kohn-Sham equation.

- Then, every atom i in the system is displaced according to a random displacement vector, such that $\mathbf{r}'_i = \mathbf{r}_i + \mathrm{d}\mathbf{r}_i$. The total energy of the system for this trial move is calculated $\mathrm{E_{trial}}$.

- If $\Delta\mathrm{E} = \mathrm{E_{trial}} - \mathrm{E_{init}} < 0$, the move is accepted, otherwise it is accepted only with the probability:

$$\mathrm{acc(init \rightarrow new)} = \min\{1, \exp[-\beta(\mathrm{E_{trial}} - \mathrm{E_{init}})]\} \tag{7.1}$$

- If the movement is accepted the trial energy is replaced for the new total energy of the system and the system acquires the new configuration. This new configuration is considered as the initial configuration for the next move. In the case that the trial movement is rejected, the atoms preserve their previous coordinates and the energy does not change.

Here, $\beta = 1/\mathrm{k_B T}$ and T and $\mathrm{k_B}$ are temperature and the Boltzmann constant, respectively. For the present work the temperature was fixed at 300 K, and the simulation was carried out for an NVT ensemble. The maximum displacement for hydrogen atoms $\mathrm{d}\mathbf{r}_\mathrm{H}$ was calculated in such a way that the acceptance ratio in every MC step remained within 30% of all trial movements. The maximum movement of the i^{th} atom is defined by the their mass ratio with respect to the hydrogen mass such that $\mathrm{d}\mathbf{r}_i = (\mathrm{m_H}/\mathrm{m}_i)\mathrm{d}\mathbf{r}_\mathrm{H}$.

7.3 Auto-ionization of neat water

The auto-ionization of water is one of the key self-reactions occurring in aqueous systems, resulting in dissociation of a water molecule, H_2O, to a hydroxide ion, OH^-, and a hydronium cation H_3O^+. Hence, the auto-ionization is a determining factor of pH of the pure water or aqueous solution. This reaction can be formulated as:

$$H_2O + H_2O \rightleftharpoons OH^- + H_3O^+$$

In bulk liquid water, auto-ionization is a very unlikely process with a probability of about 1.6×10^{-9} at 300 K, which results in the neutral value of pH = 7 [**?**]. Obviously, the rate of this reaction increases by an increase in the thermal energy. Another driving factor in dissociation of water molecules can be interpreted by the electric field fluctuations in the bulk [**?**]. The following section attempts to explore this property for water in the interface of lipids.

7.4 Auto-ionization of interfacial water

During the *ab initio* simulation of different systems of water and DPPC molecules, an enhanced ionization of water was observed at the DPPC-water interface, even in the ground state configuration. The ionization enhancement was observed by applying both the local density and the generalized gradient approximation.

In the ground state of the DPPC,$(H_2O)_{50}$ complex, two water molecules dissociated into H^+ and OH^-, with the OH^- ions located in the vicinity of the choline group $[-(CH_2)_2-N(CH_3)_3]^+$. Upon removal of the DPPC molecule, the water cluster rearranged and the H^+ and OH^- ions re-associated. By increasing the number of water molecules around the head group to 75, the number of H^+ ions did not increase, indicating that auto-ionization was catalyzed by the interface and specific to the interface. Reducing the number of water molecules to less than 20, also leads to disappearance of the auto-ionization. For a system consisting of two neighboring hydrated DPPC molecules, again two water molecules per lipid became auto-ionized in the ground state configuration.

Upon thermalizing systems to the finite temperature, a highly increase in the number of dissociated water molecules was observed. At finite temperature, the number of ionized water molecules was fluctuating in every AIMD and AIMC step. In Figure 7.2, the probability of finding N_{H^+} ionized water molecules in the DPPC,$(H_2O)_{50}$ complex is compared for the results obtained from the AIMC simulations with the local density and generalized gradient approximations.

For AIMC simulations, which were performed by using the LDA and GGA approximations, the average number of dissociated protons are $\langle N_{H^+}\rangle_{LDA} = 6.0 \pm 0.9$ and $\langle N_{H^+}\rangle_{GGA} = 4.7 \pm 0.8$, respectively. Here a further increase of auto-dissociation is observed compared to the ground state by a factor of about three. However, in the AIMD

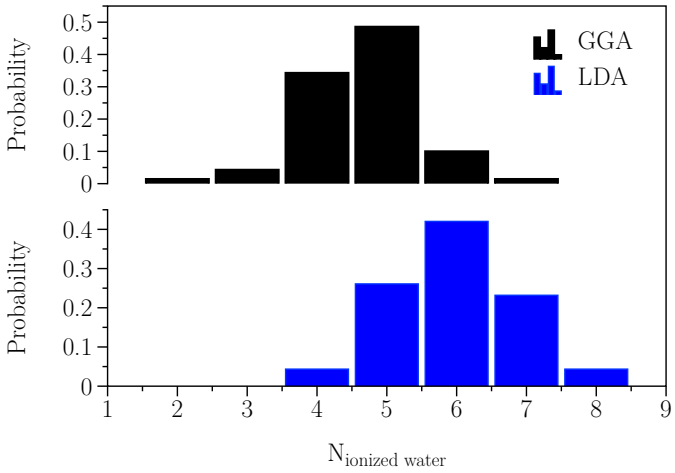

Figure 7.2: Probability of water ionization at 300 K, estimated by sampling configurations from the AIMC simulation for DPPC,$(H_2O)_{50}$ with LDA and GGA.

simulation performed by using LDA approximation, the average number of ionized water molecules was found to be $\langle N_{H^+} \rangle_{LDA} = 4.6 \pm 1.6$.

In order to find out an estimation of required distance between neighboring molecules in which the interaction between water molecules is likely followed by an dissociation process, the average distance of neighboring water molecules $\langle r_{O-O} \rangle$ was also determined. The distribution of O−O distances of the neighboring water molecules in the AIMC simulation with LDA and GGA are shown in Figure 7.3. The estimations show an average distance of about 2.50 $\mathring{A}$ and 2.55 $\mathring{A}$ for LDA and GGA approximations, respectively [**?**, **?**, **?**]. The probability densities of distances of neighboring water molecules $r_{O\text{-}O}$, involved in proton transfer processes were also determined and shown with black bars in the same figure. It was found that water molecules prone to auto-dissociation in the subsequent AIMC simulations within LDA and GGA, are found to present 2.37 $\mathring{A} \lesssim r_{O-O} \lesssim 2.6$ $\mathring{A}$ and 2.40 $\mathring{A} \lesssim r_{O-O} \lesssim 2.52$ $\mathring{A}$, respectively.

The origin of the observed enhanced auto-ionization can be sought in the presence of a strong local electric field caused by the lipid [**?**, **?**]. In addition, the effect of strong hydrogen bonding between the atoms of water and lipid molecules can be examined as the other possible effect in increasing the ionization of water molecules. In the following, by presenting the results of the *ab initio* simulations, the mechanism underlying the water dissociation will be investigated.

7.4.1 Electric field induced auto-ionization

Electric field-induced enhancement of water dissociation has been experimentally observed using field emitter tips for which the surface electric fields are estimated to be of

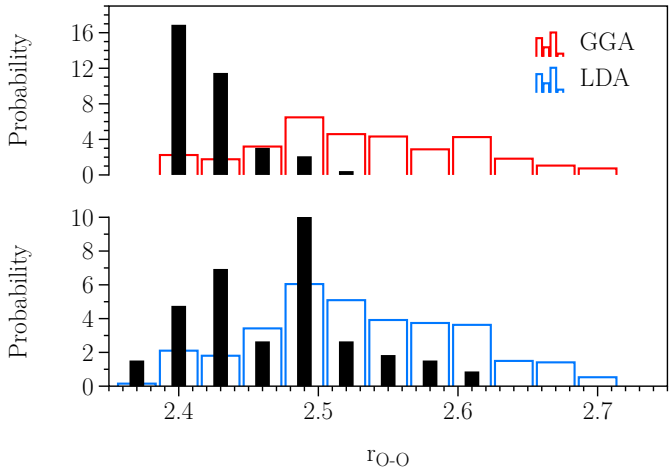

Figure 7.3: Probability density of oxygens distance of neighboring water molecules $r_{O\text{-}O}$ calculated through the AIMC simulation for DPPC,$(H_2O)_{50}$ with LDA and GGA at T=300 K. The probability densities of distances of neighboring water molecules $r_{O\text{-}O}$, involved in proton transfer processes are shown with black bars.

the order of 1 V/$\mathring{A}$ [**?**]. Moreover, as was demonstrated in Chapter 4, the interfacial water is subjected to the strong electric field of the lipid. As a result, the presence of this electric field was investigated as a possible driving factor of the ionization enhancement of interfacial water molecules.

In Chapter 4, it was explained that the lipid electric field originates primarily from the large dipole moment associated with the negatively charged phosphate and the positively charged choline groups of the DPPC molecule. The dipole moment of the DPPC head group is about 10 D, which is found to be about five times larger than the dipole moment of a water molecule. An electric field of this order of magnitude is able to distort molecules which results in ionization and bonds breaking. Thus a constant dissociation of interfacial water is expected. Figure 7.4 shows the probability density function of the magnitude of the electric field around the interfacial water molecules of hydrated DPPC. As is apparent in the Figure 7.5, there are many points in the space around the water molecules where the local electric field strength exceeds 1 V/$\mathring{A}$. In Figure 7.5 the potential iso-surfaces of $\pm$500 mV around the hydrated DPPC are depicted. This figure shows strong fluctuations of electric potential of about $\Delta V \simeq$1 V on a length scale of about 1 $\mathring{A}$.

As it is illustrated in Figure 7.3, the water molecules that get involved in proton transfer processes have O$-$O distances of about 2.37 $\mathring{A} \lesssim r_{O-O} \lesssim$ 2.70 $\mathring{A}$ and 2.40 $\mathring{A} \lesssim r_{O-O} \lesssim$ 2.70 $\mathring{A}$, for AIMC simulations within LDA and GGA, respectively. In bulk liquid water, where water auto-ionization is a rare event, the average distance $\langle r_{O-O} \rangle$ has been calculated and measured to be larger than the values observed at the lipid

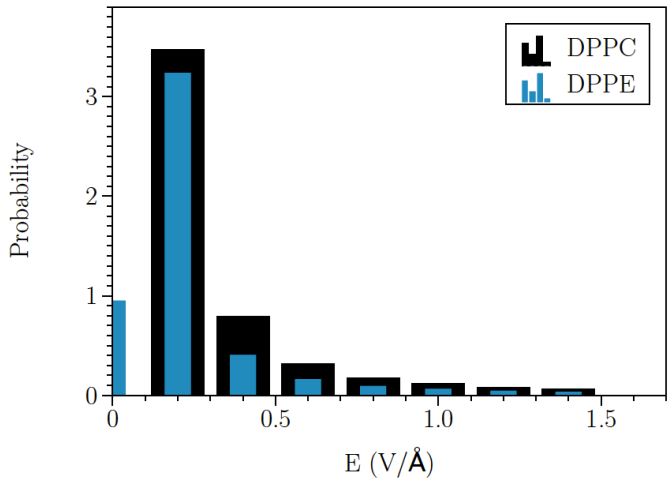

Figure 7.4: Probability distribution of the magnitude of the electric fields experienced by water molecules hydrating DPPC and DPPE. The threshold value to ionize water molecules is estimated to be about 1 V/$\mathring{A}$ [**?**]. The electric field distribution was calculated from a spherical region with a radius equals 1 $\mathring{A}$ at 3 $\mathring{A}$ distance (Lennard-Jones radius of O−atom in water molecule) from the water layer along the long axis of the molecule.

interface. However, experimental studies have reported various ranges for the $r_{O\text{-}O}$ distance which vary depending on the measuring technique used. For instance some neutron and X-ray diffraction studies determine a range of 2.78 $\mathring{A}$ − 2.82 $\mathring{A}$; while the corresponding distance was in the interval 2.5 $\mathring{A}$ − 3.5 $\mathring{A}$ when derived from EXAFS [**?**, **?**, **?**, **?**]. With a decrease in O−O distance, the hopping matrix element of H-transfer increases, facilitating proton hopping. Similarly, association of H^+ and OH^- ions in water also proceeds via hydrogen bond contraction and involves a collective compression of the water-water bridging the ions [**?**].

To demonstrate that the observation of auto-ionization is not an artifact of the approach, the structure of water molecules hydrating the zwitterionic PE were analyzed. No auto-ionization is observed in the ground state configuration derived from GGA. This result can be understood with a closer inspection of Figure 7.4: the number of water molecules around DPPE that experience a local electric field exceeding 1 V/$\mathring{A}$, is lower than for the hydrated DPPC. In addition, the probability densities of $r_{O\text{-}O}$ distances of neighboring water molecules for DPPC,$(H_2O)_{50}$ and DPPE,$(H_2O)_{50}$ complexes in ground state configuration given in Figure 7.6, are consistent with this result. The distances $r_{O\text{-}O}$ observed for DPPE,$(H_2O)_{50}$ are rarely less than 2.5 $\mathring{A}$ and the auto-ionization within this cluster is thus unlikely. This behavior can in part be traced back to the electric dipole moment of DPPE being about 8.5 D, which is about 15% smaller than that of the DPPC molecule. An observed reduction about 12.5% in the spread

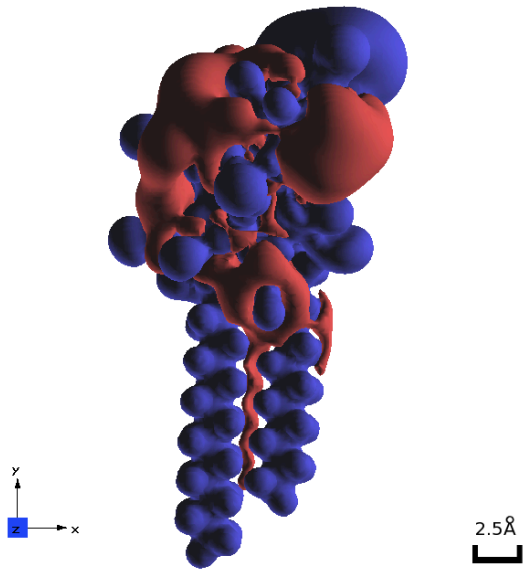

Figure 7.5: Potential iso-surfaces of DPPC,$(H_2O)_{50}$ for $V = 500$ mV (red) and $V = -500$ mV (blue) in the ground state. Strong spatial variations of the potential of about $\Delta V \simeq \pm 1$ V on a length scale of about 1 $\mathring{A}$ are clearly observable.

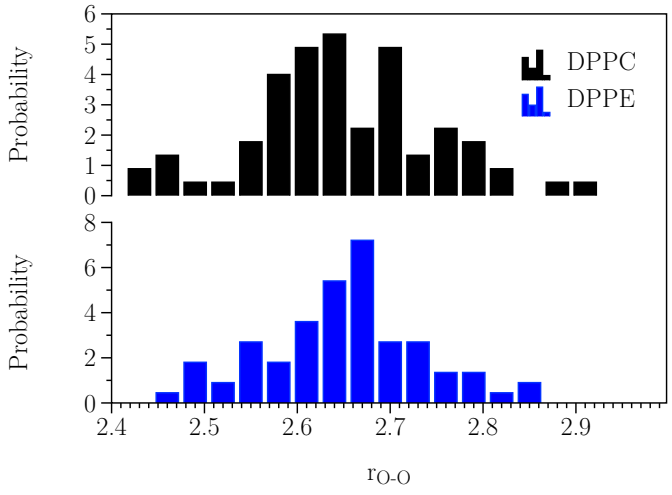

Figure 7.6: Probability distribution of distances $r_{O\text{-}O}$ of the neighboring water molecules for DPPC,$(H_2O)_{50}$ and DPPE,$(H_2O)_{50}$ with GGA in their ground state configuration. For DPPE,$(H_2O)_{50}$ $r_{O\text{-}O}$ always exceeds 2.5 $\mathring{A}$, consistent with the absence of auto-ionized water molecules. In contrast, for DPPC,$(H_2O)_{50}$, two auto-ionized water molecules are found in the ground state configuration.

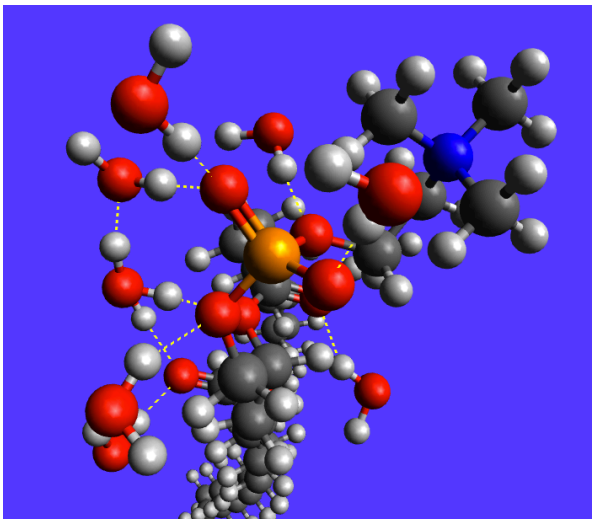

Figure 7.7: Hydrogen bonds formed in [HO−H ··· O=P], [HO−H ··· O=C], [HO−H ··· C−O−P] and [HO−H ··· C−O−C]. The color coding of the figure is as follows: carbon(gray), oxygen(red), hydrogen(white), phosphor(orange) and nitrogen(Blue).

of the $\langle r_{O-O} \rangle$ at the DPPE interface, indicates a stronger homogeneity of the electric field in the interface of this molecule.

7.4.2 Lipid-water coupling

As another possible factor which might affect the ionization process in water molecules in vicinity of the lipid head parts, the hydrogen bonds between lipid and water molecules was examined. It was explored that the enhanced water ionization cannot be explained by an increase in the strength of the hydrogen-bond interaction. Both DPPC and DPPE interact strongly with the interfacial water molecules, with DPPE making even more H-bonds with the water layer than DPPC. The hydrogen-bond interaction does however play a role in keeping the water molecules in close proximity to the lipid head group and thereby exposing them to the strong electric field exerted by the lipid. In this section, the typical strength of the hydrogen bonds formed between water and lipid molecules is quantified.

The effective spring constants are calculated from a potential of mean force (PMF), as introduced by Kirkwood in 1935 [**?**]. The hydrogen bond strength between H_{water} and O_{lipid} is considered a criterion to determine the coupling between these molecules. If r is considered as the distance between these atoms, the probability of finding a distance in the interval of $[r, r + \Delta r]$ is given by $p(r)\Delta r$. The constant term of the potential U(r) of mean bond stretching force can be estimated by the probability density of r:

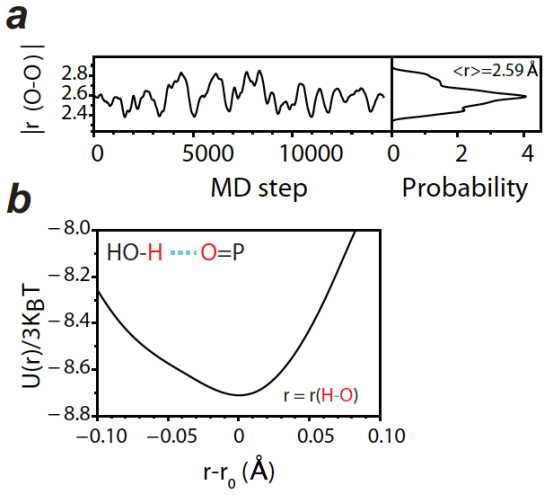

Figure 7.8: (a) Time fluctuations of $r_{O\text{-}O}$ for [HO−H $\cdots$ O=P] and their probability density. (b) The potential of mean bond stretching force U(r) for [O_{water}−$H_{water}\cdots$O=P] coupling. The effective spring constant k_{eff} is 74.1 N/m.

$$U(r) \propto -\log(p(r)\Delta r), \tag{7.2}$$

in which the discretization length Δr must be chosen much smaller than the scale over which U(r) changes. The probability density p(r) has a maximum around the equilibrium distance between two atoms, r_0, so it is possible to approximate the probability density by a Gaussian distribution around r_0,

$$p(r) \simeq \exp(-(r - r_0)^2/2\sigma^2), \tag{7.3}$$

hence, the potential of mean stretching force is estimated by:

$$\begin{aligned} U(r) &\propto -\log(p(r)\Delta r) \\ &\sim (r - r_0)^2/2\sigma^2, \end{aligned} \tag{7.4}$$

As a result of the equipartition theory, the spring constant k_{eff} is defined by requiring $1/2k_{eff}\sigma^2 = 3/2k_BT$. Consequently, this relation implies that:

$$k_{eff} = 3k_BT/\sigma^2. \tag{7.5}$$

In Figure 7.8.b the spring potential U(r) of a typical coupling for H_{water} coupled to the O=P compound in the lipid molecule is shown. Calculations for other hydrogen bonds formed between a water molecule and one of the PO^-, C−O−P, C=O and C−O−C compounds are depicted in Figure 7.9. These hydrogen bonds are illustrated in

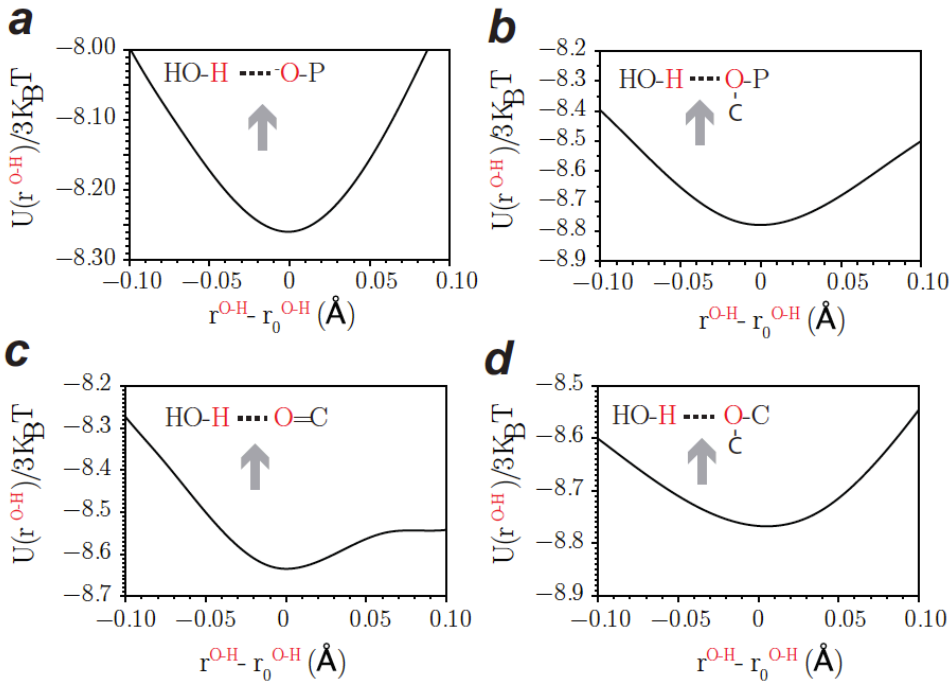

Figure 7.9: Potential U(r) of mean bond stretching force for water hydrogens bonding to (a) P−O$^-$, (b) C−O−P, (c) C=O and (d) C−O−C. The curvatures at the minima yield the spring constants listed in Table 7.1.

Coupling	$\langle r_{O\text{-}O}\rangle(\mathring{A})$	$\delta r_{O\text{-}O}(\mathring{A})$	k_{eff}(N/m)
HO-H···O=P	2.59	$\simeq 1$	74.1
HO-H···O=C	2.60	$\simeq 2$	24.6
HO-H···-O-P	2.80	$\simeq 1$	20.7
HO-H···C-O-P	2.87	$\simeq 1$	18.2
HO-H···C-O-C	3.04	> 2	9.3

Table 7.1: Mean and standard deviation of ($O_{lipid}\cdots O_{water}$) distances $r_{O\text{-}O}$ and effective spring constants k_{eff} of the corresponding ($H_{water}\cdots O_{lipid}$ bonds.)

Figure 7.7. The curvatures at the minima yield the spring constants listed in Table 7.1. These measurements were obtained with the data produced from an AIMD simulation for a DPPC,$(H_2O)_{50}$ complex after the time 3 ps.

To quantify the confinement of the water molecules at the interface of the DPPC molecule, the standard deviation of fluctuations of $r_{(O_{lipid}\cdots O_{water})}$ is determined. As an example, Figure 7.8.a shows the time fluctuations of $r_{O\text{-}O}$, where O_{lipid} is one of the oxygens of the phosphate group leading to the construction of a [HO−H ··· O=P]

structure. The probability density of the fluctuating $r_{O\text{-}O}$ values is also given in the same figure. The resulted mean value $\langle r_{O\text{-}O} \rangle$ and standard deviation $\delta r_{O\text{-}O}$ for this case, in addition to four more examples of lipid-water coupling, are given in Table 7.1.

In order to gain insight into the strength of the water-lipid coupling, the effective spring constants k_{eff} of $(H_{water} \cdots O_{lipid})$ bonds is determined according to the above explanation. Figure 7.8.b shows the associated potential of mean bond stretching force. By expanding the U(r) around their minima r_0, up to second order, the effective spring constant is found to be $k_{eff} \simeq 74$ N/m for the $(H_{water} \cdots O_{lipid})$ hydrogen bond formed in $[HO{-}H \cdots O{=}P]$. The effective spring constant for the $(H_{water} \cdots O_{lipid})$ hydrogen bond shows 60% more strength than the corresponding value for $(H_{water} \cdots O_{water})$ hydrogen bonds which is found to be $k_{eff} \simeq 47$ N/m. Evidently, interfacial water is strongly coupled to the lipid. This observation is in good agreement with recent results from pump-sum-frequency-generation (pump SFG) probe experiments at various frequencies underneath several lipid monolayers [**?**]. A variety of lipid monolayers all show a strongly hydrogen bonded subpopulation of water molecules that relaxes notably more quickly than water in bulk.

7.5 Conclusions

In summary, in the present study it was observed that water molecules display strongly enhanced auto-ionization at the lipid interface, as a result of the strong local electric field and the resulting reduced O−O distances of the water molecules located around the PC head group. The observation of enhanced auto-dissociation is expected to be relevant to the properties of water at a membrane interface. The strongly enhanced auto-dissociation reported here results in a significant local charge flux within the interfacial water layers and may explain the very high lateral conductivity associated with proton mobility observed for PC membranes. The enhanced ionization of water and concomitant charge mobility at PC lipids is highly relevant to biology, because PCs are the most common lipids in the outer leaflet of cell membranes. This study is a step towards understanding water ionization processes at the lipid interface using first principle methods. Further analysis is needed to quantify how the ionized water molecules specifically contribute to electrical conductivity of the system.

Part II

Coarse grained simulation of lipid bilayers

8 Coarse grained modeling of lipid bilayers

8.1 Introduction

In the first part of this thesis, one of the most recent and powerful methods, which has ever been stablished for performing first principle calculations of biomaterials was briefly introduced. In addition, by using *ab initio* methods, the chemical structure of two distinguishable specimens of lipids, DPPC and DPPE, was studied. Comparing the results obtained by these computational calculations with experimental results has confirmed the power and accuracy of the model.

Despite booming progress in both designing high performance computational tools and developing accurate and efficient computational algorithms in the field of chemical physics, elucidating the majority of biological phenomena, which require a broad range of temporal and spacial scales, remained out of reach for first principle methods. The time scale of a few picosecond, which is in the order of bond vibrations, and spatial scales in the order of atomic bounds, are now accessible by these methods. However, performing *ab initio* calculations provides researchers with a wealth of data sources for various types of chemical components to complete and improve classical force fields. As a result, in parallel to efforts to develop high performance computational methods in the last decade, researchers interested in material science tried to improve classical models as well. Classical methods are also extended over a broad range in accuracy and computational efficiency, however, the aim of all these methods is to pave the way for scientists to investigate large molecular systems, engaging in complex and time consuming phenomena.

Being aware of various methods for simulation of lipid membranes, one of the generic coarse grained models was chosen as a proper simulation method for the aim of the rest of this thesis. This generic coarse grained model was initially introduced by Düchs and Schmid [**?**], in order to study phase behavior of lipid monolayers.

In the present chapter, the coarse grained model, which was applied for the simulation of lipid membranes will be explained. In addition, the phase behavior of the model was investigated by reproducing some of the particular phases of lipid bilayer, according to the phase diagram of the referenced model. Later, in Chapter 9 and 10, the application of the model to investigate bilayers' mechanical properties and dynamical phenomena will be depicted.

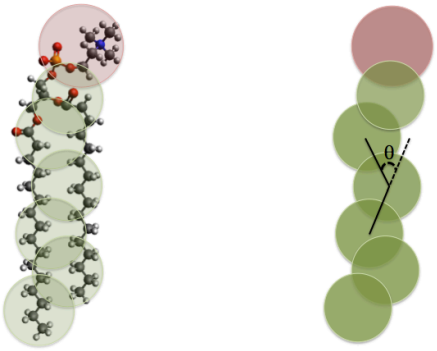

Figure 8.1: Lipid sketch of Düchs and Schmid model [**?**].

8.2 Lipid model

According to the coarse grained model initially introduced by Düchs and Schmid [**?**], each lipid consists of seven beads. One bead represents the hydrophilic head part and the remainder six beads show the hydrophobic chains (Figure 8.1). The interaction radius of tail beads is $\sigma_t = 1\sigma$ in the reduced unit of Lennard-Jones. The head bead is considered slightly larger than the tail beads with an interaction radius of $\sigma_h = 1.1\sigma_t$. Lipid molecules are surrounded by an aqueous environment, which is modeled by an explicit model for solvent particles. This model, which was proposed by Lenz and Schmid [**?**] will be precisely explained in Section 8.3.

For a system of lipid and solvent particles, the total energy of each particle is given by the sum of the intra- and intermolecular interactions. These interactions will be presented in the following.

8.2.1 Intermolecular interactions

In the reference model, the interaction of non-bonded beads is defined by a Lennard-Jones potential:

$$\mathrm{U_{LJ}(r)} = \epsilon[(\frac{\sigma_{\mathrm{LJ}}}{\mathrm{r}})^{12} - 2(\frac{\sigma_{\mathrm{LJ}}}{\mathrm{r}})^{6}] \tag{8.1}$$

For a short-range potential, whose energy function decays faster that r^{-3}, the main contribution in the total energy of a particle is governed by the neighboring particles located in a small given distance from that particle. This distance is considered as the cut off radius for that particular potential. For the sake of increasing the efficiency of computational methods, interactions with those particles which are beyond the cut off radius will be ignored in the calculations. In this case, the potential function is truncated at the cut off point. Obviously, the truncation procedure threatens the

accuracy of the energy estimation. In addition, it causes a discontinuity in the potential function, leading to a divergence of the potential derivative [?, ?]. However, in the Monte Carlo methods, truncation does not affect the algorithm. This is a serious problem in Molecular Dynamics simulation methods, when the equation of motion needs to be solved for moving particles. To avoid discontinuities occurring due to the truncation, and also to partly compensate the error of the total energy estimation, a constant term is added to the potential. This small term equals the value of the potential function at the cut off radius. This means that, the potential function is shifted in such a way that it obtains a null value at the cut off point and obviously also thereafter. Consequently, the potential function and its derivative are finite everywhere and the total energy will be conserved at the boundary. The shifted Lennard-Jones potential is expressed as:

$$U_{LJ}^{shifted}(r) = [U_{LJ}(r) - U_{LJ}(r_{cutoff})]\Theta(r_{cutoff} - r) \tag{8.2}$$

Θ represents the Heaviside step function, whose value is one for distances r smaller than r_{cutoff} and zero beyond that. By considering a sufficiently large r_{cutoff}, the error of the truncation can be made smaller. However, the discontinuity of the force between particles is yet to be solved, but it does not cause any problem in the MC algorithm.

In this model, the minimum radius σ_{LJ} of every type of Lennard-Jones interaction between different particles, is a pairwise additive of the sizes of two contributing beads. By choosing the cutoff radii equal to the minimum radius $r_{cutoff} = \sigma_{LJ}$, all interaction types but the tail-tail one are purely repulsive. For the tail-tail interaction, by considering a cut off radius as twice the interaction radius $r_{cutoff} = 2\sigma_{LJ}$, the attractive tail of the Lennard-Jones potential is also included. The attraction between the tail particles allows lipids to assemble in a bilayer structure. Hence, the self-assembling property of the model will be guaranteed.

8.2.2 Intramolecular interactions

In addition to the intermolecular potential, which rules the behavior of the non-bonded particles, there are other types of potentials, which control the interaction between beads belonging to a lipid. The intramolecular interactions are responsible for keeping lipid particles close together to maintain the lipid configuration. Inside a lipid, beads are connected by a semi-harmonic potential, defined by the attractive, finitely extensible, nonlinear elastic potential (FENE) [?, ?]:

$$U_{FENE}(r) = \begin{cases} -\frac{\kappa_{FENE}}{2} R_{max}^2 \ln[1 - (\frac{r - r_0}{R_{max}})^2] & \text{for} \quad r - r_0 < R_{max} \\ \infty & \text{for} \quad r - r_0 \geq R_{max} \end{cases} \tag{8.3}$$

where κ_{FENE} stands for spring constant, R_{max} is a finite extensibility of the spring and r_0 is the equilibrium distance between the particle centers. According to this

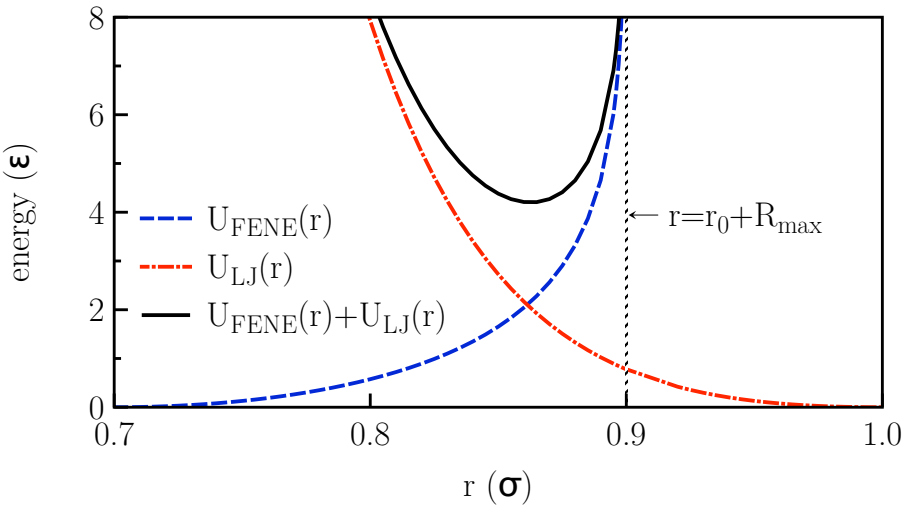

Figure 8.2: Interactions applied in the model.

model, parameters of the FENE potential are set to $\kappa_{\text{FENE}} = 100\epsilon/\sigma^2$, $R_{\text{max}} = 0.2\sigma$ and $r_0 = 0.7\sigma$, in the reduced Lennard-Jones units. It should be mentioned that, the maximum extensibility radius, as defined in this model, has been chosen so as to be short enough to prevent lipids crossing each other. The bond strength κ_{FENE} was also chosen to be weak enough to permit a simulation with long steps, leading to an increase in the efficiency of the program.

In addition to this connecting potential, the non-bonded beads of a lipid interact via a repulsive Lennard-Jones potential. As was the case for intermolecular interactions, all types of Lennard-Jones potentials consist only of a repulsive core with the exception of the tail-tail interactions.

The two mentioned potential terms, in combination with the bond angle potential, perform a set of interactions, which allow enough flexibility for bonds while at the same time preserving the lipid structure. Bond angle potential, which is considered in order to achieve a full conformational flexibility for lipid chains is expressed by:

$$U_{\text{BA}}(\theta) = \epsilon_{\text{BA}}(1 - \cos(\theta)) \tag{8.4}$$

As is depicted in Figure 8.1, θ is the angle between three adjacent beads. The magnitude of the bond angle strength was chosen as $\epsilon_{\text{BA}} = 4.7\epsilon$. All represented parameters of the model are summarized in Table 8.1

Interaction type	Potentials and Parameters
tail-tail	$U_{\mathrm{LJ}}(\mathrm{r})$: $\epsilon = 1$, $\sigma_{\mathrm{LJ}} = 1$, $\mathrm{r}_{\mathrm{cutoff}} = 2\sigma_{\mathrm{LJ}}$
head-tail solvent-tail	$U_{\mathrm{LJ}}(\mathrm{r})$: $\epsilon = 1$, $\sigma_{\mathrm{LJ}} = 1.05$, $\mathrm{r}_{\mathrm{cutoff}} = 1.05\sigma_{\mathrm{LJ}}$
head-head solvent-head	$U_{\mathrm{LJ}}(\mathrm{r})$: $\epsilon = 1$, $\sigma_{\mathrm{LJ}} = 1.1$, $\mathrm{r}_{\mathrm{cutoff}} = 1.1\sigma_{\mathrm{LJ}}$
solvent-solvent	none
bond length	$U_{\mathrm{FENE}}(\mathrm{r})$: $\kappa_{\mathrm{FENE}} = 100$, $\mathrm{r}_0 = 0.7$, $\mathrm{R}_{max} = 0.2$
bond angle	$U_{\mathrm{BA}}(\theta)$: $\epsilon_{\mathrm{BA}} = 4.7$

Table 8.1: Interaction potentials of the referenced model and corresponding parameters. r is the distance of the connecting vector of two particles, and as illustrated in Figure 8.1, θ is the angle between every three adjacent beads.

8.3 Solvent model

In addition to the inter- and intramolecular interactions between lipid particles, a solvent environment and the resulting interactions with lipid molecules are important parts of any kind of lipid membrane simulation. The solvent environment has a central role in developing a stable bilayer, especially in the fluid phase. The effect of the watery environment can be expressed by the hydrophobic nature of lipid particles. The repulsive interaction with solvent particles, obliges lipid beads to stay together and form a stable fluid matrix of lipids. In the present coarse grained model, aqueous environment is modeled by explicit solvent beads, so called phantom solvents. In this model, solvent beads are given the same size as the head particles, which equals $\sigma_s = 1.1\sigma$ in the reduced Lennard-Jones units. Solvent particles interact only with lipid particles via a pure repulsive Lennard-Jones potential, as was discussed in the subsection 8.2.1.

The biggest superiority of explicit models over surface potential models is that by using these models, full flexibility for the bilayers will be achieved. However, because in the phantom model solvent particles do not interact whit each other, this model has numerous advantages compared to earlier models such as the explicit model represented by Götz and Lipowsky [**?**]. In the phantom solvent model, the number of degrees of freedom is not increased significantly, so this model can represent the fluid nature of water, without imposing any immense computational costs as was the case of other explicit models, whose particles interact with each other. Additionally, in this representation, the unwanted artifacts caused by the packing properties of the beads, disappears.

The number of solvent particles is determined according to the ideal gas law, in order to fill the excluded volume of lipid bilayer, leading to exertion of an external pressure on the bilayer. This number is much less than the required number of particles in the other

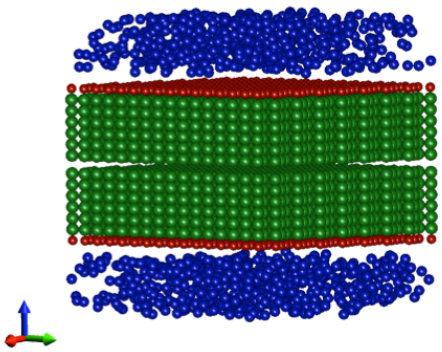

Figure 8.3: The initial configuration of a 16×16 bilayer system. Head beads are presented in red, tail beads in green and solvent beads in blue.

explicit models with self-solvent interacting particles. As a result, the phantom solvent model is still computationally more efficient. The interacting potential is truncated and shifted Lennard-Jones potential as was shown in Equation 8.2. The cutoff radius is determined by the average of the effective interacting radii. The interaction parameters are given in detail in Table 8.1. This model was initially proposed by Lenz and Schmid and fully described in [**?**]. In the following section, the simulation techniques will be explained in detail.

8.4 Details and methods

By using the molecular model presented above, several lipid bilayers were generated according to the phase space of the referenced model [**?**]. In the following subsections, the details of the simulations carried out will be presented, including: the initial structure of the system, simulation techniques and the applied algorithm and parameters. The characteristic quantities calculated for each particular phase will be reported in the next section.

8.4.1 Initializing the system

It has been demonstrated that the Lenz-Schmid coarse grained model has the ability to self-assemble [**?**], therefore in order to save the time simulations were not started from a fully random distribution of separate particles. Instead, simulations were initially carried out with a system in which a set of lipid and solvent particles were positioned in a box in such a way that the system mimics the lipid bilayer pattern (Figure 8.3). In order to thermalize the bilayer system to various points in thermodynamic phase space of the model, a system of particles composed of the total number of 16×16 lipids per leaflet is initialized. Head beads are set in a close packing hexagonal configuration

in the xy-plane. Then, tail beads will be placed in a straight line along the the head beads in the z-direction. By considering an initial fixed size for the box, the number of solvent particles is chosen according to the ideal gas law for every set of particular thermodynamic quantities. Then, these solvent particles are randomly distributed over and under the bilayer leaflets to occupy the free volume of the simulation box. As the simulation will be performed under three-dimensional periodic boundary conditions, these solvent layers can be considered as a separating watery environment between two monolayers.

8.4.2 Thermodynamic parameters

Throughout the second part of this work, all quantities will be measured in the reduced Lennard-Jones units of length σ and energy ϵ. With both σ and ϵ being assigned a value of one, according to the tail characteristic parameters. The other thermodynamic and mechanical parameters will be expressed in these unit:

$$\begin{aligned} \mathrm{E}^* &= 1/\epsilon \ \mathrm{E} \\ \mathrm{T}^* &= \mathrm{k_B}/\epsilon \ \mathrm{T} \\ \mathrm{p}^* &= \sigma^3/\epsilon \ \mathrm{p} \\ \mathrm{f}^* &= \sigma/\epsilon \ \mathrm{f} \end{aligned} \tag{8.5}$$

in which, T^* stands for temperature, p^* for pressure, f^* for force. For the sake of simplicity of notation, asterisks will be omitted for the rest of the thesis. The phase space of the referenced model is depicted in Figure 8.4. In comparison to the experimental results for the DPPC molecules, the length and energy units in the model are converted to SI units by the converting factors as $\sigma \sim \ 6\mathring{A}$ and $\epsilon \sim 3.6 \times 10^{-21}$ J, respectively [?, ?].

8.4.3 Simulation algorithm

After the initializing step, the Monte Carlo algorithm (MC) in isobaric-isothermal ensemble (NPT) was applied to perform the simulation. The NPT ensemble has been chosen to simulate bilayers in the closest conditions to the natural medium for membranes of living tissues. Every MC step in the program consists of a series of the following trial moves:

i) Bead level moves. First, a particle is randomly chosen and the energy of the system is calculated for the initial configuration $\mathrm{U_o}$. Then, the chosen particle will be replaced by a random vector to a new position:

$$\mathrm{r_n} = \mathrm{r_o} + \Delta_\mathrm{m} \ \mathrm{random}[-0.5, 0.5]$$

Δ_{m} represents the maximum magnitude of the displacement vector. At a later stage, it will be discussed that the value of Δ_{m} is regulated in such a way that the sampling scheme acquires the optimum rate of acceptance. The energy of the new configuration after the trial move is calculated and defined by $\mathrm{U_n}$. Then, by implementing the energy difference before and after the move, it is accepted or rejected according to the Metropolis algorithm:

$$\mathrm{acc(o \rightarrow n)} = \min\{1, \exp\left[-\beta(\mathrm{U_n} - \mathrm{U_o})\right]\} \tag{8.6}$$

If the move is accepted, the particle is displaced permanently and the energy of the new configuration will be kept, otherwise the old position and old energy will be retained. This procedure will be repeated for the total number of particles in the system N, which means that, in average all particles are moved at least one time in a cycle. The detailed balance condition is preserved by considering the same *a priori* probability to choose the selected particle in the sequential trial moves. Preserving the detailed balance condition guarantees the correctness of the simulation [**?**].

ii) Volume level moves. For every a few sequential bead moves, for instance every 20 cycles, the size of volume is changed. To this end, every time one of the box dimensions is randomly chosen and scaled by a factor of $1 + \eta$:

$$L_n^{\alpha} \rightarrow = (1 + \eta)\ L_o^{\alpha} \tag{8.7}$$

in which L^{α} is the box side in the α^{th} direction. η is a random value and is chosen in the same way as for displacing particles. Then, the corresponding component of the position vectors of all particles are multiplied by the same factor. The value of η can be positive or negative which results in the extension or shrinkage of the box size. In the same way as the bead moves described above, here the trial box move can be accepted by following the Metropolis criteria for the energy difference before and after the rescaling. For this procedure, the free energy change of the system is governed by Gibbs free energy and the new distribution can be accepted or rejected by the following relation:

$$\begin{aligned} \mathrm{acc(o \rightarrow n)} \;=\; & \min\Big\{1, \exp\Big[-\beta\Big(\mathrm{U}(\mathrm{r_n}, V_{\mathrm{n}}) - \mathrm{U}(\mathrm{r_o}, V_{\mathrm{o}}) \\ & + \mathrm{p}(V_{\mathrm{n}} - V_{\mathrm{o}}) - \frac{N}{\beta}\ln(V_{\mathrm{n}}/V_{\mathrm{o}})\Big)\Big]\Big\}. \end{aligned} \tag{8.8}$$

After a box movement is accepted, the centre of mass of the system will be calculated and the position of all particles will be shifted in such a way that the centre of mass always coincides with the center of the box, otherwise performing the calculation especially for volume move becomes very complicated.

In order to increase the efficiency of the algorithm, the magnitude of the random values, by which particles or box walls are displaced, is regulated so that the acceptance

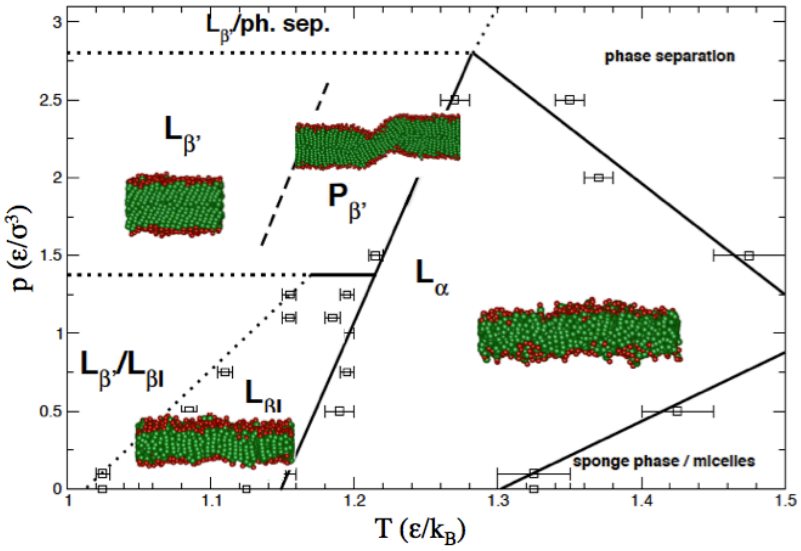

Figure 8.4: Pressure-temperature phase digram of the referenced model. Figure adopted from [**?**]

rates are maintained fixed at around 30% of the total number of trial moves. In order to control the magnitude of the displacement vectors of lipid and solvent particles, the number of accepted steps is counted after every sequential cycle. If this number was larger than the 30% of the trial moves, the magnitude should be multiplied by a number slightly larger than one, to decrease the chance of acceptance and vise versa. For volume rescaling, the acceptance rate is calculated every 50 steps. After about 1000 MC steps, the acceptance rates decay to the desire one.

8.5 Phase behavior

This section presents an overview of the phase behavior of the referenced model. However, retrieving whole phase space diagram was out of the scope of the present work, a few particular points in the phase diagram were picked out to simulate bilayer systems for the rest of this work.

Amongst the possible phases in the temperature and pressure phase space diagram (Figure 8.4), a selection of phases were reproduced in order to study either mechanical properties or dynamical phenomena happening in lipid bilayers. The fluid phase L_α was reproduced by employing high temperature T=1.3 and mediate pressure p=1, the interdigitated phase $L_{\beta I}$ with mediate temperature T=1.16 and low pressure p=0.5 and the gel phase $L_{\beta'}$ with low temperature T=1.08 and high pressure p=2. In addition,

two more phases including ripple $P_{\beta'}$ and sponge phases were simulated according to the appropriate thermodynamic quantities, which are T=1.2 and p=2 for ripple phase and high temperature T=1.4 and very low pressure p=0.1 for sponge phase. The thermodynamic requirements of these phases in addition to their physical characteristics have been explained in Chapter 2. To achieve the equilibration of a system, about 1 million steps were typically required. After the equilibration was achieved, non of the physical observables of the system changed dramatically, and they all reached a plateau. Then, the simulation was continued for about 1million more steps to prepare a system for the measurement purposes of this study. A snapshot of the equilibrated systems in every phase are inserted in the corresponding area in the phase space diagram as is shown in Figure 8.4.

8.5.1 Characteristic parameters of lipid bilayers

For every kind of simulation, a number of parameters are used to describe the simulated system. A few number of these observables, which are mostly describing the structure of lipid bilayer in different phases are average chain length, tilt angle, area per lipid, chain order parameters. A full description of these observables has been detailed in [**?**]. In the present work, the corresponding measurements of the simulated phases are reported, to validate the correctness and accuracy of the simulation and its concordance with the referenced model. These results are represented in Table 8.2.

i) Average chain length $\bar{l}$. The chain length is defined as the connecting vector between the head bead and the final tail bead of the lipid. The average value of this parameter $\bar{l}$, generally reflects how stretched the lipids are in a particular phase. In the fluid phase, as lipid beads have more freedom to move and consequently they are free to bend, the average chain length shows a smaller value with respect to the other phases. In the gel phase, however, lipids are straighter and the average chain length is greater than in the fluid phase but smaller than in the interdigitated phase. This property can be explained by the tilted behavior of the lipids in the gel phase which is not the case for the latter phase. As was expected, the interdigitated phase exhibits the highest value for average chain length, because in this phase lipids are positioned straight along the lipid axis with no tilt.

ii) Thickness d. The z-component of the chain vector can be used to determine the thickness of the bilayer. In this case, the thickness d of the bilayer can be expressed as the difference between the average z-components of lipids in the upper leaflet and in the lower leaflet. Due to the attractive depletion interaction caused by the phantom solvent beads, the head beads are mostly found at the interface between the bilayer and solvent environment. As a result, the thickness of the bilayer is better defined by the difference of the mean value of the z-component of the position vector of head beads located in the upper and lower leaflets. As is expected, the higher the average chain length, the thicker the bilayer. This is true for both the fluid and gel phase, because the bilayer leaflets are sensibly separated in these two phases. However, in

Phase	$\bar{l}$ (σ_{LJ})	d (σ_{LJ})	A (σ^2_{LJ})	S_{z}
Fluid (T=1.3,P=1)	3.3	5.48	1.68	0.42
Gel (T=1.08,P=2)	3.8	7.64	0.96	0.72
Interdigitated (T=1.16,P=0.5)	4.2	4.9	1.78	0.88
Sponge (T=1.4,P=0.1)	5.2	5.5	2.1	0.2
Ripple (T=1.2,P=2)	5.45	7.5	1.05	0.65

Table 8.2: Characteristic parameters of lipid bilayers

the interdigitated phase, lipids of the opposite monolayers are merged together and therefore, they are arranged in such a way that the head bead of one leaflet is located between the tail beads of the other leaflet. As a result the thickness of the bilayer is very small and stays close to the average lipid chain length.

iii) Area per lipid A. The area per lipid is one of the most important observables reflecting the phase behavior of the bilayer. This parameter is roughly defined as the cross sectional area of the box divided by the number of lipids in a monolayer. In this way, the projected area occupied by a lipid is measured in fact, rather than the real spatial one. The gel phase is a well packed phase so its area per lipid has the smallest value compared to the other phases. As was mentioned about the interdigitated phase, the lipid chains of one leaflet positioned between the lipid chains of the opposite leaflet, therefore a large area per lipid is allocated to each lipid. As a result, this phase exhibits the highest area per lipid of all phases studied. In the fluid phase, because the liquidity of the phase causes disordered arrangements of lipids, the area per lipid has a high value.

iv) Chain order parameter S_{z}. The last observable presented here is the chain order parameter. According to the its definition S_{z} is:

$$S_{\mathrm{z}} = \frac{1}{2}\langle 3\cos(\theta) - 1\rangle \tag{8.9}$$

where θ is the tilt angle of the lipid with respect to the normal of the bilayer plane, which here is the z-axis. The chain order parameter quantifies the orientation of lipids with respect to the bilayer normal.

For the fluid phase, due to the random configuration of lipids among the bilayer S_{z} shows the closest value to 0.5. For the interdigitated phase, all lipids are mostly positioned parallel to the z-axis, so it is expected that this phase shows the highest

value for the chain order parameter and is close to 1. The gel phase is a high ordered phase, so it also shows a large value for S_z between 0.5 and 1.

These are a few characteristic parameters through which lipid bilayers are categorized in various phases. Some of these observables can be measured by experimental methods such as NMR and X-ray diffraction. The comparison of the numerical results with the experimental ones, allows the interpretation of the coarse grained units in the real SI units. In addition, experimental results are used with the aim of finding the appropriate behavior in the simulated systems, resulting in tuning the parameters and functions used for simulation models. However, there are many properties and processes which remained far from the experimental possibilities to explore. In these cases, especially, the importance of the simulation techniques is cleared.

8.6 Conclusions

In this chapter, the coarse grained model for lipid bilayer was introduced. In addition, by applying the MC algorithm, bilayers in various phases were reproduced. Some of the observables, through which different phases are known and distinguished, were explained and the result for the present simulations were reported. In the next chapter, mechanical properties of lipid bilayers in different phases, especially the Poisson's ratio and Young's modulus will be investigated by using the simulated bilayers.

9 Mechanical properties of lipid bilayers

9.1 Introduction

Elastic properties play an important role in a number of membrane processes, as for example, membrane fusion [?] and modulations of membrane channel activities [?, ?]. In cells, the outer membranes are supported by the underlying actin networks. The mechanical stress is then dominated by the associated actin cytoskeleton at length scales larger than the mesh size of the actin network (30-300 nm) [?]. On small length scales, however, the contribution of the lipid bilayer will dominates. As such, efforts have been made to study the mechanical properties of bilayer patches with dimensions close to the mesh size of the actin cytoskeleton [?].

When considering a membrane as a two-dimensional body, i.e. neglecting its thickness, its mechanical properties in the absence of anisotropies can be characterized by two elastic constants according to continuum elasticity theory. In common practice of material characterization, these are typically Young's modulus and Poisson's ratio. Estimates for the Young's modulus of membranes have been provided by experiments [?, ?]. However the measuring of Poisson's ratio is not straightforward, due to the small thickness of membranes in the nanometer range [?, ?].

From the theoretical aspect, mechanical properties of lipid membranes are commonly investigated based on the Helfrich Hamiltonian. The main physical quantity obtained from such studies is the bending rigidity. There exists a relation between the bending rigidity, Young's modulus and Poisson's ratio, but neither Young's modulus nor Poisson's ratio have been determined separately so far.

In the present chapter, a method for determining the Poisson's ratio, ν, is introduced and the results of applying this method for a coarse grained lipid membrane model [?] for the fluid, gel and interdigitated phases are presented. After determining the bending rigidity, k_c, from the power spectrum of membrane height fluctuations, one can calculate the Young's modulus, E.

9.2 Poisson's ratio

In the steady state, any materials have a zero average internal strain. It means that the total forces on every part (atom, molecule) of the body is zero. In most cases, when

an object is stretched (compressed) in one direction, it tends to compress (expand) in two other perpendicular directions to compensate the extra strain that is loaded on the body. This effect is called the Poisson's effect and the mechanical quantity that measures this effect named the Poisson's ratio in the honor of Siméon Poisson.

To explain the origin of this effect, looking at the molecular level might be useful. In this level, due to the stretching, the molecular bond lengths increase in the load direction and consequently the bond lengths in the other direction decrease to accommodate the internal stress. By accumulating these small elongations (and also shortenings in the perpendicular directions) throughout the whole body of material, the phenomenon comes out to be observable. However, there are some rare exceptions, in which materials do not obey this pattern and show other behaviors as in the case of auxetic materials. When an auxetic material compress in axial direction, it will shrink in transverse direction. Some zeolites and carbon nanotubes belong to this category. Another different behavior can be found in some material such as cork, in which the transverse contraction will be prohibited by the stiff arms in the structure of this material.

By definition, the Poisson's ratio is the negative ratio of transverse strain variations to the applied axial strain in an object:

$$\nu = -\frac{\mathrm{d}\epsilon_{\mathrm{trans}}}{\mathrm{d}\epsilon_{\mathrm{axial}}}, \tag{9.1}$$

where ν is the Poisson's ratio, $\epsilon_{\mathrm{trans}}$ refers to the transverse strain raised by the implied axial strain $\epsilon_{\mathrm{axial}}$. The axial strain $\epsilon_{\mathrm{axial}}$ is positive if the applied force causes an extension in the body along the direction of the force and is negative if the force compresses the body in that direction, while the opposite signs are true for the transverse strain $\epsilon_{\mathrm{trans}}$. The minus sign in the definition is then considered in the formula to obtain a positive Poisson's ratio for normal materials.

In the infinitesimal limit of applied strain, the Poisson's ratio determines how much the length of the body in direction perpendicular to the applied force changes when its length in the direction of applied force has been changed. It means that, in this limit, we can replace the strain terms in Equation 9.1 by the corresponding relative length changes as follow:

$$\nu = -\frac{\Delta \mathrm{L}'/\mathrm{L}'}{\Delta \mathrm{L}/\mathrm{L}}, \tag{9.2}$$

in which L and L′ are the lengths in the axial and transverse direction, respectively, and ΔL and ΔL′ stand for the change lengths in the corresponding directions.

The theory of elasticity for isotropic materials predicts a positive stiffness for a mechanically stable object. According to the defined relations between the shear and bulk stiffnesses with the Poisson's ratio of an isotropic material, accompanied by the concepts, which are resulted from the second thermodynamics law, it can be proved that

the Poisson's ratio of a free object (not constrained to a substrate) takes a value in the range of -1 to 0.5.

The elastic properties of isotropic materials are direction independent. As a result, these materials have an identical Poisson's ratio for three directions. In contrast, anisotropic materials exhibit directional elastic properties including their Poisson's ratios. For instance, due to anisotropic cellular structure, cork possesses a Poisson's ratio $\nu \approx 0$ in radial growth direction, while it has a Poisson's ratio greater than zero for the perpendicular direction.

Incompressible materials show a Poisson's ratio about 0.5. For these kind of materials, the sum of all strain components in three directions is zero, which means that, no relative volume change is observed within the bulk. It can be simply proved that, the volume change caused by small strains equals the sum of the three diagonal components of the strain matrix.

In the following section, a method will be introduced to measure the Poisson's ratio for membranes with small thickness.

9.2.1 Simulation details

In this section, a computational method, which is applied to estimate the Poisson's ratio for shells of small thickness will be introduced. The thickness of a lipid bilayer is about 80 $\mathring{A}$, which is four order of magnitude smaller than the size of vesicles with a typical diameter of about 10 μm. Hence, a bilayer can be considered as a two dimensional surface. As for one of the characterizing mechanical properties of a body, measuring the Poisson's ratio is experimentally a dilemma for membranes with small thicknesses in the order of nanometer [**?**, **?**].

The present method is based on the rescaling of inter-particle distances in one lateral direction under periodic boundary conditions. In the context of this research, this method was used to calculate the Poisson's ratio for coarse grained lipid bilayers, which were simulated by Lenz and Schmid model (see Chapter 8 and [**?**]). However, this is a general method and can be applied for other surfaces.

To build the initial structure of bilayers, three systems consist of 12×24 lipids per each leaflet were equilibrated by using the isobaric-isothermal ensemble (NPT) for the gel, fluid and interdigitated phases. The temperature and pressure for each phase were chosen with respect to the phase space diagram of the Lenz-Schmid model (Figure 8.4). According to the temperature-pressure phase diagram, these thermodynamics parameters in the reduced units are as follows: T=1.08 and P=2 for the gel phase, T=1.3 and P=1 for the fluid phase and T=1.16 and P=0.5 for the interdigitated phase. For the rest of this section, the Poisson's ratio formula is replaced by the ratio of the relative length changes and is rewritten as:

$$\nu_{\alpha\beta} = -\frac{\Delta \mathrm{L}_\alpha}{\eta_\beta \mathrm{L}_\alpha}, \tag{9.3}$$

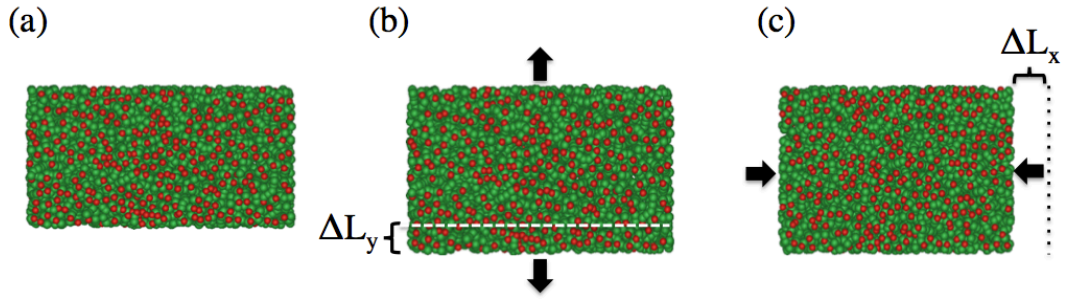

Figure 9.1: Snapshots of the lipid membrane in fluid phase as (a) initial configuration, (b) after increasing the bilayer size in the y-direction by a factor of $(1+\eta)$, and (c) the relaxed bilayer fixing the membrane size in the y-direction and variable the x-direction. As consequence of a predicted positive Poisson's ratio for the bilayer in this phase, the membrane size in the x-direction is reduced and equilibrated after a few number of MC steps.

where $\eta_\beta \equiv \Delta L_\beta / L_\beta$ is defined as the fraction of the axial length change. Here, the Greek indices represent Cartesian coordinates, as such α=x,y and z and $\alpha \neq \beta$.

Once the system was equilibrated and thermalized to the desired phase, the length between neighboring lipids is rescaled by a factor of $(1+\eta)$, for instance in the y-direction. Subsequently, the change of the box size in the x- and z-direction (perpendicular to the extended direction) were monitored. While keeping the rescaled box length $L'_y = (1+\eta)L_y$ constant, for keeping the pressure fixed during the procedure, other box dimensions were allowed to fluctuate. After a few number of MC steps, the mean length in the x- and z-direction, which in this case were L_x and L_z before the rescaling, reached a new mean length $L'_x = L_x + \Delta L_x$ and $L'_z = L_z + \Delta L_z$. Figure 9.1 exhibits these three steps for one of the simulated membranes.

In order to accelerate the thermalization procedure after extending the box along the axial direction, the temperature in the system was slightly increased, which resulted in producing the more mobility for the particles. After rescaling one of the box sides, firstly the simulation was carried out with the original temperature to avoid any unexpected changes in the procedure of the resulted deformation in other sides. As was understood from the procedure, the initial steps are determining steps. Because of this reason, after about 100 MC initial steps, the temperature was switched to a higher amount. In the present cases, for fluid phase with the initial T=1.3 the temperature changed to 1.4 for about extra 400 steps and then switched back to the original value. For the gel and interdigitated phase the initial temperature T=1.08 and T=1.16 switched to T=1.2 and T=1.3, respectively.

As is demonstrated in Figures 9.4 and 9.5, the Poisson's ratio obtained in this way is independent of the rescaling factor, η, as long as η is neither too large which leads to destroy the membrane structure nor too small which does not produce enough free

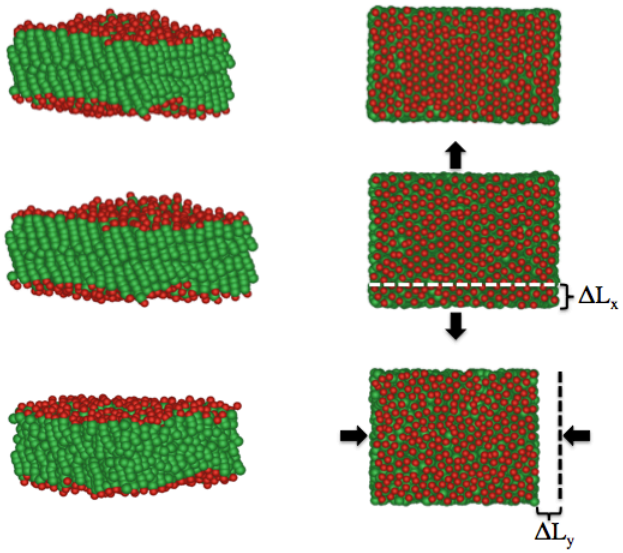

Figure 9.2: Snapshots of the lipid bilayer in gel phase, when initially rescaled the bond lengths in lateral direction of perpendicular to the tilt direction (x-direction) for $\eta = 0.3$.

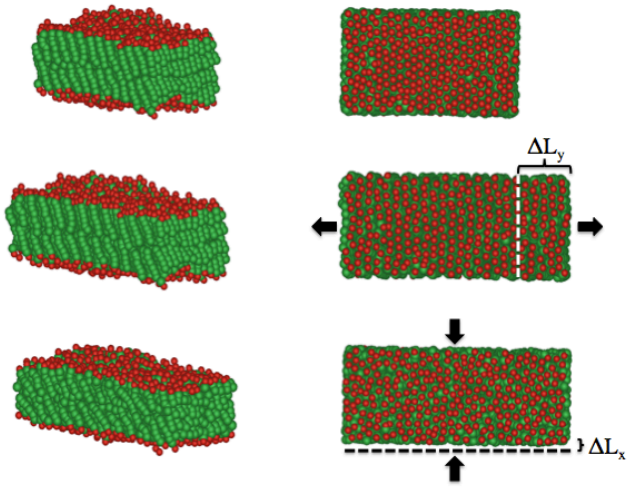

Figure 9.3: Snapshots of the lipid bilayer in gel phase, when initially rescaled the bond lengths in lateral direction of in the tilt direction (y-direction), for $\eta = 0.3$. In this case, less induced compression is observed resulted with respect to the case that elongation was happened in the direction of perpendicular to the tilt angle as is illustrated in Figure 9.2.

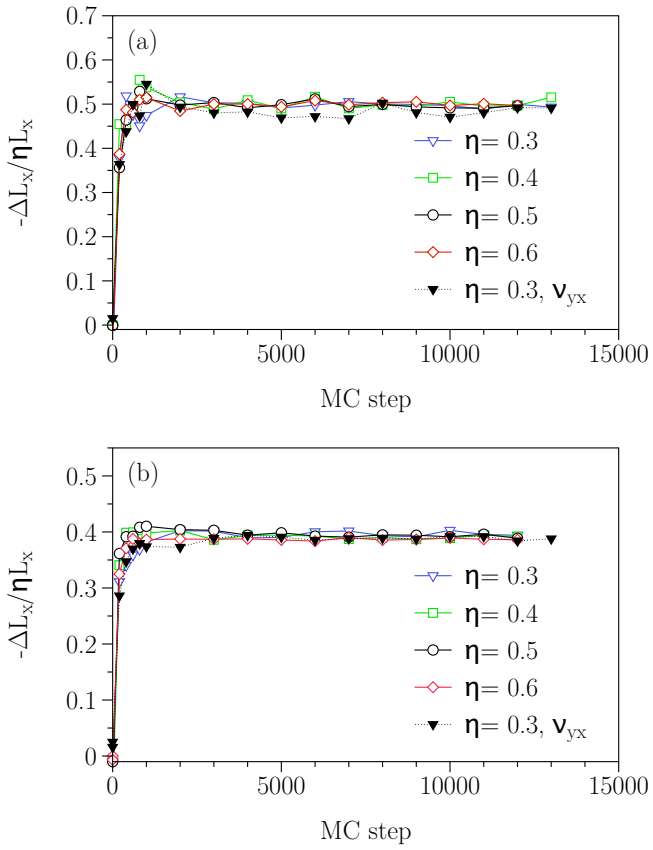

Figure 9.4: Relaxation of $-\Delta L_\alpha/\eta_\beta L_\alpha$ in (a) fluid and (b) interdigitated. The plateau value reached after about 5000 MC steps, independent of the value of η, yields the Poisson's ratio ν. The fluid and interdigitated phases have the identical values for ν_{xy} and ν_{yx}, representing these phases as in-plane isotropic phases.

space for particles to move. In Table 9.1, the obtained Poisson's ratios ν_{yx}, ν_{zy} and ν_{zx}, as well as ν_{xy} for different phases are summarized.

According to the Table 9.1 and Figure 9.4, the fluid and interdigitated phases have the identical Poisson's ratio for both the x- and y-directions. It means that, in these two phases, lipid bilayers are in-plane isotropic. However, this is not the case any more for the gel phase.

It was already examined and shown in [**?**, **?**] that, the gel phase exhibits an in-plane anisotropicity. In this respect, a bilayer in the gel phase behaves as an anisotropic material which has two different Poisson's ratio for two different directions in the plane of the bilayer (Figure 9.5). This is the case for the cork. When the bilayer is expanded in the tilt direction, it does not significantly change in the lateral direction (Figure 9.3). Conversely, when the bilayer was extended in the perpendicular direction to the tilt

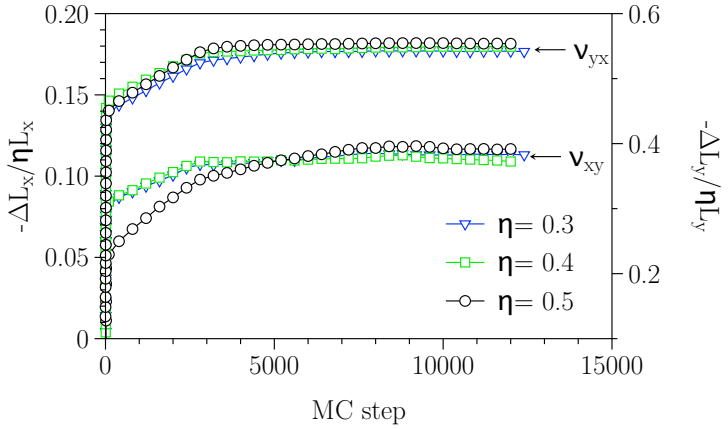

Figure 9.5: Relaxation of $-\Delta L_\alpha/\eta_\beta L_\alpha$ in the gel phase. The plateau value reached after about 5000 MC steps, independent of the value of η, yields the Poisson's ratio ν. In the gel phase, the obtained Poisson's ratio for elongation in the y-direction is $\nu_{xy} = 0.11$ (left axis) and for elongation in the x-direction is $\nu_{yx} = 0.54$ (right axis).

plane, lipids reorganized themselves in a way that the bilayer shrank in the lateral direction (Figure 9.2).

For the present work, lipid bond lengths in the z-direction (perpendicular to the bilayer plane) were not rescaled. The reason is that, to observe the Poisson's effect, the length between the beads should be rescaled by a factor, which produces enough space for particles to rearrange. It means that the bonded beads inside a lipid should be distanced too much, which results in bond breakages and consequently, the structure of molecules and the nature of the simulated material will be affected. Therefore, the reported values for ν_{zx} and ν_{zy} are relative length changes in the bilayer mean length due to the lateral extension of bilayer in x- and y-direction, respectively.

9.3 Fluctuation spectrum

A common analysis of the elastic properties of a membrane relies on the Helfrich Hamiltonian [**?**], which describes the cost of elastic free enthalpy associated with fluctuations of the membrane height (deviations from flat surface). When parameterizing the membrane in Cartesian coordinates, $(x, y) \rightarrow (x, y, h(x, y))$ according to Monge gauge, the Helfrich Hamiltonian is, for small fluctuations, given by:

$$H = \int dx\, dy \left[\frac{k_c}{2} \left(\nabla^2 h \right)^2 + \frac{\varsigma}{2} \left(\nabla h \right)^2 \right], \tag{9.4}$$

where k_c is the bending rigidity and ς is the surface tension. Equation 9.4 is applied

when the membrane is considered as a body with negligible thickness. A generalized elastic theory for membranes with finite thicknesses was suggested by Brannigan and Brown [**?**] and recently applied to the Lenz-Schmid model [**?**, **?**].

In order to investigate the power spectrum of the surface height fluctuations for the referenced phases, three bilayer systems in the fluid, gel and interdigitated phases with corresponding thermodynamics parameters mentioned above, consist of 64 × 64 lipids per leaflet, were thermalized under constant temperature and pressure condition (NPT ensemble). According to the initial box size for each phase, the number of solvent beads was chosen in a way that the ideal gas law was satisfied. The corresponding solvent number is N_{solvent} =16896, 30160 and 72624 for the interdigitated, fluid and gel phase, respectively.

In order to determine the surface height, h(x,y) at each point, the bilayer xy-plane was discretized into a regular grid with spacing $2\sigma_{\text{LJ}}$. Each cell is specified by indices (α, β). Firstly, the z-component of each cell at upper and lower leaflets was replaced by the z-component of the corresponding head bead, which was located at that cell. In order to correct the mesh, if a cell contained more than one lipid, the average value of the z-components of heads' position vector was calculated and assigned as the cell height, and if a cell had no head inside it, the average value of the neighboring cells' height was, then, considered as the cell height. The mean z-coordinates, $\mathrm{z}_+(\alpha,\beta)$ and $\mathrm{z}_-(\alpha,\beta)$ of head beads in the upper and lower leaflet, respectively, were used to calculate the height for each cell, such that $\mathrm{h}(\alpha,\beta) = [\mathrm{z}_+(\alpha,\beta) + \mathrm{z}_-(\alpha,\beta)]/2$. Subsequently, the average $\bar{\mathrm{h}}$ of the resulted mesh was subtracted.

For a membrane of lateral size $\mathrm{L_x} \times \mathrm{L_y}$, Equation 9.4 predicts that the power spectrum of the fluctuations behaves as:

$$\langle |\hat{\mathrm{h}}(\mathbf{q})|^2 \rangle = \frac{\mathrm{k_B T L_x L_y}}{k_c \mathrm{q}^4 + \varsigma \mathrm{q}^2}, \tag{9.5}$$

where $\hat{\mathrm{h}}(\mathbf{q})$ is the Fourier transform of h(x,y) at wave vector $\mathbf{q}$ and $\mathrm{q} = |\mathbf{q}|$. Brackets $\langle \ldots \rangle$ denotes an equilibrium average. In the numerics, $\hat{\mathrm{h}}(\mathbf{q})$ is calculated from a discrete Fourier transform of $\mathrm{h}(\alpha,\beta)$, according to the relation:

$$\hat{\mathrm{h}}(\mathrm{q}_\alpha, \mathrm{q}_\beta) = \frac{\mathrm{L_x L_y}}{N_\mathrm{x} N_\mathrm{y}} \sum_{\alpha,\beta=1}^{N_\mathrm{x}, N_\mathrm{y}} \mathrm{h}(\alpha,\beta) \exp^{-2\pi \mathrm{i}[(\mathrm{x}_\alpha \frac{\mathrm{q}_\alpha}{\mathrm{L_x}}) + (\mathrm{y}_\alpha \frac{\mathrm{q}_\beta}{\mathrm{L_y}})]}, \tag{9.6}$$

where $N_\mathrm{x} = \mathrm{L_x}/2\sigma_{\text{LJ}}$ and $N_\mathrm{y} = \mathrm{L_y}/2\sigma_{\text{LJ}}$. Subsequently, $\hat{\mathrm{h}}(\mathbf{q})$ was obtained at each cell point by calculating the sum of the corresponding $\hat{\mathrm{h}}(\mathbf{q})$, for which $\mathrm{q} = (\mathrm{q}_\alpha^2 + \mathrm{q}_\beta^2)^{1/2}$, as follow:

$$\hat{\mathrm{h}}(\mathbf{q}) = \sum_{\alpha,\beta=1}^{N_\mathrm{x}, N_\mathrm{y}} \hat{\mathrm{h}}(\mathrm{q}_\alpha, \mathrm{q}_\beta). \tag{9.7}$$

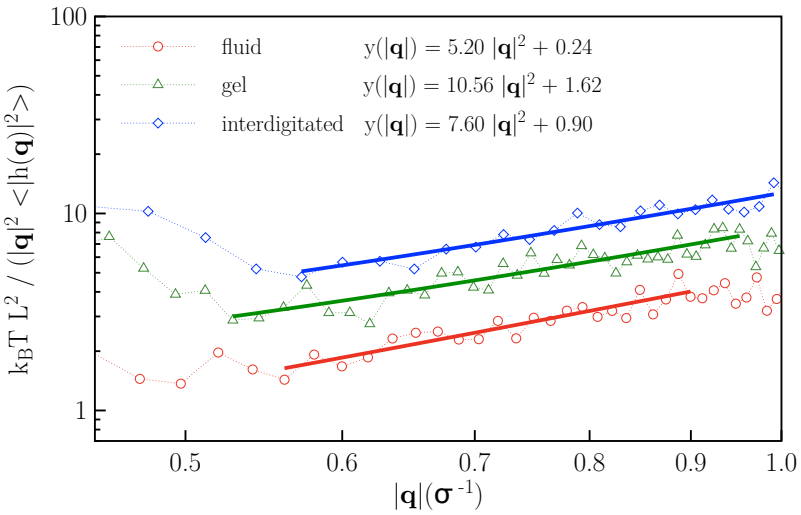

Figure 9.6: Fluctuation spectra for three phases.

It is clear that Equation 9.5 can be true only for a q-range $2\pi/\mathrm{L} \ll \mathrm{q} \ll 2\pi/\sigma_{\mathrm{LJ}}$, where neither the finite system size nor the (atomistic) bead size affects the fluctuations. The corresponding q-range for system sizes amenable within reasonable computing time is unfortunately not large, but fits of $\langle|\hat{\mathrm{h}}(\mathbf{q})|^2\rangle/\mathrm{k_B T L_x L_y}$ as function of q^2 in a range $0.2 \leq \mathrm{q}^2 \leq 1$ yield a good agreement with Equation 9.5 for present sizes.

The values obtained for the bending rigidity, k_{c}, are 5.2ϵ for the fluid phase, and 10.56ϵ for the gel phase, which are in agreement with previously reported values by [?], and they also are in reasonable agreement with experimental findings [?, ?]. It should be mentioned that, the bending rigidity of the gel phase was investigated only in one direction. However, it was already discussed that [?], the corresponding values in the tilt direction and the perpendicular to that are different. The spectral density for the interdigitated phase was calculated according to the same method, resulted in a bending rigidity of about 7.6ϵ. Figure 9.6 shows the fluctuation spectrum for three phases.

9.4 Young's modulus

According to the definition from the theory of elasticity, the modulus of extension or the Young's modulus, E, for an isotropic material is the ratio of stress element along the loading direction to the resulted strain on the loading plane, that is:

$$E = \frac{\sigma_{\alpha\alpha}}{\epsilon_{\alpha\alpha}}.$$

Here, α represent a Cartesian coordinate along the loading direction. Logically, an

phase	$k_c\,(\epsilon)$	ν_{xy}	ν_{zy}	ν_{yx}	ν_{zx}	$E(\epsilon/\sigma^3)$
gel	-	0.11	0.44	0.54	0.04	–
fluid	5.20	0.50	0.25	0.48	0.26	0.27
interdigitated	7.60	0.40	0.12	0.37	0.13	0.67

Table 9.1: Elastic constants obtained from simulations of lipid membranes in different phases

isotopic material would be extended due to the uni axial tension in the loading direction. It is also can be concluded from the second law of thermodynamics. Hence, the Young's modulus should be positive for all these materials.

Within two-dimensional elasticity theory [**?**], the bending rigidity, k_c is related to the Poisson's ratio ν and the Young's modulus E according to:

$$k_c = \frac{Ed^3}{12(1-\nu^2)}, \tag{9.8}$$

where d is the mean membrane thickness, for which the obtained values are $5.48\sigma_{LJ}$, and $4.86\sigma_{LJ}$ for the fluid, and interdigitated phases, respectively. As the gel phase exhibits an in-plane anisotropicity, two different values were obtained for that phase.

Substituting the found values for the Poisson's ratios and the bending rigidities for bilayers in two isotropic phases into Equation 9.8, one can obtain the corresponding Young's moduli. The Young's moduli, which were calculated in this way are 0.28 and 0.67 in units of ϵ/σ^3, for the fluid and interdigitated states, respectively. Obviously, the observed anisotropicity in the gel phase does not allow to use the above theorem for the bilayer in this phase. The estimated elastic moduli are summarized in Table 9.1.

9.5 Conclusions

Monte Carlo simulations were performed for the lipid bilayer model of Lenz and Schmid to gain insight into the mechanical properties of planar lipid membranes. By using a rescaling method, the Poisson's ratio, ν, for different phases was calculated. In addition, the bending rigidity, k_c, was determined by performing an analysis of the membrane height fluctuations based on the Helfrich Hamiltonian. Calculations for the fluid and interdigitated phases showed that, these two phases are isotropic. It was not the case for the gel phase, which exhibits nonidentical elastic moduli for different directions in the bilayer plane. Having the Poisson's ratio and bending rigidity, allows to calculate the Young's modulus, E, for the isotropic phases.

10 Lipid translocation and pore formation

10.1 Introduction

Living cells are in nonequilibrium states, open to exchange with their environments. Maintenance of a continuous intracellular trafficking of molecules underlies cell survival [?]. In the last decades, a large body of information has been gathered concerning membrane protein synthesis and trafficking [?]. In contrast, the mechanism underlying lipid transport from the endoplasmic reticulum (ER) -where the lipids and proteins are synthesized- to their final destination remains to be clarified [?].

Cellular membranes have been viewed as a double layer of lipids in which proteins are embedded, the so-called fluid mosaic model (Figure 1.1). In recent years, however, it is increasingly recognized that biological membranes are often far from being homogeneous and symmetrical, and differ from the canonical fluid mosaic model in many ways [?]. As was discussed in Chapter 2, asymmetry of the lipid distribution between the leaflets is an important feature of most biomembranes with important functional consequences [?]. This is particularly seen in plasma membranes (PM), in which for instance Phosphatidylethanolamines (PEs) are enriched in the cytoplasmic leaflet. To establish asymmetric membrane lipid composition, transbilayer movement of lipids from one leaflet to the other is required [?]. Endoplasmic reticulum membranes, on the other hand, have symmetric lipid distributions. Phospholipid synthesis takes place almost exclusively in the cytoplasmic leaflet of the ER, which leads in principle to an asymmetry in lipid composition. In order to maintain the balance of lipid molecules in the ER, about one-half of the newly synthesized lipids are transferred to the other leaflet.

The investigation of the atomistic mechanisms of passive (not catalyzed by ATP dependent flippases) lipid flip flop processes constitutes a challenge to both in theory and experimentally [?]. Experimental methods have their own limitations and disadvantages. For instance, in fluorescence spectroscopy and electron spin resonance, labeling the target molecule causes inaccuracy in the rate of flip flop [?].

To overcome these limitations, computer simulations are widely being used to address the subject and investigate the underling mechanisms and thermodynamics of the process. Several computational works, including all atomistic [?] and coarse grained models [?, ?] have studied the flip flop procedure for different kinds of lipids through

diverse computational methods such as potential of mean force (PMF) [?], transition path sampling (TPS) [?] and umbrella sampling [?, ?]. In the following, some of the results of these works will be summarized in tables.

In the resting state, lipid flip flop is often an extremely low rate process with one single lipid flip flop event in hours to days [?, ?, ?]. This is attributed to the high energy barrier imposed by the resistance to the passage of hydrophilic head groups through the hydrophobic core. It has previously been shown [?] that the lipid flip flop is usually associated with the formation of water pores or defects, which are energy consuming processes. Moreover, the resistance enforced by the increased lateral tension developed in the receiving monolayer, when the new phospholipid is inserted, also contributes to the procedure. As a result, the nature of the rate limiting step in unassisted flip flop processes has been a topic of much debate. Some studies indicate that the lipid transport is limited by the rate of dissociation from the lipid bilayer [?]. Others provide evidence that the rate of crossing from one hemi-leaflet to the other is the main limiting factor [?]. To find reliable answers to these questions, evaluation of the free energy profile of the process is a matter of great interest and was explored in the present work.

In this chapter, by applying the so-called nonequilibrium thermodynamic integration method, proposed by Jarzynski [?, ?], the free energy difference associated with the lipid flip flop process is calculated and the free energy barrier of such events in the fluid and gel phases is estimated. Also, the free energy cost of inter-membrane lipid translocation (monomeric exchange) is studied. Finally, the free energy of the formation of water pores within a bilayer is calculated.

10.2 Method

Calculation of free energy is of great importance for understanding the kinetics of the flip flop process. Such calculations, however, require extensive sampling of configurational space and therefore are extremely costly for complex systems [?] like bilayer membranes. Effort has been made based on equilibrium or quasi-static simulations, such as thermodynamics integration and umbrella sampling to calculate the free energy barrier of biomolecular processes including the membrane lipid flip flopping [?, ?, ?, ?, ?]. The recent discovery of Jarzynski's identity opens the possibility of calculating free energies from nonequilibrium processes [?, ?]. In this section, the Jarzynski method for the estimation of the free energy for a nonequilibrium process is introduced. The force formulae, which were used in order to calculate the work in the present simulation, will be explained in detail in Appendix B.

10.2.1 Free energy estimation

Unassisted flip flop processes usually happens over a nanosecond time scale. The system does not preserve its equilibrium state during the evolution trajectory of the exchange

process, which occurs at non- or quasi-equilibrium conditions. The calculation of the thermodynamic quantities in the nonequilibrium conditions is not a straightforward procedure. According to thermodynamics theories, for a system in contact with a heat reservoir, when the system evolves through an equilibrium process, the required work that has been done on the system is equal to the Helmholtz free energy difference of the system in transition from the initial to the final points of the evolution trajectory. A nonequilibrium process is an irreversible process and a part of the free energy is dissipated in the form of an increase in the entropy of the system. Therefore, the equality of the efficient work and free energy difference for changing the state of the system between two equilibrated states, is not preserved anymore. In order to solve this problem, for the first time, Jarzynski proposed a most useful and simple formula for the estimation of the free energy difference of the evolutionary system. According to the Jarzynski equality, the free energy difference ΔF between two equilibrium states is given by [**?**]:

$$\Delta F = -k_B T \ln\langle \exp(-W/k_B T)\rangle \tag{10.1}$$

in which k_B is the Boltzmann constant, T is the temperature, and $\langle \cdots \rangle$ denotes an ensemble average over a distribution of (microscopic) work values W. Because of this reason, for performing an ensemble of work measurements, the system should be initially equilibrated, such that all system characteristic parameters reach their fixed mean values and only the fluctuation around mean values is accepted. Then, by choosing different paths to cross the transition trajectory in configurational space of the system, and also different switch rates along the paths, the required work for the transition of the system from the initial state is calculated. The average thickness of the bilayer is used to determine the final stable state. By performing an average over the ensemble of these nonequilibrium measurements and employing Equation 10.1, the equilibrium free energy difference will be evaluated. By applying this method, in the next sections, the lipid translocation phenomenon across membranes will be investigated.

10.3 Lipid translocation

Lipid flip flop is a biological phenomenon during which one lipid or cholesterol is displaced from one leaflet to the other. Many computational studies have proposed that transient pores are the most important pathways for passive phospholipid flip flop across the membrane [**?**, **?**, **?**], a process that happens over a nanosecond time scale. In the absence of pores, the time scale for flip flop would be on the order of hours. The rest of this chapter is devoted to the investigation of this phenomenon by using the coarse grained model presented in Chapter 8. Comparing the results obtained by this method with the other simulation models and experimental findings will illustrate the potential and drawbacks of this model to study the flip flop phenomenon.

10.3.1 Transmembrane lipid translocation (Flip Flop)

The free energy barrier of the flip flop process was investigated by means of the Lenz-Schmid coarse grained model which was introduced in Chapter 8. For the aim of this work, two bilayers composed of 12×12 lipids per leaflet were equilibrated to fluid and gel phases. The isobaric-isothermal (NPT) ensemble was used to thermalize the systems. The thermodynamics parameters of these phases are as follows: A high temperature and mediate pressure fluid phase, L_α, with $T = 1.3\ \epsilon/k_B$ and $P = 1\ \epsilon/\sigma^3$ and a low temperature and high pressure gel phase, $L_{\beta'}$, with $T = 1.08\ \epsilon/k_B$ and $P = 2\ \epsilon/\sigma^3$. The reduced parameters ϵ and σ are the Lennard-Jones interaction strength and radius, respectively.

Once the system is equilibrated, one lipid is arbitrarily chosen and its head is excluded from the usual moving process in a MC step. This means that after equilibration, in each MC step, all lipid particles are randomly selected and displaced except for the head of the flip flopping lipid. Instead, the head of the targeted lipid will be urged to move very slowly in a specific direction to make a lipid flip flop along the bilayer. Assuming that the mentioned lipid is initially in the upper leaflet, every 20 steps it's head is pushed about 0.001 σ in the z-direction, perpendicular to the plane of the lipid membrane, to reach the lower leaflet. During this procedure, tail beads of the selected lipid are moving in such a way that they adapt themselves according to the new position of the head bead. This part of the simulation is performed at a canonical ensemble (NVT). Figure 10.1 illustrates the transmembrane lipid translocation in the fluid phase bilayer.

To be able to apply the Jarzynski method, the system should also end up in an equilibrated state. For this purpose, half of the thickness of the bilayer which corresponds to the location of the head beads is considered as the final position of the given head bead. Once the head bead of the targeted lipid has arrived at this distance from the middle plane of the bilayer, the flip flop process completes. However, to examine that the assumed position for the final state of the lipid was correctly chosen, the urging movement was continued by pulling the lipid out of the bilayer into the solvent bulk. As the targeted lipid travels across the bilayer, or is being brought out of its original leaflet into the water environment, the total force acting on lipid's centre of mass is calculated (see Appendix B for force formulae). The work required for moving the particle is obtained by integrating over the trajectory. In each phase, by generating a large number of stable states, an ensemble of about 50 several trajectories along them was produced. Using this ensemble, a distribution of the calculated works for the flip flop process was performed.

It should be noted that, the trajectories can be taken from quite general driving protocols of control variables that lead the system from the initial to the final state. It is not necessary that the driving process be sufficiently slow in order to establish a quasi-equilibrium state during the process, as would be the case when the free energy difference has to be determined from the (macroscopic) mean work in conventional

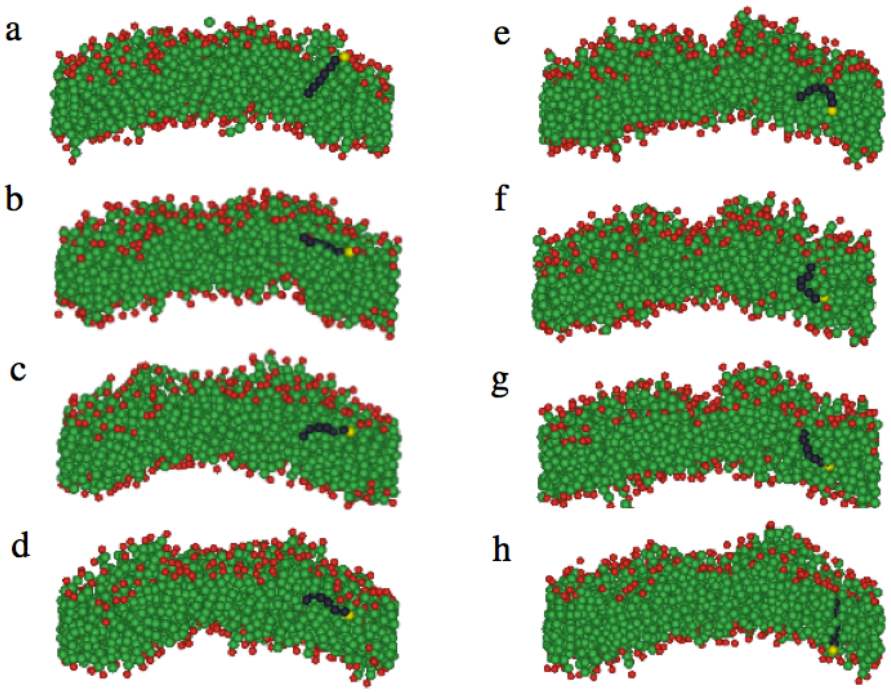

Figure 10.1: Snapshots of a single lipid translocation path across the fluid bilayer. (a) The targeted lipid is initially located on the upper leaflet and (b-g) The targeted lipid is urged to move downwards to reach to the lower leaflet. (h) Finally, the system is equilibrated for the new configuration.

thermodynamics. The work distributions for the fluid and gel phases are depicted in Figure 10.2.c and d.

Using the Jarzynski equality Equation 10.1, free energy profile for each system was obtained and illustrated in Figure 10.2.e and f. The two-minima structure of free energy are evident from Figures 10.2.e and f, which correspond to the head positions in the bilayer. The position of the head particles are shown in the Figure 10.2.a and b, by estimating the density distribution of these particles as well as two other types of particles in the system.

Two observed minima along the free energy profile are linked with steeply rising trajectories, with their difference showing the free energy cost for the displacement of the lipid across the bilayer. The estimation shows a difference in free energy of the system of $\Delta F \sim 6.4\ \epsilon$ and $\Delta F \sim 32\ \epsilon$, caused by the flip flop procedure in the fluid and gel phases, respectively. The higher barrier in the gel phase is evidence of the rareness of the phenomenon in this phase. By using the converting factor for energy (which was measured to be $\epsilon \sim 3.6 \times 10^{-21} J$ [**?**, **?**]), it is possible to interpret the free energy barriers in real SI unit.

Comparison of the present results with other experimental and computational find-

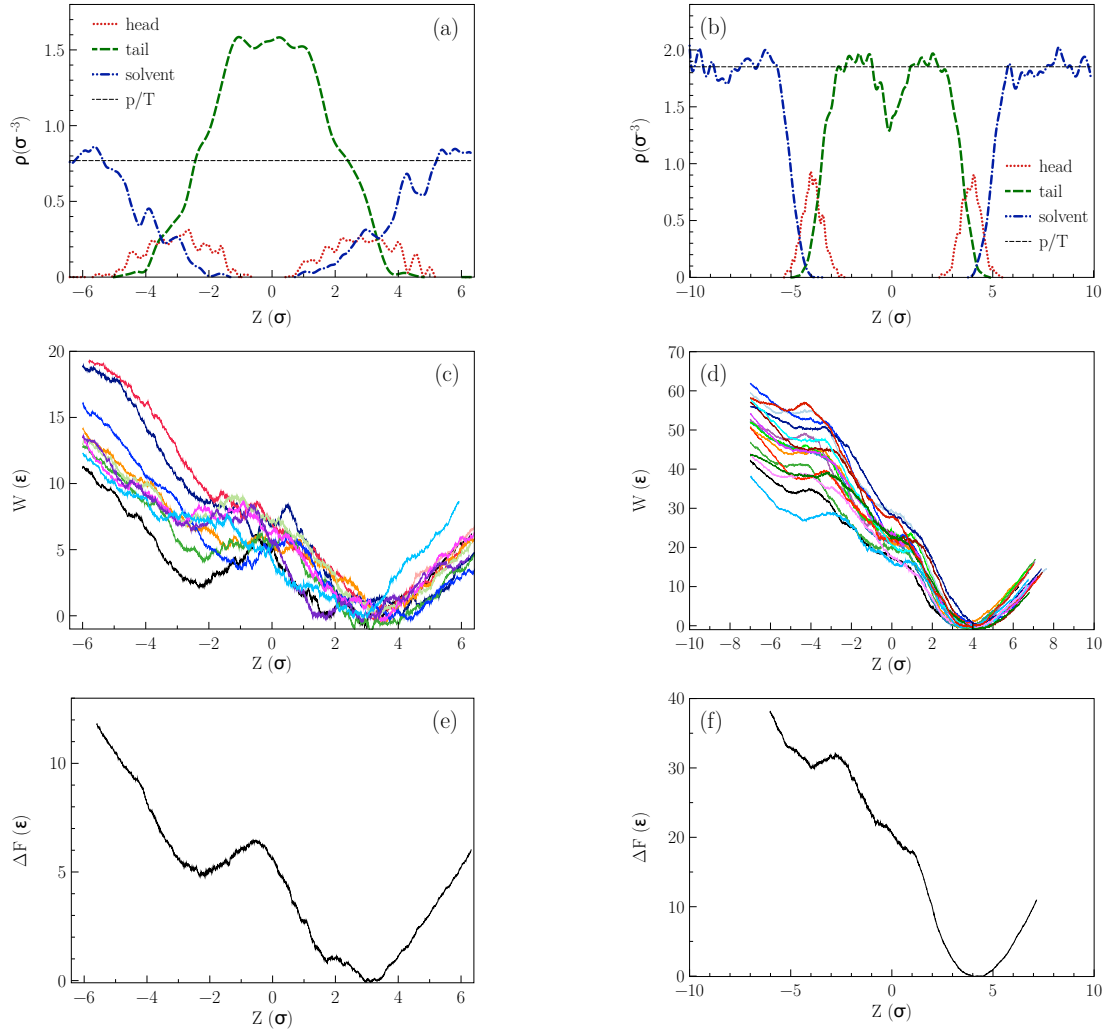

Figure 10.2: Density profiles of lipid and solvent particles in the fluid (a) and gel (b) phase. Work profiles as a function of the displacement of a selected head bead, urged to move from the upper to the lower leaflet, for different realizations of the process in the fluid and gel phases are shown in plots (c), (d), respectively. Free energy differences estimated from the distribution of work are depicted in plots (e), (f) for the fluid and gel phase, respectively. $N_{\text{path}} = 50$ paths are used to perform the average in the Jarzynsky equality. The higher energy barrier in the gel phase illustrates the lower rate of the flip flop in this phase with respect to the fluid phase.

Lipid	Pore-independent (kJ/Mol)	Pore-dependent (kJ/Mol)	Monomeric exchange (kJ/Mol)	Model/force field	reference
CG lipid (fluid)	15	-	15	CG	Present model
CG lipid (gel)	70	-	43	CG	Present model
DPPC/Cholestrol	24	-	-	CG	[?]
DPPC(298K)	80	-	-	CG	[?]
DPPC/Cholestrol	-	-	80	CG	Bennet (unpublished)
TEMPO-DPPC	-	79	-	experiment	[?]
DPPC	-	81	-	experiment	[?]
CG lipid (298K)	15	-	-	CG [?]	[?]
DPPC	-	78	-	AA	[?]
DLPC	-	16	-	AA	[?]
POPC	87	-	-	AA	[?]
DOPG/DOPC	105	-	-	AA	[?]
DMPC	-	37	-	AA,$\text{water}_{\text{Bundled}}$	[?]
DPPC	80	-	-	CG	[?]
DLPC	73	-	-	CG	[?]
DOPG	59	-	-	CG	[?]
DPPC	-	87	-	$\text{CG} - \text{pol} - \text{lj}^{+}$	[?]
DLPC	-	55	-	$\text{CG} - \text{pol} - \text{lj}^{+}$	[?]
DPPC	87	-	-	CG-pol	[?]
DPPC	90	-	-	CG-pol(PME)	[?]
DLPC	73	-	-	CG-pol	[?]
DLPC	73	-	-	CG-polPME)	[?]
DOPG	77	-	-	CG-pol	[?]
DOPG	110	-	-	CG-pol(PME)	[?]
DPPC	150	-	-	CG,$\text{water}_{\text{BMW}}$ [?]	[?]
DLPC	122	-	-	CG,$\text{water}_{\text{BMW}}$ [?]	[?]
DLPC	-	60	-	$\text{CG} - \text{lj}^{+}$	[?]

Table 10.1: Comparison of the free energy barrier for the lipid translocation process estimated by different experimental and computational methods.

ings shows an underestimation in the energy barrier by this model. In Table 10.1 the results of several methods are summarized. One reason for the underestimation can be traced back to the very simplified interactions of the model. One of the biggest limitations of this model is the lack of polar interaction and charged particles in the system. This deficiency results in the inability of the model to reproduce the water defects which are associated with the flip flop process. Since water defects and pore formations are high energy consuming processes, the inability of the model to represent them can explain the underestimation in the free energy cost of the procedure. The ef-

fect of polar interactions has already been investigated by means of the coarse grained MARTINI force field [?]. This study showed that by including an electric dipole in water molecules, pores were created inside the membrane due to the electroporation. In addition, the presence of polar water molecules results in an improvement in the magnitude of the free energy barrier. However, even by applying this model, no water defect and poration were produced during the flip flop process (i.e. in the absence of the electric field). It was later demonstrated that the soft core repulsive Lennard-Jones interaction between head groups and water molecules is responsible for the lack of observation of water defects during the process and results in the underestimation of the required energy barrier [?]. Another reason for the underestimation is that for calculating the required work, only the motion along the z-direction was considered, however, all types of molecular movements contribute to the potential energy barrier. The rate of pulling out the lipid molecule is also another limiting parameter. It was shown that the slow force movements lead to higher energy estimations [?]. However, it does not affect the shape of the energy profile.

It was also shown that pulling out a lipid from its equilibrium position in the bilayer to the aqueous environment requires an amount of work [?] and this work is equal to the free energy difference of system between these two states. In the next section, inter-membrane lipid translocation will be discussed and the free energy cost required to transfer a lipid from the bilayer into the aqueous phase will be estimated with the same methods.

10.3.2 Inter-membrane lipid translocation (Monomeric Exchange)

The present approach can be applied to study monomeric exchange processes during which a lipid molecule is exchanged between two neighboring bilayers [?, ?]. Membrane lipid molecules generally have a low monomer concentration in the aqueous phase and therefore have a tendency to redistribute spontaneously between membranes [?, ?, ?, ?, ?, ?, ?, ?, ?]. The monomeric exchange of lipids is a crucial and efficient transport mechanism in particular for organelles like mitochondria and chloroplasts that are not connected to vesicular pathways and are unable to synthesize their own full repertoire of lipids [?]. The rate limiting step in the monomeric exchange process is attributed to the desorption step and depends on the tail length: short chain lipids such as PCs desorb within minutes while long chain lipids have extremely slow desorption (within days) [?].

In order to investigate the monomeric exchange of lipids and calculate the free energy barrier to pass a lipid between two different bilayers and finally its absorption by a monolayer, a series of simulations was performed with the same methods that have been described for the flip flop procedure in the previous subsection. To simulate this procedure, firstly an arbitrary lipid is chosen and pulled out from the bilayer toward the solvent space in the simulation box. As simulation is performed in periodic boundary conditions, the water bulk acts as a separating layer between two monolayers. So, two

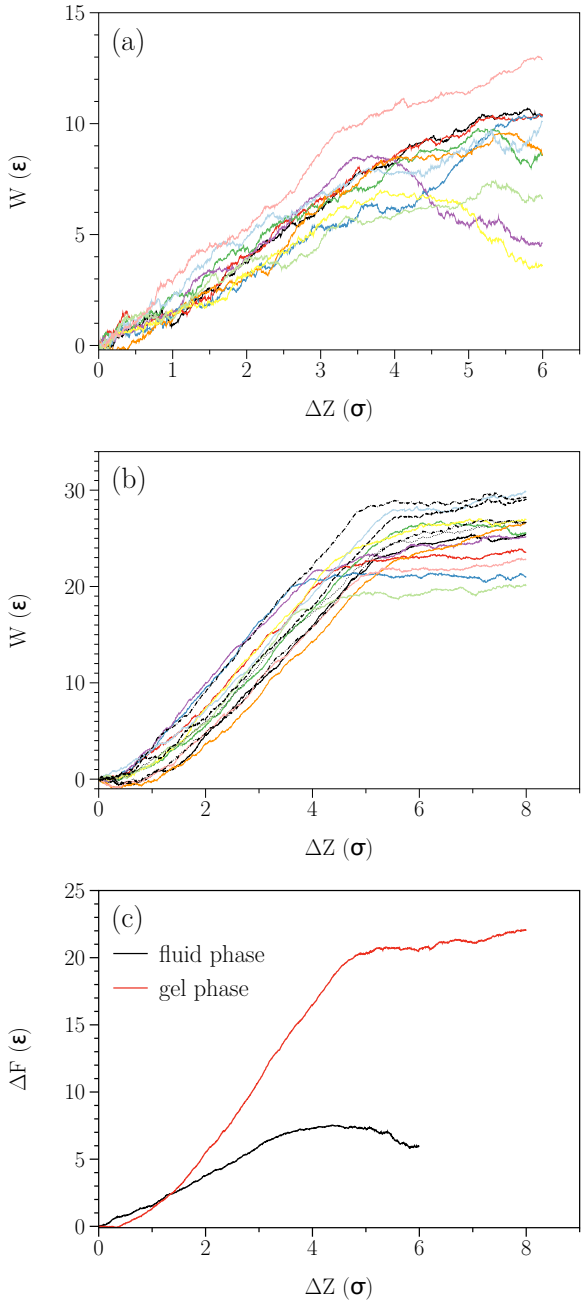

Figure 10.3: Work distributions as a function of displacement of a selected head bead, urged to move from the upper to the lower leaflet, for different realizations of the process in the fluid phase (a) and gel phase (b). (c) Free energy differences calculated from the distribution of the work from $N_{\text{path}} = 50$ for both phases.

monolayers can be considered as monolayers of different bilayers. By continuing the forcing movement until the lipid reaches the other monolayer, it starts to be absorbed by the new monolayer. Thereafter, the targeted lipid is free to follow ordinary movements as the other lipids. After quite a few steps, the lipid is completely absorbed by the monolayer and the monomeric exchange procedure is complete. In Figure 10.3, the free energy cost required to transfer a lipid from the bilayer into the aqueous phase is depicted.

The free energy profile shows a steady rise from the initial equilibrium location of the lipid to the water-bilayer interface. Apparently, there is no considerable energy barrier to make the lipid become free from the bilayer and the energy profile suddenly flattens by releasing the lipid in to the solvent. Once the lipid is immersed in the aqueous bulk, the free energy trajectory reaches a plateau value.

As was explained already, no water pore has been formed during the flip flop procedure simulated by the model presented here, and this is an important shortcoming in the use of the model. An interesting question therefore arises as to how much work is needed to perform one pore within the membrane harvested by the Lenz-Schmid model. This will be investigated in the next section.

10.4 Pore formation process

To release materials that are enclosed within a bilayer, one strategy is to induce nano-pores/ruptures within the bilayer allowing for material transport such as ion permeation [**?**] or lipid translocation [**?**]. Since these pores are transient, a lipidic gate can be opened and closed at a desired time. The transient nature of lipid nano-pores has made it difficult to precisely study their structure by experiments; thus many efforts have recently been made to investigate the origins, properties and functionality of pores by computer simulations both at the atomistic and coarse-grained levels [**?**, **?**]. Although pores can form spontaneously, various operations enforce this procedure. Here some of the most important pore-inducing agents and conditions are briefly mentioned.

i) Electric field poration. One of the best-known ways to create pores is by exerting electric potential differences to the membrane of a cell. Experimentally, electric pulses produced by high-energy lasers are applied to the cell membrane. Computationally, the proper potential difference across a membrane is produced either by applying a constant electric field [**?**, **?**, **?**, **?**, **?**, **?**, **?**, **?**, **?**], or by creating an ionic imbalance around the membrane, which causes an electric field responsible for pore formation [**?**, **?**, **?**, **?**]. As a result of the electric field, water molecules can penetrate into the membrane. The process of opening a pore usually starts by spreading of water molecules throughout the membrane. When water molecules permeate the membrane, some small water defects form around the lipid head groups. A pore will later be stabilized when the head groups move towards this initial pore. The pore then enlarges and becomes lined with lipid head groups and the head groups distribute evenly over the pore surface [**?**].

ii) Pore formation induced by mechanical stress. Mechanical stress such as osmotic swelling can also induce pore formation in membranes. In this case pores are formed as a response of the membrane to the surface tension. To simulate a membrane under different levels of surface tension, one possibility is to change the surface density of lipids. Forming a pore requires a critical threshold surface strain, which depends on the lipid composition and environmental condition [**?**, **?**]. By estimating the free energy of the system, the stability of pores can be investigated. Several methods have been proposed to calculate free energy differences in membrane systems caused by pore formation. One possibility is to use constraint forces to calculate the free energy profile for pore formation as a function of pore radius [**?**, **?**, **?**]. Another option is to calculate the free energy of pore evolution by pushing a lipid molecule into the bilayer interior in a reversible manner [**?**]. During this process, a small water pore forms spontaneously.

iii) Pore formation in lipid membranes by peptides. One of the main pharmacological mechanisms for killing microbial cells is by antimicrobial peptides, which form pores in the bacterial cell membrane, leading to ion influx and cell death. Typically, amphipathic peptides containing lysine and arginine residues are able to induce pores. Pore formation occurs when the hydrophobic parts of the peptide are in contact with the lipid membrane and the polar residues face the water. Usually, formation of a toroidal membrane-spanning pore is the result of the cooperative self-assembly of five to six magainin (an antimicrobial peptide) molecules [**?**]. The first computational study of peptide-induced pores suggests that pores can be formed in a few nanoseconds [**?**, **?**]. Recent molecular dynamics simulation studies also reported a time scale between 10 to 100 nanoseconds for pore formation in the presence of enough peptides [**?**, **?**, **?**].

Pore formation is usually accompanied by ion transport across the membrane, especially when an ionic imbalance is the forcing factor to open a pore. Cations like sodium permeate the bilayer primarily through water pore defects, while for anions like chloride ions, the pore-mediated permeation is extremely unlikely. A thin water chain is enough for the cations to diffuse across the membrane with a mechanism similar to proton diffusion along a water chain. This is not possible for negative ions. Obviously large pores (> 1.5 nm) can readily support the flux of anions [**?**, **?**]. The rate of ion permeation through intact bilayers can be estimated by calculating the free energy barrier of this process. Membrane permeability rates of sodium ions are calculated to take in the order of a day, which is in good agreement with experimental estimations [**?**]. Therefore, membrane nano-pores dramatically increase the membrane permeability for ions.

The formation of water defects across a lipid bilayer (water pores or holes) -irrespective of the mechanism that underlies the formation of these pores- unavoidably leads to diffusive translocation of lipids through the defects [**?**, **?**]. To understand the energetics of lipid translocation, it is therefore important to estimate the free energy changes associated with the pore formation process. Atomistic molecular dynamics simulations of a lipid bilayer were previously carried out to determine the free energy of a cylindrical transmembrane water pore as a function of its radius [**?**]. According to this study, at

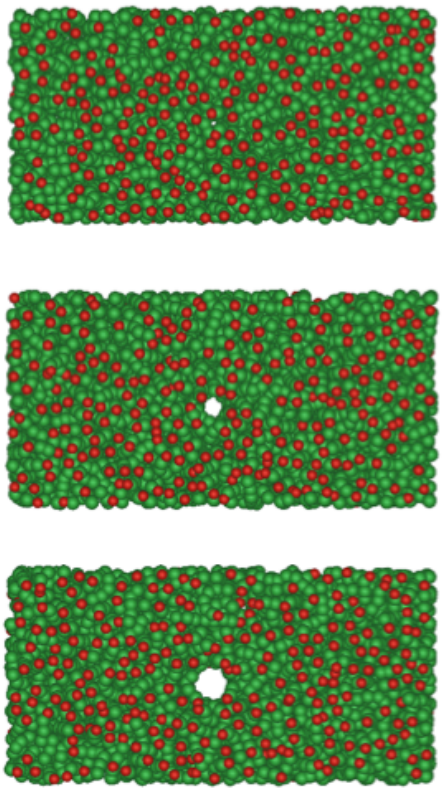

Figure 10.4: Snapshots of the pore formation across a fluid-phase bilayer.

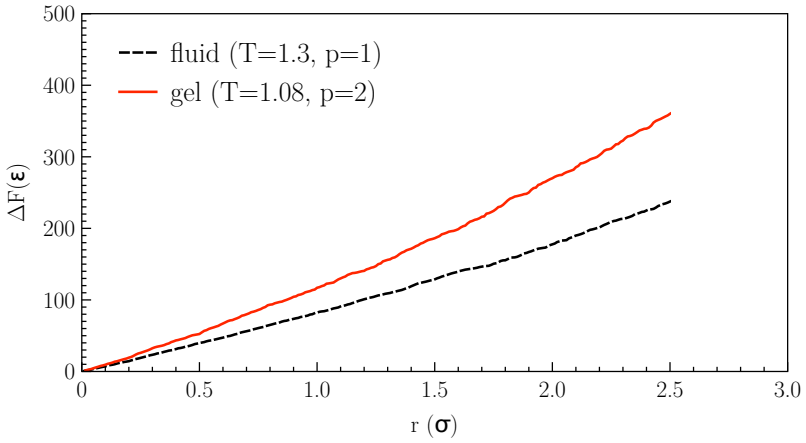

Figure 10.5: Free energy differences calculated from the distribution of the work in the pore formation processes for the gel and fluid phases ($N_{\text{path}} = 50$).

Lipid	Free energy barrier (kJ/Mol)	Model/force field	reference
CG lipid (fluid)	86 (r=0.5 σ)	CG	Present model
CG lipid (gel)	108 (r=0.5 σ)	CG	Present model
DPPC (325K)	80 (r $\sim$ 0.3 nm)	CG	[**?**]
DPPC (323K)	75-100 (r $\sim$ 0.3 nm)	CG	[**?**]

Table 10.2: Comparison of the free energy barrier for pore formation estimated by different experimental and computational methods

radius smaller than 0.3 nm, a quadratic dependence on radius was found for the free energy, while for large values of the radius, the free energy changes linearly. Recently, an investigation over the full minimum energy path to pore formation by combining the string method with dynamic self-consistent field (DSCF) theory has been carried out [**?**]. The estimated free energy barrier was lower than previous estimates by classical nucleation theory.

Considering the transient nature of the defects, nonequilibrium integration methods were applied to calculate the free energy barrier of the formation of a cylindrical pore across bilayers in the fluid and gel phases (Figure 10.5).

The creation and extension of pores inside lipid membranes happens at much larger time scales compared to the time scale of the atomic movements. However, as it occurs in a nonstationary condition, it seems reasonable to create a pore under arbitrary speed for use in a MC simulation. To produce an appropriate ensemble, 50 different initial configurations of the thermalized membranes for both gel and fluid phases were generated. To extend the pore size to a certain value, its apparent radius was increased at periodic intervals during the MC execution. The extension speeds varied among the 50 runs. From the forces acting on the lipid particles forming the boundary of the pores, the associated work was estimated. Due to the cancellation of the z-components of the forces, only radial components of the forces (pointing towards the hole axis) were considered in this estimation.

The estimated free energies for cylindrical pore geometry are presented in Figure 10.5 for the fluid and gel phases. Figure 10.5 compares the results for the two phases. For forming pores with radius $\rho < 1.5$ nm, a quadratic model fits best to the calculated free energy presented here for both phases.

As the next step, the average number of pores per unit of the bilayer area is calculated. Having the required free energy barrier ΔF for forming a pore with small radius of about 0.5σ, the density of pores is estimated by:

$$\rho = \frac{1}{A_{\text{lipid}}} \exp(-\Delta \text{F}/\text{T}) \tag{10.2}$$

where A_{lipid} is the area per lipid and T is the temperature. Through this estimation, the density of pores which can be formed in a bilayer in the fluid phase was obtained

to be about $\rho = 9$ cm^{-2}. This result is somewhat smaller than the previous reported values by previous studies for pores at the same radius [**?**, **?**]. For the gel phase with a higher value of the energy barrier of about 108 kJ/mol, the density of the pore was found to be negligible.

A similar approach can be taken to calculate the free energy of the formation of a more general elliptic toroidal pore geometry and various other distorted shapes of membrane pores emerging in nature [**?**].

10.5 Conclusions

In summary, by applying Jarzynski's equality to the work associated with the nonequilibrium translocation of lipids across the coarse grained model of lipid bilayer membranes, one is able to estimate the energy barriers of pore-independent and pore associated flip flop movements of lipids within the membrane. The approach presented here should be broadly applicable to the transport of other molecules including proteins and drugs across membranes. Future refinements of this method, including improved representation of the molecules will allow for greater insight on the energetics of nonequilibrium transport processes across cell boundaries. The significant difference between the present coarse grained model and experimental works and all atomic simulation models is due to pore formation in those approaches. In the present model, the over simplicity of the potentials and interactions of the system and more specifically the lack of polar interactions of the solvent molecules with the head part of lipids, can be considered as the reason for that the flip flop process is not followed or accompanied with pore formation. The next step for this research might be retrieving the Arrhenius pre-exponential factor to predict the flip flop rate, which is possible by performing the same simulations for different temperatures in the identical phase and also is required extra MD simulations.

A Relaxed structure of pure DPPC

In Chapter 4, by using the first principle method, DPPC molecule was relaxed to their ground states. In the following, the coordinates of the obtained relaxed structure for pure DPPC will be presented.

id	atomic symbole	x ($\AA$)	y ($\AA$)	z ($\AA$)
1	C	6.608595	33.13726	4.69945
2	C	7.658136	32.765158	2.530744
3	C	8.959785	32.669147	4.534465
4	N	7.637103	32.366086	3.961775
5	C	7.42309	30.882543	4.115239
6	C	6.022353	30.37068	3.957967
7	O	5.54742	30.50786	2.651306
8	P	4.416868	31.77095	2.379686
9	O	3.994859	32.213564	3.769868
10	O	5.073713	32.645693	1.355318
11	O	3.192247	30.973627	1.66173
12	C	2.298936	30.29324	2.502816
13	C	2.905686	28.984636	2.9685
14	C	3.659084	28.485138	1.878694
15	O	4.880553	28.044329	2.181976
16	C	5.247204	27.766275	3.312158
17	O	5.743749	27.93765	0.971263
18	C	6.882794	26.973941	1.206451
19	C	6.365774	25.604094	1.586694
20	C	7.40911	24.519332	1.705961
21	C	6.785263	23.210149	2.132909
22	C	7.730104	22.032835	2.192738
23	C	7.017032	20.74471	2.535753
24	C	7.905106	19.522101	2.542723
25	C	7.141719	18.241671	2.793533
26	C	7.9992	16.997905	2.747505
27	C	7.210435	15.722008	2.933416
28	C	8.049527	14.46812	2.839993
29	C	7.24488	13.197358	2.987676
30	C	8.069016	11.935009	2.868985
31	C	7.238319	10.681385	3.007103
32	C	1.89635	27.944876	3.354307
33	O	2.618776	26.827844	3.83119
34	O	1.597031	25.559739	2.269182
35	C	4.086008	6.902093	3.700739
36	H	5.837826	25.719199	2.565823
37	H	7.533153	26.918078	0.303486
38	H	6.292646	23.344888	3.12838
39	H	7.93854	24.384388	0.731189
40	H	6.510275	20.849047	3.527406

id	atomic symbole	x ($\AA$)	y ($\AA$)	z ($\AA$)
41	H	8.24757	21.92022	1.208623
42	H	6.617178	18.302492	3.779459
43	H	8.439479	19.4475	1.56388
44	H	6.680593	15.747523	3.918051
45	H	8.540402	16.958562	1.770341
46	H	6.711142	13.203328	3.970676
47	H	8.587674	14.454873	1.860451
48	H	6.721226	10.645809	3.99252
49	H	8.600288	11.934483	1.887386
50	H	7.509913	27.364779	2.043597
51	H	5.590661	25.285682	0.845141
52	H	8.196344	24.824529	2.436954
53	H	5.950398	22.965305	1.42803
54	H	8.541326	22.230142	2.934581
55	H	6.185961	20.585725	1.802838
56	H	8.70881	19.640697	3.309395
57	H	6.322277	18.150456	2.036726
58	H	8.799459	17.062253	3.524465
59	H	6.394662	15.678531	2.168761
60	H	8.852837	14.4956	3.616213
61	H	6.43132	13.181969	2.21962
62	H	8.874478	11.946435	3.641382
63	H	6.444698	10.636891	2.227092
64	H	7.846009	9.75622	2.9162
65	C	2.415671	25.685987	3.151127
66	C	3.327856	24.597985	3.613103
67	C	2.621306	23.26256	3.544978
68	C	3.544803	22.067075	3.572873
69	C	2.796984	20.753112	3.5999
70	C	3.689671	19.533036	3.570113
71	C	2.919341	18.234925	3.658086
72	C	3.787016	16.99872	3.593152
73	C	3.000872	15.712727	3.711027
74	C	3.852961	14.467538	3.623661
75	C	3.062722	13.185555	3.757036
76	C	3.914631	11.940948	3.658985
77	C	3.131619	10.654936	3.790421
78	C	3.988563	9.414167	3.685653
79	C	3.208436	8.125404	3.813853
80	H	1.885832	23.191296	4.381567

id	atomic symbole	x ($\mathring{A}$)	y ($\mathring{A}$)	z ($\mathring{A}$)
81	H	4.197829	24.609162	2.907283
82	H	2.150627	20.716213	4.510949
83	H	4.220079	22.098878	2.681773
84	H	2.32462	18.221294	4.604399
85	H	4.306129	19.541587	2.636881
86	H	2.436463	15.710129	4.67565
87	H	4.366537	16.99792	2.636436
88	H	2.513191	13.186675	4.730177
89	H	4.410058	14.463656	2.653728
90	H	2.585471	10.64867	4.765398
91	H	4.465851	11.943659	2.685955
92	H	2.6665	8.11854	4.789312
93	H	3.734255	24.860801	4.614715
94	H	2.008176	23.277874	2.609945
95	H	4.222897	22.125929	4.460436
96	H	2.087949	20.713922	2.737313
97	H	4.428088	19.587102	4.408883
98	H	2.16195	18.198009	2.837023
99	H	4.560281	17.039793	4.400578
100	H	2.217935	15.683094	2.914107
101	H	4.646102	14.500922	4.411924
102	H	2.26812	13.155079	2.971711
103	H	4.712925	11.973362	4.441799
104	H	2.334499	10.623224	3.007758
105	H	4.787653	9.443252	4.467581
106	H	2.412808	8.098489	3.03178
107	H	4.53867	9.419074	2.712031
108	H	4.868239	6.893849	4.491339
109	H	4.613141	6.875222	2.721713
110	H	3.508006	5.958777	3.794039
111	H	5.104744	27.662451	0.101642
112	H	6.087346	28.989098	0.806386
113	H	1.221142	28.309499	4.161524
114	H	1.295759	27.60784	2.471067
115	H	3.611141	29.131463	3.822747
116	H	6.050023	29.271025	4.194073
117	H	5.310805	30.870229	4.667651
118	H	8.093885	30.404831	3.364261
119	H	7.785348	30.619778	5.135364
120	H	7.957417	33.83459	2.493389
121	H	8.429846	32.151967	2.019502
122	H	6.638475	32.647813	2.025587
123	H	9.172436	33.749035	4.395338
124	H	8.961237	32.42423	5.616944
125	H	5.563422	32.913496	4.31142
126	H	6.848961	34.21453	4.581821
127	H	2.053366	30.925861	3.393909
128	H	1.382626	30.106506	1.896112
129	H	9.733143	32.068786	4.011304
130	H	6.673374	32.863827	5.774428

B Calculation of forces

In Chapter 10 by calculating the total force acting on a lipid to displace that from one leaflet to the other, the work done on the system during the flip flop process was estimated. In order to estimate the free energy barrier for opening a water pore inside the bilayer body, one also need to calculate forces affecting the lipids and consequently the work has been performed on the system. In this appendix, the formulation of forces acting between particles will be derived in details.

Throughout this appendix, Greek subscript, α represents Cartesian coordinates and italic Latin subscripts i, j, k, l represent atomic indices.

Generally, the coarse grained model used in this work contains three types of interactions. Two of these potentials, i.e. Lennard-Jones and FENE interactions are pair interactions that depend only on the distances between particles. In this case, one can easily derive the force function by calculating the gradient of potential, $\mathbf{F}(\mathrm{r}^{ij}) = -\nabla_{\mathrm{r}^{ij}} \mathrm{U}(\mathrm{r}^{ij})$. The third potential is a bond-angle potential which is a three body interaction. The angle dependent potential, however can be interpreted as a function of distances between particles. Therefor, the force contribution of this potential is also straightforward. In the following, corresponding force components will be presented.

B.1 Two body forces

If the distance vector between particles i and j is presented as $\mathbf{r}^{ij} = \mathbf{r}^{j} - \mathbf{r}^{i}$, the resulting forces are given as following.
For Lennard-Jones interaction, the force formula is given by:

$$\mathbf{F}_{\mathrm{LJ}}(\mathrm{r}^{ij}) = -12 \left[(\frac{\sigma_{\mathrm{LJ}}}{\mathrm{r}^{ij}})^{12} - (\frac{\sigma_{\mathrm{LJ}}}{\mathrm{r}^{ij}})^{6} \right] \frac{\mathbf{r}^{ij}}{\mathrm{r}^{ij\,2}} \; \Theta(\mathrm{r}^{ij} - \mathrm{r}_{\mathrm{cutoff}}) \tag{B.1}$$

where Θ is step function. Interaction parameters were explained in Chapter 8.
The force due to the finitely extensible nonlinear elastic interaction, $\mathrm{U}_{\mathrm{FENE}}$, is given by:

$$\mathbf{F}_{\mathrm{FENE}}(\mathrm{r}^{ij}) = -\kappa_{\mathrm{FENE}} \frac{\mathrm{r}^{ij} - \mathrm{r}_0}{1 - \left(\frac{\mathrm{r}^{ij} - \mathrm{r}_0}{\Delta \mathrm{R}_{\mathrm{max}}} \right)^2} \frac{\mathbf{r}^{ij}}{\mathrm{r}^{ij}} \tag{B.2}$$

B.2 Three body forces

If θ_{ijk} be the angle between three adjacent beads, the bond angle potential has the form:

$$\mathrm{U}(\theta_{ijk}) = \kappa_{\mathrm{BA}}(1 + \cos(\theta_{ijk})) \tag{B.3}$$

It can be proved that, the three body force can be expressed as the sum of the pair by pair interactions:

$$\mathrm{F}^{\mathrm{i}}_{\alpha}(\mathrm{BA}) = \sum_{l \neq i} \mathrm{f}^{li}_{\alpha} \tag{B.4}$$

f^{li}_{α} is the α^{th} component of the the force contribution of l^{th} particle acting on particle i^{th}. The force component f^{li}_{α} can be readily calculated as:

$$\mathrm{f}^{li}_{\alpha} = -\frac{\partial \mathrm{U}(\theta_{ijk})}{\partial \mathrm{r}^{l}_{\alpha}} \tag{B.5}$$

To this end, the potential should be rewritten in term of the particle bond vectors by replacing for $\cos(\theta_{ijk})$:

$$\cos(\theta_{ijk}) = \frac{\mathbf{r}^{ij} \cdot \mathbf{r}^{ik}}{|\mathbf{r}^{ij}|\ |\mathbf{r}^{ik}|} \tag{B.6}$$

Then, f^{li}_{α} is obtained as:

$$\mathrm{f}^{li}_{\alpha} = \frac{1}{\sin(\theta_{ijk})} \frac{\partial \mathrm{U}}{\partial \theta_{ijk}} \frac{\partial \cos(\theta_{ijk})}{\partial \mathrm{r}^{l}_{\alpha}} \tag{B.7}$$

$$\begin{aligned} \frac{\partial \cos(\theta_{ijk})}{\partial \mathrm{r}^{l}} &= \frac{\partial}{\partial \mathrm{r}^{l}} \left(\frac{\mathbf{r}^{ij} \cdot \mathbf{r}^{ik}}{|\mathbf{r}^{ij}|\ |\mathbf{r}^{ik}|} \right) \\ & (\delta_{lj} - \delta_{li}) \frac{\mathbf{r}^{ik}}{\mathrm{r}^{ij}\ \mathrm{r}^{ik}} + (\delta_{lk} - \delta_{li}) \frac{\mathbf{r}^{ij}}{\mathrm{r}^{ij}\ \mathrm{r}^{ik}} \\ & -\cos(\theta_{ijk})\ \left\{ (\delta_{lj} - \delta_{li}) \frac{\mathbf{r}^{ij}}{\mathrm{r}^{ij\,2}} + (\delta_{lk} - \delta_{li}) \frac{\mathbf{r}^{ik}}{\mathrm{r}^{ik\,2}} \right\} \end{aligned} \tag{B.8}$$

$$\begin{aligned} \mathrm{f}^{li}_{\alpha} &= \kappa_{\mathrm{BA}} \left[(\delta_{lj} - \delta_{li}) \frac{\mathrm{r}^{ik}_{\alpha}}{\mathrm{r}^{ij}\ \mathrm{r}^{ik}} + (\delta_{lk} - \delta_{li}) \frac{\mathrm{r}^{ij}_{\alpha}}{\mathrm{r}^{ij}\ \mathrm{r}^{ik}} \right. \\ & \left. -\cos(\theta_{ijk})\ \left\{ (\delta_{lj} - \delta_{li}) \frac{\mathrm{r}^{ij}_{\alpha}}{\mathrm{r}^{ij\,2}} + (\delta_{lk} - \delta_{li}) \frac{\mathrm{r}^{ik}_{\alpha}}{\mathrm{r}^{ik\,2}} \right\} \right. \end{aligned} \tag{B.9}$$

$$\mathrm{f}_{\alpha}^{ij} = -\kappa_{\mathrm{BA}} \left\{ \frac{\mathrm{r}_{\alpha}^{ik}}{\mathrm{r}^{ij}\ \mathrm{r}^{ik}} - (\cos\theta_{ijk})\ (\frac{\mathrm{r}_{\alpha}^{ij}}{\mathrm{r}^{ij\,2}}) \right\}$$

$$\mathrm{f}_{\alpha}^{ik} = -\kappa_{\mathrm{BA}} \left\{ \frac{\mathrm{r}_{\alpha}^{ij}}{\mathrm{r}^{ij}\ \mathrm{r}^{ik}} - \cos(\theta_{ijk})\ (\frac{\mathrm{r}_{\alpha}^{ik}}{\mathrm{r}^{ij\,2}}) \right\} \tag{B.10}$$

By using the Equation (B.4), the total force acting on the i^{th} particle from its two connected neighbors can be obtained.

Publications

Results of the present work have been published in:

- Chapter 4: "**Hydration strongly affects the molecular and electronic structure of membrane phospholipids**". *J. Chem. Phys.*, 136:114709, 2012.
- Chapter 5: "**Interfacial water facilitates energy transfer by inducing extended vibrations in membrane lipids**". *J. Phys. Chem. B*, 116:6455, 2012.
- Chapter 6: "**Vibrational lifetimes of hydrated phospholipids**". *Euro. Phys. Lett*, 102:28008, 2013.
- Chapter 7: "**Enhanced autoionization of water at phospholipid interfaces**". *J. Phys. Chem. C*, 117(1):510, 2013.
- "**Lipid Nanotechnology- A review**". *International Journal of Molecular Sciences.* 14:1,2013.

Bibliography

[1] J. M. Soler, E. Artacho, J. D. Gale, A. Garcia, J. Junquera, P. Ordejón, and D. Sánchez-Portal. *J. Phys. Condens. Matter*, 14(11):2745, 2002.

[2] N. Agmon and M. Gutman. *Nature Chem.*, 3:840, 2011.

[3] M. Heim, G. Cevc, R. Guckenberger, H. F. Knapp, and W. Wiegrabe. *Biophys. J.*, 69(2):489, 1995.

[4] A. Y. Mulkidjanian, J. Heberle, and D. A. Cherepanov. *Biochimica et Biophysica Acta (BBA) - Bioenergetics*, 1757(8):913, 2006.

[5] M. Prats, J. Teissi, and J.F. Toccane. *Nature*, 322:756, 1986.

[6] S. Serowy, S. M. Saparov, Y. N. Antonenko, W. Kozlovsky, V. Hagen, and P. Pohl. *Biophys J.*, 84:1031, 2003.

[7] A. M. Smondyrev and G. A. Voth. *Biophys. J.*, 82:1460, 2002.

[8] A. Springera, V. Hagenb, D. A. Cherepanovc, Y. N. Antonenkod, and P. Pohla. *PNAS*, 108:14461, 2011.

[9] J. Teissié, M. Prats, P. Soucaille, and J. F. Tocanne. *Proc. Natl. Acad. Sci.*, 82(10):3217, 1985.

[10] T. Yamashita and G. A. Voth. *J. Phys. Chem. B*, 114:592, 2010.

[11] O. Lenz and F. Schmid. *J. Mol. Liquids*, 117:147, 2005.

[12] R. Koynova and M.Caffrey. *Biochim.Biophys.Acta*, 1376:91, 1998.

[13] K. Yang and Y. Ma. *Soft Matter*, 8:606, 2012.

[14] O. G. Mouritsen. Springer-Verlag, Berlin, 2005.

[15] S. L. Veatch and S. L. Keller. *Phys. Rev. Lett.*, 89:268101, 2002.

[16] S. J. Singer and G. L. Nicholson. *Science*, 175(23):720, 1972.

[17] H. T. McMahon and J. L. Gallop. *Nature*, 438:590, 2005.

[18] J. Zimmerberg and L. V. Chernomordik. *Science*, 310:1626, 2005.

[19] M. M. Kozlov, H. T. McMahon, and L. V. Chernomordik. *Trends, Biochem. Sci.*, 35:699, 2010.

[20] J. Lee and B. R. Lentz. *Proc. Natl. Acad. Sci. USA*, 95:9274, 1998.

[21] K. Simons and D. Toomre. *Nat. Rev. Mol. Cell Biol.*, 1:31, 2000.

[22] P. Ordejón, E. Artacho, and J. M. Soler. *Phys. Rev. B*, 53(6):10441, 1996.

[23] D. Sánchez-Portal, , P. Ordejón, E. Artacho, and J. M. Soler. *Quant. Chem*, 65:453, 1997.

[24] C. Y. Ruan, V. A. Lobastov, F. Vigliotti, S. Y. Chen, and A. H. Zewail. *Science*, 304:80, 2004.

[25] F. Noé, I. Horenko, C. Schütte, and J. C. Smith. *J. Chem. Phys.*, 126:155102, 2007.

[26] M. Karplus and J. A. McCammon. *Nature Struct. Mol. Biol.*, 9:646, 2002.

[27] D. Düchs and F. Schmid. *J. Phys: Cond. Matt*, 13:4853, 2001.

[28] L. V. Chernomordik and M. M. Kozlov. *Nat. Struct. Mol. Biol.*, 15(7):675, 2008.

[29] R.B. Gennis. Springer-Verlag, New York, 1989.

[30] R. Koynova and M. Caffrey. *Chem. Phys. Lipids*, 69(3):181, 1994.

[31] R. Koynova and M. Caffrey. *Chem. Phys. Lipids*, 69:1, 1994.

[32] R. Koynova and M.Caffrey. *Biochim.Biophys.Acta*, 1255(3):213, 1995.

[33] J. N. Israelachvili, D. J. Mitchell, and B. W. Ninham. *J. Chem. Soc.*, 72:1525, 1976.

[34] M. Caffrey, R. L. Magin, B. Hummel, and J. Zhang. *Biophys. J.*, 58:21, 1990.

[35] G. Tresset. *PMC Biophysics*, 2:3, 2009.

[36] O. Lenz. PhD thesis, University of Bielefeld, 2007.

[37] M. J. Janiak, D.M. Small, and G. G. Shipley. *J. Biol. Chem*, 254:6068, 1979.

[38] T. Heimburg. *Current Opinion in Colloid and Interface Science*, 5:224, 2000.

[39] A. H. de Vries, S. Yefimov, A. E. Mark, and S. J. Marrink. *Proc. Natl. Acad. Sci. USA*, 102:5392, 2005.

[40] T. Heimburg. WILEY-VCH Verlag GmbH and Co. KGaA, Weinheim, betz-Druck GmbH, Darmstadt, 2007.

[41] T. J. McIntosh, S. A. Simon, J. C. Ellington Jr., and N. A. Porter. *Biochemistry*, 23:4038, 1984.

[42] S. W. Hui, J. T. Mason, and C. H. Huang. *Biochemistry*, 23:5570, 1984.

[43] M. Kranenburg and B. Smit. *FEBS Lett.*, 568:15, 2004.

[44] R. Cotterill. John Wiley and Sons Ltd., Baffins Lane, Chichester, West Sussex PO19 1UD, England, 2002.

[45] G. A. Jamieson and D. M. Robinson. volume 2. Butterworth, London, 1977.

[46] Y. W. Hsueh, K. Gilbert, C. Trandum, M. J. Zuckermann, and J. Thewalt. *Biophys. J.*, 88:1799, 2005.

[47] J. E. Rothman and J. Lenard. *Science*, 195:743, 1977.

[48] E. F. DeLong and A. A. Yayanos. *Science*, 228:1101, 1985.

[49] S. M. Kaneshiro and D. S. Clark. *J. Bacteriol.*, 177:3668, 1995.

[50] S. M. Kaneshiro and D. S. Clark. *Appl. Environ. Microbiol.*, 33:1233, 1977.

[51] F. Possmayer, S. H. Yu, J. M. Weber, and P. G. Harding. *Can. J. Biochem. Cell Biol.*, 62:1121, 1984.

[52] L. Greengard. *Science*, 265(909):20410, 1994.

[53] G. Galli and M. Parrinello. *Phys. Rev. Lett.*, 69:3547, 1992.

[54] F. Mauri, G. Galli, and R. Car. *Phys. Rev. B*, 47:9973, 1993.

[55] P. Ordejón, D. A. Drabold, M. P. Grumbach, and R. M. Martin. *Phys. Rev. B*, 48:14646, 1993.

[56] P. Ordejón, D. A. Drabold, , R. M. Martin, and M. P. Grumbach. *Phys. Rev. B*, 51:1456, 1995.

[57] J. Kim, F. Mauri, and G. Galli. *Phys. Rev. B*, 52:1640, 1995.

[58] X.-P. Li, R. W. Nunes, and D. Vanderbilt. *Phys. Rev. B*, 47:10891, 1993.

[59] R. Car and M. Parrinello. *Phys. Rev. Lett*, 55:2471, 1985.

[60] C. M. Goringe, D. R. Bowler, and E. Hernandez. *Rep. Prog. Phys.*, 60:1447, 1997.

[61] P. Ordejón. *Comput. Mater. Sci.*, 12:157, 1998.

[62] O. F. Sankey and D. J. Niklewski. *Phys. Rev. B*, 40:3979, 1989.

[63] M. C. Payne, M. P. Teter, D. C. Allan, T. A. Arias, and J. D. Joannopoulos. *Rev. Mod. Phys.*, 64:1045, 1992.

[64] S. Goedecker. *Rev. Mod. Phys.*, 71(4):1085, 1999.

[65] W. Kohn. *Phys. Rev. Lett.*, 76:3168, 1996.

[66] E. Hernandez and M. J. Gillan. *Phys. Rev. B*, 51(10):157, 1995.

[67] W. Kohn and L. J. Sham. *Phys. Rev.*, 140:A1133, 1965.

[68] N. Troullier and J. L. Martins. *Phys. Rev. B*, 43:1993, 1991.

[69] L. Kleinman and D. M. Bylander. *Phys. Rev. Lett.*, 48:1425, 1982.

[70] E. Artacho, D. Sánchez-Portal, P. Ordejón, A. García, and J. M. Soler. *Phys. Stat. sol*, 215:809, 1999.

[71] S. G. Louie, S. Froyen, and M. L. Cohen. *Phys. Rev. B*, 26:1738, 1982.

[72] J. P. Perdew and A. Zunger. *Phys. Rev. B*, 23:5048, 1981.

[73] J. P. Perdew, K. Burke, and M. Ernzerhof. *Phys. Rev. Lett.*, 77:3865, 1996.

[74] D. Porezag, Th. Frauenheim, Th. Köhler, G. Seifert, and R. Kaschner. *Phys. Rev. B*, 51(12):947, 1995.

[75] A. P. Horsfield. *Phys. Rev. B*, 56:6594, 1997.

[76] S. D. Kenny, A. P. Horsfield, and H. Fujitani. *Phys. Rev. B*, 62:4899, 2000.

[77] J. Jaunquera, Ó. Paz, D. Sánchez-Portal, and E. Artacho. *Phys. Rev. B*, 64:235111, 2001.

[78] S. Huzinaga, J. Andzelm, M. Klobukowski, E. Radzio-Andzelm, Y. Sakai, and H. Tatewaki. Elsevier Publ. Co., Amsterdam/New York, 1984.

[79] R. Poirier, R. Kari, and R. Csizmadia. Elsevier Publ. Co., Amsterdam/New York, 1985.

[80] H. Brockman. *Chem. Phys. Lipids*, 73:57, 1994.

[81] I. Vorobyov and T. W. Allena. *J. Chem. Phys.*, 132:185101, 2010.

[82] A. D. Pickar and R. Benz. *J. Membr. Biol.*, 44:353, 1978.

[83] K. Gawrisch, D. Ruston, J. Zimmerberg, R. P. Rand V. A. Parsegian, and N. Fuller. *Biophys. J.*, 61:1213, 1992.

[84] H. Mozaffary. *Chem Phys Lipids*, 59:39, 1991.

[85] J. Schamberger and R. J. Clarke. *Biophys. J.*, 82:3081, 2002.

[86] L. G. Wang, P. S. Bose, and F. J. Sigworth. *Proc. Natl. Acad. Sci. U.S.A.*, 103:18528, 2006.

[87] F. Lairion and E. A. Disalvo. *J. Phys. Chem. B*, 113:1607, 2009.

[88] T. Starke-Peterkovic and R. J. Clarke. *Eur. Biophys. J.*, 39:103, 2009.

[89] B. Moores, F. Hane, L. Eng, and Z. Leonenko. *Ultramicroscopy*, 110(6):708, 2010.

[90] N. Kucerka, S. Tristram-Nagle, and J. F. Nagle. *Biophys J.*, 90:83, 2006.

[91] H. Hauser, I. Pascher, R. H. Pearson, and S. Sundell. *Biochimica et Biophysica Acta (BBA)-Reviews on Biomembranes*, 650:21, 1981.

[92] J. F. Nagle, R. Zhang, S. Tristram-Nagle, W. Sun, H. I. Petrache, and R. M. Suter. *Biophys J.*, 70:1419, 1996.

[93] K. Bruzik, S. M. Gupte, and M.-D. Tsa. *J. Am. Chem. Soc*, 104:4682, 1982.

[94] M. Patra, M. Karttunen, M. T. Hyvonen, E. Falck, P. Lindqvist, and I. Vattulainen. *Biophys J.*, 84:3636, 2003.

[95] G. Parr and W. T. Yang. *Annu. Rev. Phys. Chem.*, 46:701, 1995.

[96] J. Izquierdo, A. Vega, L. C. Balbas, D. Sánchez-Portal, J. Junquera, E. Artacho, J. M. Soler, and P. Ordejón. *Phys. Rev. B*, 61:13639, 2000.

[97] D. M. Ceperley and B. J. Alder. *Phys. Rev. Lett.*, 45:566, 1980.

[98] R. O. Jones and O. Gunnarsson. *Rev. Mod. Phys.*, 61:689, 1989.

[99] Z. Li, , R. M. Venable, L. A. Rogers, D. Murray, and R. W. Pastor. *Biophys. J.*, 97:155, 2009.

[100] G. van Meer, D. R. Voelker, and G. W. Feigenson. *Nat. Rev. Mol. Cell Biol.*, 9:112, 2008.

[101] E. Meirovitch and J. H. Freed. *J. Phys. Chem.*, 84:3281, 1980.

[102] S. D. Guler, D. D. Ghosh, J. Pan, J. C. Mathai, M. L. Zeidel, J. F. Nagle, and S. Tristram-Nagle. *Chem. Phys. Lipids*, 160:33, 2009.

[103] J. P. Prates Ramalho, P. Gkeka, and L. Sarkisov. *Langmuir*, 27:3723, 2011.

[104] W. J. Sun, R. M. Suter, M. A. Knewtson, C. R. Worthington, S. Tristram-Nagle, R. Zhang, and J. F. Nagle. *Phys. Rev. E*, 49:4665, 1994.

[105] R. G. Larson and S. L. Duncan. *Biophys. J.*, 94:2965, 2008.

[106] M. Pasenkiewicz-Gierula, Y. Takaoka, H. Miyagawa, K. Kitamura, and A. Kusumi. *J. Phys. Chem. A*, 101:3677, 1997.

[107] T. D. Gurkov, P. A. Kralchevsky, and K. Nagayama. *Colloid Polym. Sci.*, 274:227, 1996.

[108] S. J. Vigmond, T. Dewa, and S. L. Regen. *J. Am. Chem. Soc*, 117:7838, 1995.

[109] V. V. Volkov, Y. Takaoka, and R. Righini. *J. Phys. Chem. B*, 113:4119, 2009.

[110] V. V. Volkov, D. J. Palmer, and R. Righini. *Phys. Rev. Lett*, 99:078302, 2007.

[111] V. A. Raghunathan and J. Katsaras. *Phys. Rev. Lett.*, 74:4456, 1995.

[112] F. B. van Duijneveldt, J.G. C. M. van Duijneveldt-van de Rijdt, and J. H. van Lenthe. *Chem. Rev.*, 94:1873, 1994.

[113] M. Dion, H. Rydberg E. Schroder, D. C. Langreth, and B. I. Lundqvist. *Phys. Rev. Lett.*, 92:246401, 2004.

[114] G. Roman-Perez and J. M. Soler. *Phys. Rev. Lett.*, 103:096102, 2009.

[115] J. F. Nagle and S. Tristram-Nagle. *Biochim. Biophys. Acta.*, 1469:159, 2000.

[116] S. A. Pandit, S-W. Chiu, E. Jakobsson, A. Grama, and H. L. Scott. *Biophys. J.*, 92:920, 2007.

[117] S. A. Clough, Y. Beers, G. P. Klein, and L. S. Rothman. *J. Chem.Phys.*, 59:2254, 1973.

[118] C. A. Coulson and D. Eisenberg. *Proc. R. Soc. London A*, 291:445, 1966.

[119] P. L. Silvestrelli and M. Parrinello. *Phys. Rev. Lett*, 82:3308, 1999.

[120] S. A. Kane, M. Compton, and N. Wilder. *Langmuir*, 16:8447, 2000.

[121] M. Weis, J. Beno, E. Dobrocka, and D. Hasko. *Appl. Surf. Sci.*, 254:6370, 2008.

[122] B. Rosenberg and G. L. Jendrasiak. *Chem. Phys. Lipids*, 2:47, 1968.

[123] B. Rosenberg and E. Postow. *Annals of the New York Academy of Sciences*, 158:161, 1969.

[124] B. Rosenberg and H. C. Pant. *Chem. Phys. Lipids*, 4:203, 1970.

[125] J. Milhaud. *Biochim. Biophys. Acta, Biomembr.*, 1663:19, 2004.

[126] K. Gawrisch, V. A. Parsegian, and R. P. Rand. Springer Verlag, Berlin, 1990.

[127] Z. H. Wang, A. Pakoulev, and D. D. Dlott. *Science*, 296:2201, 2002.

[128] T. Nakano, G. Kikugawa, and T. Ohara. *J. Chem. Phys.*, 133:154705, 2010.

[129] A. Ghosh, M. Smits, J. Bredenbeck, and M. Bonn. *J. Am. Chem. Soc.*, 129(31):9608, 2007.

[130] M. Smits, A. Ghosh, J. Bredenbeck, S. Yamamoto, M. Muller, and M. Bonn. *New J. Phys.*, 9:3901, 2007.

[131] M. Bonn, H. J. Bakker, A. Ghosh, S. Yamamoto, M. Sovago, and R. K. Campen. *J. Am. Chem. Soc.*, 132:14971, 2010.

[132] X. C. Huang, A. B. McCoy, J. M. Bowman, L. M. Johnson, C. Savage, F. Dong, and D. J. Nesbitt. *Science*, 311:60, 2006.

[133] J. L. Skinner, B. M. Auer, and Y. S. Lin. *Adv. Chem. Phys.*, 311(142):59, 2009.

[134] A. Szent-Gyorgyi. *Science*, 93:609, 1941.

[135] K. Esfarjani. Chapter 1, phonons and lattice dynamics. `web.mit.edu/kei1/www/CM231/phonons.pdf`, MIT University.

[136] B. T. Wong and M. P. Mengüç. Springer Verlag, Berlin, New York, 2008.

[137] L. E. Silbert, A. J. Liu, and S. R. Nagel. *Phys. Rev. E*, 79:021308, 2009.

[138] E. M. Huisman and T. C. Lubensky. *Phys. Rev. Lett*, 106:088301, 2011.

[139] J. L. Skinner and B. M. Auer. *J. Chem. Phys.*, 128:224511, 2008.

[140] M. C. Rheinstadter. SpringerLink, 2012.

[141] R. Lipowsky and E. Sackmann. Elsevier, Amsterdam, 1995.

[142] M. M. Martin and J. T. Hynes. Elsevier, Amsterdam, 2004.

[143] M. Kimble and W. Castleman. Elsevier, Amsterdam, 2006.

[144] C. Fang, A. Senes, L. Cristian, W. F. DeGrado, and R. M. Hochstrasser. *Proc. Natl. Acad. Sci. USA*, 103:16740, 2006.

[145] J. C. Deak, Y. S. Pang, T. D. Sechler, Z. H. Wang, and D. D. Dlott. *Science*, 306:473, 2004.

[146] V. V. Volkov, F. Nuti, Y. Takaoka, R. Chelli, A. M. Papini, and R. Righini. *J. Am. Chem. Soc.*, 128:9466, 2006.

[147] P. Mukherjee, I. Kass, I. Arkin, and M. T. Zanni. *Proc. Natl. Acad. Sci. USA*, 103:8571, 2006.

[148] Y. H. Wang, J. S. Baskin, T. B. Xia, and A. H. Zewail. *Proc. Natl. Acad. Sci. USA*, 101:18000, 2004.

[149] I. J. Finkelstein, H. Ishikawa, S. Kim, A. M. Massari, and M. D. Fayer. *Proc. Natl. Acad. Sci. USA*, 104:2637, 2007.

[150] R. H. Austin, A. H. Xie, L. van der Meer, B. Redlich, P. A. Lindgard, H. Frauenfelder, and D. Fu. *Phys. Rev. Lett.*, 94:128101, 2005.

[151] M. H. Lim, P. Hamm, and R. M. Hochstrasser. *Proc. Natl. Acad. Sci. USA*, 95:15315, 1998.

[152] R. J. Hawkins and T. C. B. McLeish. *Biophys. J.*, 91:2055, 2006.

[153] A. W. Smith. *Biophys. Acta.*, 1818:172, 2012.

[154] K. Esfarjani and H. T. Stokes. *Phys. Rev. B*, 77:144112, 2008.

[155] J. Shiomi and S. Maruyama. *Phys. Rev. B*, 73:205420, 2006.

[156] A. S. Henry and G. Chen. *J. Comput. Theor. Nanosci.*, 5:141, 2008.

[157] A. Debernardi. *Phys. Rev. B*, 57:12847, 1998.

[158] A. J. H. McGaughey and M. Kaviany. *Phys. Rev. B*, 69:094303, 2004.

[159] J. A. Thomas, J. E. Turney, R. M. Iutzi, C. H. Amon, and A. J. H. McGaughey. *Phys. Rev. B*, 81:081411, 2010.

[160] N. de Koker. *Phys. Rev. Lett.*, 103:125902, 2009.

[161] B. Qiu, H. Bao, G. Zhang, Y. Wu, and X. Ruan. *Comput. Mater. Sci.*, 53:278, 2012.

[162] S. Nosé. *J. Chem. Phys.*, 81(1):511, 1984.

[163] W. G. Hoover. *Phys. Rev. A*, 31:1695, 1985.

[164] R. Vácha, V. Buch, A. Milet, J. P. Devlin, and P. Jungwirth. *Phys Chem Chem Phys.*, 9(34):4736, 2007.

[165] P. L. Geissler, C. Dellago, D. Chandler, J. Hutter, and M. Parrinello. *Science*, 291(5511):2121, 2001.

[166] K. Laasonen, F. Csajka, and M. Parrinello. *Chem. Phys. Lett*, 194:172, 1992.

[167] K. Laasonen, M. Parrinello, R. Car, C. Lee, and D. Van derbilt. *Chem. Phys. Lett*, 207:208, 1993.

[168] L. Rao, H. Ke, G. Fu, X. Xu, and Y. Yan. *J. Chem. Theory. Comput.*, 5:86, 2009.

[169] E. M. Stuve. *Chem. Phys. Lett.*, 519, 2012.

[170] X. Xu and W. A. Goddard. *J. Phys. Chem. A*, 108:2305, 2004.

[171] U. Bergmann, A. D. Cicco, P. Werner, E. Principi, P. Glatzel, and A. Nilsson. *J. Chem. Phys.*, 127:174504, 2007.

[172] K. A. Sharp and J. M. Vanderkooi. *Acc Chem. Res.*, 43:231, 2010.

[173] A. K. Soper. *J. Phys. Cond. Matt.*, 19:33520, 2007.

[174] A. Hassanali, M. K. Prakash, H. Eshet, and M. Parrinello. *PNAS*, 108(51):20410, 2011.

[175] J. G. Kirkwood. *J. Chem. Phys.*, 3:300, 1935.

[176] M. P. Allen and D. J. Tildesley. Oxford Science Publications, Oxford, 1987.

[177] D. Frenkel and B. Smith. Academic Press, New York, 2002.

[178] H. R. Warner. *Industrial and Engineering Chemistry Fundamentals*, 11:379, 1972.

[179] G. S. Grest and K. Kremer. *Phys. Rev. A*, 33:3628, 1986.

[180] R. Götz and R. Lipowsky. *J. Chem. Phys.*, 108:7397, 1998.

[181] B. West. PhD thesis, University of Bielefeld, 2008.

[182] D. Schmidt and R. MacKinnon. *Proc. Natl. Acad. Sci.*, 105(49):19276, 2008.

[183] D. M. S. P. Sansom and P. C. Biggin. Royal Society of Chemistry, 1st edition edition, 2010.

[184] N. Morone, T. Fujiwara, K. Murase, H. Ike R. S. Kasai, S. Yuasa, J. Usukura, and A. Kusumi. *J. Cell Biol.*, 174(6):851, 2006.

[185] M. Claesson, R. Frost, S. Svedhem, and M. Andersson. *Langmuir*, 27(14):8974, 2011.

[186] K. J. Tierney, D. E. Block, and M. L. Longo. *Biophys. J.*, 89(4):2481, 2005.

[187] G. Popescu, T. Ikeda, K. Goda, C. A. Best-Popescu, M. Laposata, S. Manley, R. R. Dasari, K. Badizadegan, and M. S. Feld. *Phys. Rev. Lett.*, 97:218101, 2006.

[188] J. S. Mitchell, C. A. Zorman, T. Kicher, S. Roy, and M. Mehregany. *J. Aerosp. Eng.*, 16(2):46, 2003.

[189] P. Martins, C. Malhaire, S. Brida, and D. Barbier. *Microsyst Technol.*, 15(9):1343, 2009.

[190] J. Neder, B. West, P. Nielaba, and F. Schmid. *Biophys. J.*, 96:101, 2009.

[191] W. Helfrich. *Z. Naturforsch. C*, 28:693, 1973.

[192] G. Brannigan and F. L. H. Brown. *Biophys. J.*, 90:1501, 2006.

[193] B. West, F. L. H. Brown, and F. Schmid. *Biophys. J.*, 96:101, 2009.

[194] P. Liu and Y. W. Zhang. *Appl. Phys. Lett*, 94(23):231912, 2009.

[195] M. Falcioni, M. J. Bowick, E. Guitter, and G. Thorleifsson. *Europhys. Lett.*, 38(1):67, 1997.

[196] L. D. Landau, L. P. Pitaevskii, E.M. Lifshitz, and A. M. Kosevich. volume 7. Butterworth-Heinemann, third edition, 1986.

[197] H. Qian. *J. Phys. Chem. B*, 110:15063, 2006.

[198] D. J. Schnell and D. N. Hebert. *Cell*, 112:491505, 2003.

[199] F. Xabier Contreras, L. Snchez-Magraner, A. Alonso, and F. M. Goi. *FEBS Letters*, 584:1779, 2010.

[200] J. D. Perlmutter and J. N. Sachs. *,J. Am. Chem. Soc*, 133:6563, 2011.

[201] J. C. M. Holthuis and T. P. Levine. *Nature Reviews Molecular Cell Biology*, 6:209, 2005.

[202] J. Liu and J. C. Conboy. *Biophys. J.*, 89:2522, 2005.

[203] W. F. D. Bennett and D. P. Tieleman. *J. Chem. Theory Comp*, 7:2981, 2011.

[204] A. A. Gurtovenko, J. Anwar, and I. Vattulainen. *Chem. Rev.*, 110:6077, 2010.

[205] S. J. Marrink, A. H. de Vries, and D. P. Tieleman. *Bba-Biomembranes*, 1788:149, 2009.

[206] D. P. Tieleman and S. J. Marrink. *J. Am. Chem. Soc.*, 128:12462, 2006.

[207] J. Martí and F. S. Csajka. *EurPhys. Lett.*, 61:409, 2003.

[208] R. D. Kornberg and H. M. McConnell. *Biochemistry*, 10:1111, 1971.

[209] M. Nakano, M. Fukuda, T. Kudo, N. Matsuzaki, T. Azuma, K. Sekine, H. Endo, and T. Handa. *J. Phys. Chem. B*, 113:6745, 2009.

[210] N. Sapay, W. F. Drew Bennett, and D. P. Tieleman. *Soft Matter*, 5:3295, 2009.

[211] A. A. Gurtovenko, O. I. Onike, and J. Anwar. *Langmuir*, 24:9656, 2008.

[212] C. Daniels, N. Noy, and D. Zakim. *Biochemistry*, 24:3286, 1985.

[213] J. Storch and A. M. Kleinfeld. *Biochemistry*, 25:1717, 1986.

[214] C. Jarzynski. *Phys. Rev. Lett.*, 78:2690, 1997.

[215] C. Jarzynski. *Phys. Rev. E*, 56:5018, 1997.

[216] S. Park, F. Khalili-Araghi, E. Tajkhorshid, and K. Schulten. *J. Chem. Phys.*, 119:3559, 2003.

[217] T. C. Anglin, M. P. Cooper, H. Li, K. Chandler, and J. C. Conboy. *J. Phys. Chem. B*, 114:1903, 2010.

[218] S. Jo, H. Rui, J. B. Lim, J. B. Klauda, and W. Im. *J. Phys. Chem. B,*, 114:13342, 2010.

[219] A. A. Gurtovenko and I. Vattulainen. *J. Phys. Chem. B*, 111:13554, 2007.

[220] H. Leontiadou, A. E. Mark, and S. J. Marrink. *J. Am. Chem. Soc.*, 128:12156, 2006.

[221] A. H. de Vries, A. E. Mark, and S. J. Marrink. *J. Am. Chem. Soc.*, 126:4488, 2004.

[222] B. Smit, P. A. J. Hilbers, K. Esselink, L. A. M. Rupert, N. M. van Os, and A. G. Schlijper. *J. Phys. Chem.*, 95:6361, 1991.

[223] Z. Wu, Q. Cui, and A. Yethiraj. *J. Phys. Chem. B*, 114:10524, 2010.

[224] S. O. Yesylevskyy, L. V. Schafer, D. Sengupta, and S. J. Marrink. *PLoS Comput. Biol.*, 6:e1000810, 2010.

[225] E. Evans and K. Ritchie. *Biophys. J.*, 72:1541, 1997.

[226] S. Lev. *Nature Reviews Molecular Cell Biology*, 11:739, 2010.

[227] F. J. Martin and R. C. MacDonald. *Biochemistry*, 15:321, 1976.

[228] G. Duckwitzpeterlein, G. Eilenberger, and P. Overath. *Biochim. Biophys. Acta.*, 469:311, 1977.

[229] M. A. Roseman and T. E. Thompson. *Biochemistry*, 19:439, 1980.

[230] L. R. Mclean and M. C. Phillips. *Biochemistry*, 23:4624, 1984.

[231] E. A. Dawidowicz. *Curr. Top. Membr. Transp.*, 29:175, 1987.

[232] T. M. Bayerl, C. F. Schmidt, and E. Sackmann. *Biochemistry*, 27:6078, 1988.

[233] J. W. Nichols and R. E. Pagano. *Biochemistry*, 20:2783, 1981.

[234] J. W. Nichols. *Biochemistry*, 24:6390, 1985.

[235] D. R. Voelker. *J. Lipid Res.*, 44:441, 2003.

[236] A. A. Gurtovenko and J. Anwar. *J. Phys. Chem. B*, 111:13379, 2007.

[237] S. J. Marrink, E. Lindahl, O. Edholm, and A. E. Mark. *J. Am. Chem. Soc.*, 123:8638, 2001.

[238] D. P. Tieleman. *BioPhys. J.*, 86:371a, 2004.

[239] R. A. Bockmann, B. L. de Groot, S. Kakorin, E. Neumann, and H. Grubmuller. *BioPhys. J.*, 95:1837, 2008.

[240] D. P. Tieleman, H. Leontiadou, A. E. Mark, and S. J. Marrink. *J. Am. Chem. Soc.*, 125:6382, 2003.

[241] M. Tarek. *BioPhys. J.*, 88:4045, 2005.

[242] P. T. Vernier and M. J. Ziegler. *J. Phys. Chem. B*, 111:12993, 2007.

[243] P. T. Vernier, M. J. Ziegler, Y. H. Sun, W. V. Chang, M. A. Gundersen, and D. P. Tieleman. *J. Am. Chem. Soc.*, 128:6288, 2006.

[244] Q. Hu, R. P. Joshi, and K. H. Schoenbach. *Phys. Rev. E*, 72:031902, 2005.

[245] M. J. Ziegler and P. T. Vernier. *J. Phys. Chem. B*, 112:13588, 2008.

[246] P. T. Vernier, M. J. Ziegler, Y. H. Sun, M. A. Gundersen, and D. P. Tieleman. *Phys. Biol.*, 3:233, 2006.

[247] A. A. Gurtovenko and I. Vattulainen. *J. Am. Chem. Soc.*, 127:17570, 2005.

[248] A. A. Gurtovenko and I. Vattulainen. *Biophys. J.*, 92:1878, 2007.

[249] S. K. Kandasamy and R. G. Larson. *J. Chem. Phys.*, 125:074901, 2006.

[250] S. J. Marrink, A. H. de Vries, and A. E. Mark. *J. Phys. Chem. B*, 108:750, 2004.

[251] T. V. Tolpekina, W. K. den Otter, and W. J. Briels. *J. Chem. Phys.*, 121:12060, 2004.

[252] T. V. Tolpekina, W. K. den Otter, and W. J. Briels. *J. Chem. Phys.*, 121:8014, 2004.

[253] M. Pasenkiewicz-Gierula, K. Murzyn, T. Rog, and C. Czaplewski. *Acta Biochim. Pol.*, 47:601, 2000.

[254] K. Murzyn, T. Rog, and M. Pasenkiewicz-Gierula. *Comput. Sci.*, 3037:325, 2004.

[255] H. Leontiadou, A. E. Mark, and S. J. Marrink. *BioPhys. J.*, 92:4209, 2007.

[256] J. Wohlert, W. K. den Otter, O. Edholm, and W. J. Briels. *J. Chem. Phys.*, 124:154905, 2006.

[257] C. L. Ting, D. Appelö, and Z.-G. Wang. *Phys. Rev. Lett.*, 106:168101, 2011.

[258] S. Wi and C. Kim. *J. Phys. Chem. B*, 112(36):11402, 2008.

Acknowledgment

This work would not have been completed without the contributions from many people. Therefore, I am deeply indebted to them all and I would like to take this opportunity to acknowledge them.

First of all, I would like to express my profound gratitude and deep regards to my supervisor Prof. Philipp Maaß, who gave me the chance and the opportunity to work on such an interesting project. I am so grateful for the time he devoted to this work and the patience he always had to hear and answer my questions. He taught me the art of doing research and tried to shape me into a scientist, therefore, I am deeply indebted to him.

In particular, I would like to express a deep sense of gratitude to Prof. Mohammad Reza Rahimitabar for his exemplary guidance, monitoring and constant encouragement throughout the course of this thesis. The blessing, help and guidance given by him time to time shall carry me a long way in the journey of life on which I am about to embark.

I would like to express my sincere gratitudes to Prof. Steinhoff and Prof. Mulkidjanian for examining this dissertation.

I would like to express my special thanks to Prof. Nafari for his valuable guidance and discussions, which helped us in advancing this work through various stages.

My best thanks go to Dr. Alireza Mashaghi, whose exemplary motivation and insistence were always inspiring me. The biological part of our research was mainly conducted by him.

My warm thanks go to Dr. Pouya Partovi for his invaluable company. He taught me how to work with the SIESTA package, and patiently answered my questions.

I would like to thank Hamid Seyyed Allaii, who taught me to be brave in Object Oriented C++ programming.

My very special and warm thanks pass towards my dearest and best friend I have ever made. Laura Saez not only was very compassionate friend of mine, but also patiently edited my poor english in the dissertation. I am profoundly indebted to her for her extraordinary company.

Last but not least, I would like to express my gratitude to all my very best colleagues in the research group of Prof. Maaß, who were beside me when I needed them. To this end, I would like to specially thank Sandra Nostheide, Susanne Hahne, Hendrik Pils, Omar Bakhti, and my former colleague Dr. Michael Schuch. Moreover, I would never forget the kindness of Mrs. Riemann, Mrs. Meyer, Mrs. Osmanovic and other department secretaries, because of their very best helps.